Development of a high sensitive receiver system for transient electromagnetics

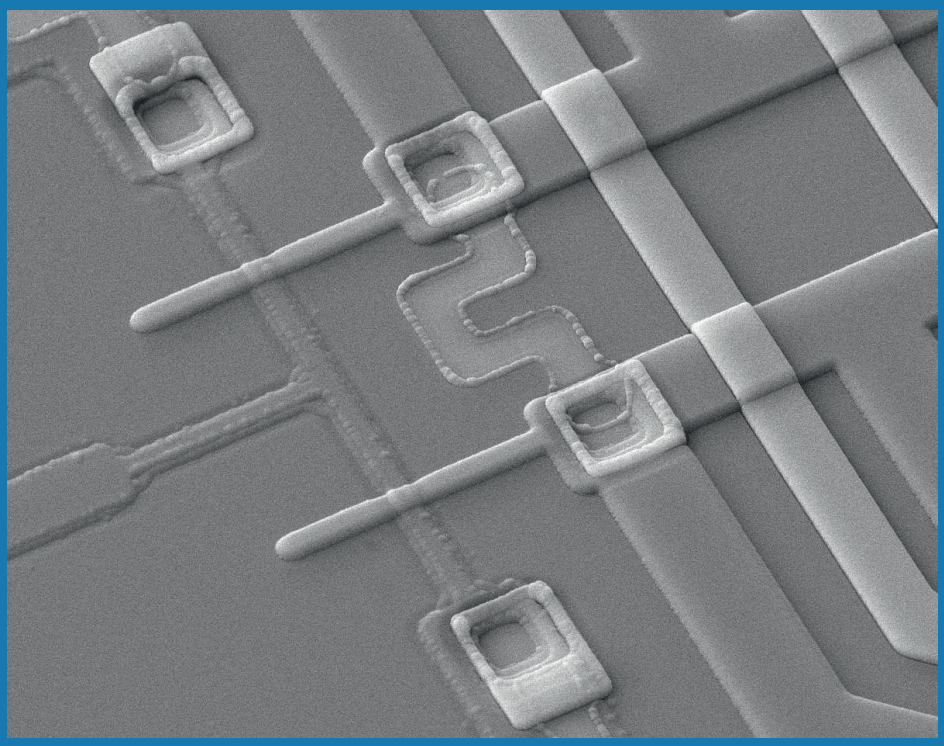

Matthias Schmelz

Ph.D. committee

Chairmen and Secretary

Prof. Dr. G. van der Steenhoven	University of Twente

Supervisor

Prof. Dr. H. Rogalla	University of Twente

Assistant supervisor

Prof. Dr. H.-G. Meyer	IPHT Jena, Germany

Members

Prof. Dr. H. Hilgenkamp	University of Twente
Prof. Dr. B. Poelsema	University of Twente
Prof. Dr. J. Flokstra	University of Twente
Prof. Dr. M. Siegel	Karlsruhe Institute of Technology, Germany
Prof. Dr. P. Febvre	University of Savoie, France

Front Cover: Photograph of a dc SQUID based on cross-type Josephson tunnel junctions used for the evaluation of the fabrication technology.

The research described in this thesis was performed at the Institute of Photonic Technology in Jena, Germany in collaboration with the Low Temperature Division at the University of Twente, Netherlands.

M. Schmelz
"Development of a high sensitive receiver system for transient electromagnetics"
Ph.D. Thesis University of Twente, Enschede, The Netherlands.

ISBN: 978-94-6259-016-8

Printed by Ipskamp Drukkers B.V. Enschede, The Netherlands

DEVELOPMENT OF A HIGH SENSITIVE RECEIVER SYSTEM FOR TRANSIENT ELECTROMAGNETICS

DISSERTATION

to obtain
the degree of doctor at the University of Twente,
on the authority of the rector magnificus,
prof. dr. H. Brinksma,
on account of the decision of the graduation committee,
to be publicly defended
on Wednesday January 22nd, 2014 at 12.45

by

Matthias Schmelz

born on 14.06.1981
in Apolda

This dissertation has been approved by:

Prof. Dr. H. Rogalla (promotor)
Prof. Dr. H.-G. Meyer (assistant-promotor)

To my family,

especially my wife Linda and my son Richard

Table of Contents

1 Introduction

1.1 Fundamentals of geophysical prospection methods

The search for metals and rare elements presumably date from the very beginning of mankind. Probably Georgius Agricola could be seen as the first who described mining and metallurgy in a scientific manner in his book “De re metallica” in 1556 [1]. Since then many developments had led to a deeper insight and a comprehensive understanding of geophysical procedures and many techniques evolved for the detection of natural mineral deposits. Due to the increased need for natural commodities, like minerals, oil and gas – which is an everlasting development more than ever nowadays – different methods and research fields emerged to enhance these detection techniques.
Figure 1.1 summarizes several exploration methods classified by the target characteristic. A detailed description of these methods can e.g. be found in [2-4]. Within this thesis I will focus on electromagnetic methods, especially the transient electromagnetic method (TEM or TDEM) searching for conductivity anomalies. However, geophysical prospection almost always combines different exploration methods. For example, at an early stage typically fast and economic airborne based methods such as gravity, magnetics and electromagnetics are applied. Due to their high mapping speed they should reveal possible deposit areas. Afterwards, high-resolution ground-based methods, like seismics, geoelectrics and electromagnetics, depending on the target and ground characteristics are used to delimit and characterize possible targets. In this regard it should be considered

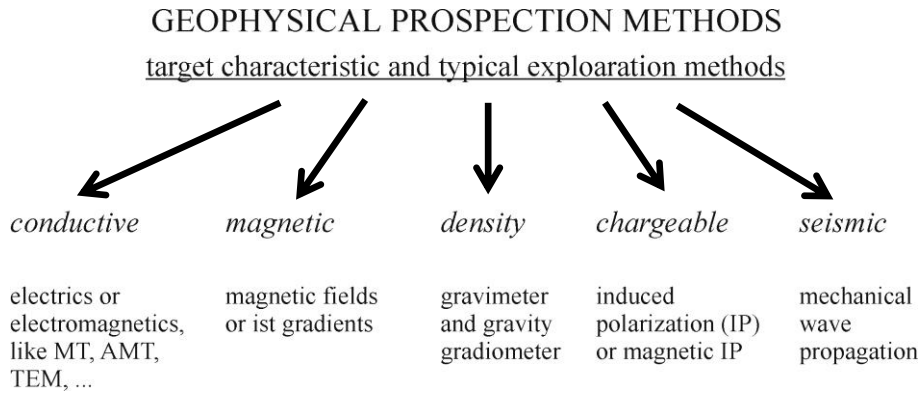

Figure 1.1: Classification of common geophysical prospection methods by the target characteristic and typical used exploration methods. MT stands for magnetotellurics, AMT for audio-magnetotellurics and TEM for transient electromagnetics.

that the choice of a suitable method is not only determined by the target itself but as well by the properties of the surrounding material of a deposit and the topography of the area. The last and most expensive step of exploration is a drilling program, where again geophysical borehole methods are applied and for instance grades of minerals are determined directly.
Nowadays it is natural to combine different exploration methods in geophysics according to the objective and the expected targets since a single prospection method sometimes gives only an indication, if the reviewed area can contain the desired target or not. In this regard not only the bare measurement, but rather an appropriate data acquisition and a fusion with data of other geophysical sensors are essential for the right interpretation and therefore the outcome of the survey.

As shown in Figure 1.1, TEM as an active electromagnetic exploration method searches (today more and more deep laying) conductive targets such as nickel, copper, gold and silver metals and iron ore bodies. I will therefore estimate the expected exploration depth as a function of soil electrical resistivity ρ. Figure 1.2 shows the dependence of the skin depth δ of an electromagnetic wave travelling into a conductive half space vs. the frequency f of investigation, wherefore the simple model $\delta\,[\mathrm{km}] \approx 0.5 \cdot (\rho/f)^{1/2}$ as described in [5] was used. Typical resistivities for sediments range from 1 to 10'000 Ωm as given in [6]. In addition, Figure 1.2 depicts the frequency range of typical prospection methods. Accordingly, the electrical resistivity of the soil and the choice of the prospection method determine the possible depth of investigation.
For the shown set of electrical resistivities, the exploration depth for TEM ranges from about few tens of meters to several kilometers. One has to notice, that this rough estimation will strongly change if the target area contains not only a single but several

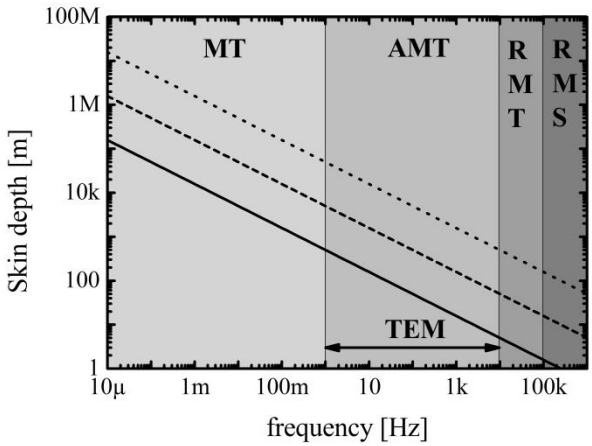

Figure 1.2: Calculated skin depth according to $\delta\,[\mathrm{km}] \approx 0.5 \cdot (\rho/f)^{1/2}$ of an electromagnetic wave penetrating into a conductive media vs. the frequency of investigation for a set of electrical resistivities (solid line = 1Ωm, dashed line = 100 Ωm and dotted line = 10000 Ωm) and corresponding prospection method [MT stands for magnetotelluric, AMT = audio-magnetotellurics, RMT = radio-magnetotellurics, RMS = radiomagnetic sounding, TEM = transient electromagnetics].

conductive layers for instance in case of a high conductive overburden.

After this short introduction into the field of geophysical prospection, within this first chapter the measurement procedure and demands on a receiver system for TEM are discussed – primarily with respect to a system which implements Superconducting Quantum Interference Devices (SQUIDs). The differences compared to commonly used systems based on induction coil type sensors will be reviewed in Chapter 1.3. Subsequently, the goals of a SQUID based system and hence the thesis goals are deduced.

1.2 Measurement procedure for TEM

The general principle for electromagnetic prospection [7] can be seen in Figure 1.3. Therein a transmitter (TX), typically a current carrying loop, produces a primary magnetic field. If the current is switched off an electromagnetic pulse is created. According to Lenz's law, this pulse gives rise to eddy currents in subsurface conductive structures, whose secondary magnetic field opposes the original change in primary magnetic flux. Due to ohmic losses, the eddy current dissipates and diffuses down- and outwards in the subsurface. A typical model for equal current density plots are expanding smoking rings [8] which cause a decaying secondary magnetic field measured on the surface. The diffusion time of the eddy currents depend on the conductivity distribution in the ground. Hence, by measuring the decay curve with a magnetic receiver system (RX) – the amplitude vs. the time after switching off the primary field – one can deduce a depth profile of electrical conductivity in the ground. In practice, repetition of this measurement procedure is used to remove offsets and for averaging of measurement data – so-called stacking – to improve signal to noise ratio. Taking measurements at various surface grid positions allow to obtain a three dimensional information of the conductivity distribution in the soil.

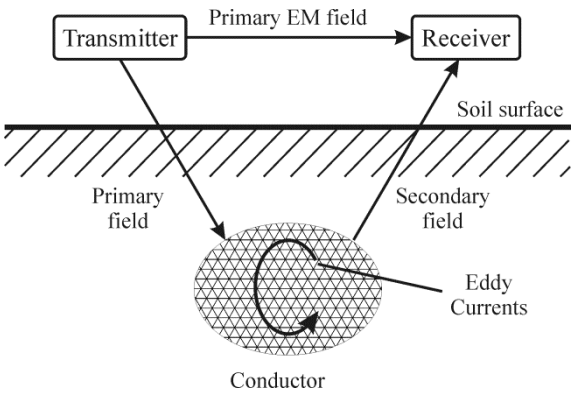

Figure 1.3: Schematic of the measurement configuration for transient electromagnetics showing the main components: transmitter, the conductor to be investigated with its eddy currents as a response to the changing primary field and the receiver system.

This short overview of the measurement procedure already emphasizes parameters, which define the performance of a measurement instrument:
By making use of artificial excitations one needs to couple the primary transmitter field to the target of interest. Here is a general trend towards large primary field amplitudes facilitated by stronger transmitters as this determines the secondary field magnitude and therefore the depth of investigation. Often the available driving power together with portability imposes practical limits for field operation.
Furthermore, the characteristic of the target sets the shape of the decaying secondary field. One can influence the signal strength by the choice of the prospection method and therefore the choice of the physical parameters to be measured, as will be discussed in the next section by comparing SQUIDs and induction coil type sensors for TEM.
The receiver sensitivity is the main parameter determining the performance of the measurement system. It sets the signal to noise ratio (SNR) thereby limiting the maximum exploration depth. On the other hand, more sensitive receiver systems allow reducing the number of averages (stacking) of measured data and hence increasing the mapping speed. Here, the sensor sensitivity will be defined by the sum of intrinsic sensor noise as well as electronics and cultural noise.
As contributions to the system performance like primary field amplitude and target characteristic are mostly set for a certain prospection method and measurement setup, it is mandatory to improve the receiver sensitivity as much as possible, always taking interactions of the sensor with other parts of the system, like the transmitter, into account. This will be the main focus of this thesis.

1.3 Advantages of SQUID systems – d*B*/d*t* vs. *B*

Most of today's measurement systems for transient electromagnetics are based on induction coil sensors. These sensors measure the time derivative of the magnetic induction, d*B*/d*t*, whereas SQUIDs or fluxgate sensors directly measure *B*.
Within the last years, the pros and cons of measuring the magnetic induction vs. its time derivative have been summed up extensively, like for instance in [9]. In [10] a comparison with respect to the measured signal strength is given. Accordingly, under the assumption of a half-space with a conductivity σ, which is roughly fulfilled for the position of the receiver at the soil surface, the late-time signal amplitude of the magnetic field response can be written as [10]

$$B_z = \frac{I\sigma^{3/2}\mu_0^{5/2}a^2}{30\sqrt{\pi}t^{3/2}}. \tag{1.1}$$

Here I is the transmitter current amplitude, a denotes the radius of a circular transmitter loop, t the time and μ_0 the vacuum permeability. The subscript z indicates the response in z direction; that is perpendicular to the soil surface.
In contrast the induced voltage response V of an induction coil accounts to [10]

$$V = \frac{I\sigma^{3/2}\mu_0^{5/2}a^2}{30\sqrt{\pi}t^{5/2}} \cdot A_{\text{eff}}, \tag{1.2}$$

where $A_{\text{eff}} = \partial\Phi/\partial B$ being the effective area of the magnetometer.
As the measured signal amplitude for a certain time-stamp after switching off the primary field can be attributed to the depth of the signal source, the difference in the time dependencies between B and dB/dt sensors implicate a larger exploration depth for B-field sensors. This implies a faster decrease of the induced voltage response compared to the magnetic field response, thus prohibiting measurements at very late times (in the sense a long time after switching off the TX signal) and therefore larger exploration depths in case of B-field sensors.
For example, in cases of high conductive overburden the voltage response of induction coils drops more rapidly than the magnetic field response which precludes detection of conductive targets below the overburden. In contrast, B-field sensors can "look through" such high conductivity layers.
In addition, the frequency dependence of SQUID-based measurement systems is flat above the $1/f$ noise corner, which is typically about a few Hz. In contrast, induction coil-type sensors are typically optimized to a minimum noise at about 1 kHz increasing to smaller frequencies.
Moreover, in [11] the influence of atmospheric events or sferics, electromagnetic waves due to thunderstorms, which travel between the Ionosphere and the Earth's surface, was reported to be about a factor of 100 larger in coil-type than in B-field sensors. In contrast B-field sensors are more affected by sensor movement noise like vibrations, which couples the Earth's magnetic field into the sensor.
In terms of sensitivity it was shown in [12], that SQUID sensors are to be favored respect to fluxgate sensors. More precisely, a comparison of low and high temperature superconductive SQUIDs (LTS and HTS) and fluxgate sensor data lead to ratios of the averaging times as 1 (LTS) : 28 (HTS) : 870 (fluxgate) to obtain the same signal to noise ratios. Accordingly, the use of LTS SQUID sensors allows a much faster mapping speed, due to lower number of averages of measured data.
Due to the above statements the focus of this thesis is drawn towards the development of a receiver system for transient electromagnetics based on SQUIDs.

1.4 Application scenarios and demands

Electromagnetic receiver systems may be used for either ground or airborne based measurements. Within this thesis the focus is set on a ground-based application, although the sensor characteristics should allow both scenarios. Especially for the discussion of the achievable system slew-rate the demands for an airborne based application will be considered. For ground-based applications the situation will be weakened, although such high slew rates would be very beneficial, as this allows the measurement with receiver positions closer to the transmitter coil wire. Ongoing work towards an airborne operation of SQUID systems will be addressed in the Appendix with respect to the dynamic range limitation of conventional SQUID systems.
Typical transmitter loop sizes for ground-based TEM vary between $(1 \times 1)\,\text{m}^2$ and $(2 \times 2)\,\text{km}^2$, where larger loops allow for deeper prospection. An overview of common

transmitter-receiver configurations can be found in [7]. For mapping it may however be logistically easier to move the small receiver rather than the large transmitter loop. In the widely used "in-loop" configuration [7] the receiver is therefore placed inside the transmitter loop, and may measure at various positions inside the loop.
Typical ground-based TEM receiver systems are e.g. ProTEM by Geonics Limited [13], GDP by Zonge International [14] or CDR2 by Crone Geophysics [15].
In order to scan large and often hardly accessible areas in short times, different airborne electromagnetic measurement systems had been developed in recent years. An historical overview of airborne geophysics with special emphasis on airborne electromagnetic measurement systems can be found in [16, 17]. As described therein these systems are either fixed-wing, like Spectrem 2000 [18], GEOTEM [19] or MEGATEM [20], or helicopter-based systems, like AeroTEM [21], VTEM [22] or HeliGEOTEM [23].
During about the last decade the main focus of development was mainly set on lower repetition frequencies and larger amplitudes of the transmitter currents. Current airborne-based systems feature magnetic dipole moments of more than one million Am^2 [16]. Both of these directions aim for larger prospection depths, as most of the easy explorable mineral deposits have already been discovered. Even so, nowadays needs to reveal very deep and/or conductive targets or targets under conductive overburden can more easily or sometimes only met with SQUID sensors, as discussed in Chapter 1.3. Furthermore, the use of SQUID sensors with their extremely low noise would probably enable a path of improved economic feasibility in view of deep located targets, as these systems may operate with reduced magnetic dipole moments and therefore probably more compact systems.

Due to their superior ability to measure the Earth's magnetic field, already in the 1970s SQUIDs have been used in geophysics [24, 25]. Probably the complexity of these systems, as well as the requirement of cryogenics hampered the widespread use of such systems in these days. Since then, several SQUID systems aimed for TEM have been reported [26-30]. According to the results presented therein, one can propose the main development tasks for next generation SQUID TEM receivers: these are a sufficiently low (white) noise level, improved stability against magnetic background fields during cool-down as well as during operation with additional applied magnetic fields and an increased system slew rate, especially in the case of airborne systems.

1.5 Goals of the thesis and outline

Very challenging requirements regarding the receiver system and hence the SQUID sensors emerge for the intended application in TEM. The system should feature an orthogonal triple of SQUID magnetometers as this allows better data inversion than just the vertical component. Additionally, this comes along with a better resolution of conductor's edges, independent on its orientation respect to the sensor orientation. The magnetic field noise of the sensors should be well below 20 $fT/Hz^{1/2}$ in the frequency range of 10 Hz to about 20 kHz, with signal contributions of up to ± 2.5 µT. Furthermore

unshielded field operation in desert-like to subarctic conditions and even by non-professional personal demands for a very reliable and robust system.
Beside the sufficient low noise in TEM as an active method, a main figure of merit is the system slew rate or the ability to track fast changing signals. For a rough estimation of required parameters, I will assume a configuration similar to the AeroQuest system [21], where the SQUID will be set up in the center of the transmitter coil, which is towed by a helicopter. The magnitude of the primary field of about 1 mT in the AeroTEM III transmitter can partially be compensated at the position of the SQUID system to below 1 µT. The sudden switch-off of the square transmitter current within about 100 µs leads to a required system slew rate of about 10 mT/s. This results in about 2 $M\Phi_0$/s for an inverse magnetometer effective area of about 5 nT/Φ_0, just to follow the switching of the primary field.
Additionally, the application requires a good resolution of the signal slope for early times after switching off the TX current, as in this period signals from shallow sources are located. Assuming an envisaged resolution of the slope of 5%, the required slew rate is about 200 mT/s or 40 $M\Phi_0$/s for the above considered case.

To sum up, the objective of this thesis is the development of a highly sensitive receiver system based on SQUIDs for transient electromagnetics. As SQUIDs will be used as sensitive magnetic field sensors later on called magnetometers, I will comment on basic relations and properties of superconductors and SQUIDs in Chapter 2. The condition of extremely low noise sensors leads to a realization concept pointing towards Josephson junctions with small geometric area and small capacitance. Chapter 3 therefore describes typical current junction fabrication technologies and comments on their advantages and limitations whereupon the approach of cross-type Josephson tunnel junctions is explained in detail. The fabricated Josephson junctions are analyzed in Chapter 4 with regard to junction quality and their capacitance. Furthermore, in Chapter 5 I will report on the design, simulation and characterization of adequate sensors suitable for the described application. Special emphasis will be given to the increased usable voltage swing of the SQUIDs, improved sensor noise and the sensor stability with respect to magnetic background fields during cool-down as well as during operation. Moreover, the low-frequency noise behavior of these sensors will be critically examined. The observed areal dependence of low-frequency magnetic flux noise will be discussed within a model of fluctuating surface spins. In Chapter 6 I will describe the composition of the SQUID system and comment on achieved parameters, especially the sensor noise and slew rate. In order to evaluate the system's low-frequency noise in an unshielded environment I will present and discuss results of correlation based processing of measured sensor signals. Finally, I will show results from a ground based field application to demonstrate the system performance.

Beyond the scope of this thesis I will shortly summarize continuative work in the Appendix. These are the expansion of the fabrication technology to deep submicron Josephson junctions with critical current densities of up to 20 kA/cm^2 [31], the further use of the cross-type junction technology in SQUID current sensors exhibiting extraordinary low current noise levels of 3 $fA/Hz^{1/2}$ [32], first steps towards nanoSQUIDs based on

Josephson tunnel junctions [33] or bi-SQUIDs as linear SQUID amplifier [34]. Furthermore, I comment on the development of a SQUID based setup for the absolute measurement of the Earth's magnetic field [35] and a concept for an on-chip linearization of the SQUID output voltage [36] for next generation SQUID sensors aimed for geophysical measurement setups.

2 Fundamentals

As illustrated in the previous chapter, the use of SQUIDs gains potential for substantial improvements in exploration depth and speed for transient electromagnetics. For a basic understanding of SQUIDs and their working principle, I will give a short summary on effects and relations, related to superconductivity, Josephson junctions and dc SQUIDs, as well as on SQUID electronics within this chapter.
However, for a complete overview the reader is referred to special textbooks, as e.g. [37-41], on the according subjects.

2.1 Fundamentals of Superconductivity

The observation of vanishing dc resistance of mercury by the Dutch physicist Heike Kammerling Onnes in 1911 [42, 43] can probably be seen as the birth of superconductivity. Today, nearly 100 years later, scientists and engineers have gained a deep insight into its principles and one could probably say that superconducting fabrication technology and superconducting applications have become mature and achieved success in some niche applications.
Besides the already mentioned effect of vanishing dc resistance below a critical temperature T_C the superconducting state in addition only persists below a maximum critical field H_C and critical current density J_C. As these parameters are material dependent, different classes of superconducting materials emerged. Due to the high reliability and the potential for use in an industrial-like fabrication process, some materials like e.g. Al and Nb have achieved major significance. Within this thesis I will therefore focus on these metallic LTS superconductors, although there have been improvements like e.g. in HTS film quality, which probably open up the way for numerous applications in the future. The desired resolution of the envisaged sensors within this thesis, as well as their intended purpose for unshielded operation enforces the use of low temperature superconductors.

In a superconductor the current is carried by pairs of electrons, so called Cooper-pairs, which have zero spin and therefore behave as Bosons. At low temperatures they all condense in the same quantum state and could be described by a collective superconducting wave function $\Psi = \Psi_0 \cdot \exp(i\phi)$, with $\phi(x,t)$ being the time and space-dependent phase and $n_S = |\Psi|^2$ the Cooper-pair density. The length scale at which n_S decays is described by the coherence length

$$\xi = \sqrt{\frac{m_S}{4\pi\mu_0 e^2 \Psi_0^2}}, \tag{2.1}$$

typically in the range of a few tens to hundred nm for LTS materials [41]. Here m_S is the mass of the superconducting charge carriers and μ_0 being the vacuum permeability.
In addition, if a superconductor of sufficient thickness will be placed into a magnetic field, a screening current in a finite outer layer is flowing, which expels the field from the inside of the superconductor. The thickness of this outer layer is described by the London penetration depth

$$\lambda_L = \sqrt{\frac{m_S}{\mu_0 n_S (2e)^2}}, \tag{2.2}$$

where (2e) is the electric charge of a Cooper pair and λ_L has typical values of a few tens nm [41].
As Cooper pairs could be described by a single valued wave function, the phase difference $\Delta\phi$ along an arbitrary closed path l inside a superconductor has to be a multiple of 2π. For a closed path inside a thick superconductor the supercurrent density is zero and thus the phase difference along this path can be expressed as

$$\Delta\phi = 2\pi \cdot \frac{2e}{h} \oint \vec{A} d\vec{l} = 2\pi \cdot \frac{2e}{h} \int \vec{B} d\vec{F} = \frac{2\pi}{\Phi_0} \cdot \Phi \overset{!}{=} 2\pi \cdot n. \tag{2.3}$$

Accordingly, the magnetic flux Φ inside a superconductor can only take integer values of the magnetic flux quantum Φ_0. Here A is the magnetic vector potential, B the magnetic flux density, F the area penetrated by the magnetic flux and $\Phi_0 = h/2e = 2.07 \cdot 10^{-15}$ Tm^2 is the magnetic flux quantum.

2.2 Josephson junctions

As described in the previous section, the supercurrent is carried by Cooper-pairs. If two superconductors are weakly connected, Cooper-pairs can now exchange between them.
There are different types of how these weak links or junctions can be arranged. Probably the most important type and the one I will focus on within this thesis is the so-called *SIS* Josephson tunnel junction, when a thin insulating layer (*I*) is placed between two superconductors (*S*). The current through a Josephson junction is described by the first Josephson equation $I_C = I_{C,0} \cdot \sin(\phi_1 - \phi_2) = I_{C,0} \cdot \sin(\varphi)$, with φ being the phase difference across the junction [44]. Here $I_{C,0}$ is the junction's maximum critical current which is much lower than the critical current of the superconductor and is determined by the thickness of the insulating barrier t_{ox}, the junction area A_{JJ} and the temperature T.
When the maximum critical current is exceeded, the phase difference across the junction will evolve over time and a dc voltage across the junction V_{DC} appears, described by the second Josephson equation [44]

$$\frac{\partial\varphi}{\partial t} = \frac{2e}{\hbar} \cdot V_{DC} = \frac{2\pi}{\Phi_0} \cdot V_{DC} = \omega_J. \tag{2.4}$$

Here $f_J = \omega_J/2\pi = V_{DC}/\Phi_0 = 483.6$ MHz$\cdot V_{DC}/\mu$V is the Josephson frequency of the alternating current and $\hbar = 1.055 \cdot 10^{-34}$ Js being the reduced Planck's constant.

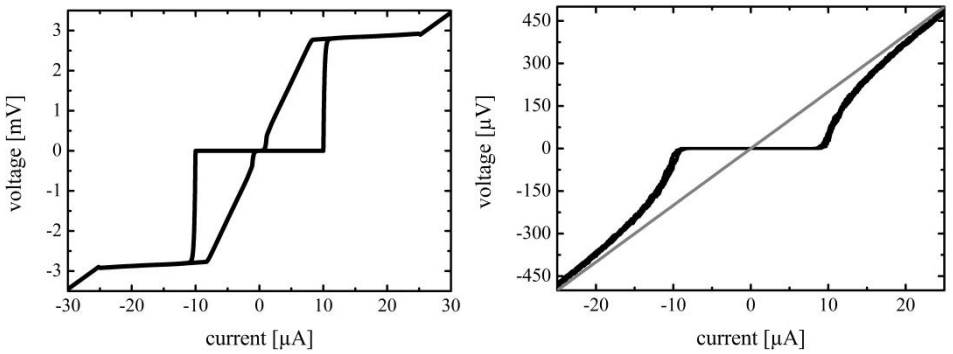

Figure 2.1: Current-voltage characteristics of an undamped (left) and of a damped (right) Josephson tunnel junction. The characteristics result from simulations with JSIM [46, 47], where the following parameters (as will be explained in Chapter 4.1) are used: A_{JJ} = (0.8 x 0.8) μm^2, I_C = 10 μA, R_S = 350 Ω, R_N = 130 Ω, C_{JJ} = 40 fF, V_{Gap}= 2.8 mV and R_{Sh} = 20 Ω. Note that the subgap resistance was intentionally chosen much smaller than experimentally obtained values to illustrate the influence on the subgap branch.

Compared to the Josephson equations, which describe the static state, the dynamics of Josephson junctions is usually described by the RCSJ (resistively and capacitively shunted junction) model. Therein a real Josephson junction is composed of an ideal junction with additional resistance R_N and capacitance C_{JJ} in parallel, describing the tunneling of normal electrons in the voltage state and the displacement current over the capacitance between the two superconducting electrodes. This model is only valid in case of short junctions $a_0 < \lambda_J$, meaning that the phase difference across the junction is a point-like variable, with a_0 being the linear geometric dimension of the Josephson junction. Here

$$\lambda_J = \sqrt{\frac{\Phi_0}{2\pi\mu_0 j_C \left(2\lambda_L + t_{ox}\right)}} \tag{2.5}$$

is the Josephson penetration depth, with $j_C = I_{C,0}/A_{JJ}$ being the critical current density of the junction. With a typical critical current density in this work of about 1.7 kA/cm^2 and $\lambda_{L,Nb}$ of about 86 nm [45], λ_J is about 10 μm, which is well above typical junction dimensions used in the developed devices in this thesis.

A typical I-V characteristic of an undamped junction exhibits a hysteresis, as shown in Figure 2.1 (left). In the simulation I chose R_S = 350 Ω instead of typical achieved values in the kΩ-range to illustrate the influence on the subgap branch. A measure for the hysteresis is the McCumber parameter [48, 49]

$$\beta_C = \frac{2\pi I_C R_N^2 C_{JJ}}{\Phi_0}. \tag{2.6}$$

Typical values for unshunted (0.8 x 0.8) μm^2 Nb/AlO$_x$/Nb SIS Josephson junctions within this thesis are I_C = 10 μA, R_N = 130 Ω, and C_{JJ} = 40 fF, which will be discussed in more detail in chapter 4. This results in a β_C of about 36. Such hysteretic junctions with $\beta_C > 1$ are mostly used in digital applications, where some latching to a defined state is needed [50, 51]. To avoid the hysteresis and in order to obtain a single valued characteristic, an

additional shunt resistor R_{Sh} is usually placed across the junction to damp its dynamics. The value of R_{Sh} should be chosen to satisfy the condition $\beta_C < 1$, which will be the case in all developed sensors throughout this thesis.
Due to the finite thermal energy at $T > 0$, the I-V characteristic of a non-hysteretic junction will be noise-rounded around I_C, as could be seen in Figure 2.1 (right). The ratio between thermal energy $k_B T$ and Josephson coupling energy $E_J = I_C \Phi_0 / 2\pi$ is known as the noise parameter

$$\Gamma = \frac{k_B T}{E_J} = \frac{2\pi k_B T}{I_C \Phi_0} \tag{2.7}$$

and describes the strength of noise-rounding due to thermal or Nyquist noise of the shunt resistor [52, 53]. Here k_B is Boltzmann's constant and T is temperature. The I-V characteristic degenerates to an ohmic behavior for $\Gamma = 1$ as shown in Figure 2.1 (right) as a grey solid line. For LTS dc-SQUIDs the condition $\Gamma < 0.05$ is typically chosen which allows to neglect the influence due to thermal noise rounding. This results in junction critical currents of $I_C > 3.5$ µA at 4.2 K.
As in this thesis Josephson junctions with small area and hence small capacitance will be developed and investigated, I will briefly estimate conditions for intrinsic shunting of Josephson junctions. The well-known relation by Ambegaokar and Baratoff [54, 55] relates the gap-voltage to the critical current and normal state resistance of the junction. For $T \approx 0.5 \cdot T_C$, which is fulfilled for all measurements in this thesis performed in liquid helium at 4.2 K, this reduces to $R_N \approx 0.7 \cdot \pi V_{Gap} / 4 I_C$ [56] and a typical junction critical current of about 10 µA and V_{Gap}=2.8 mV results in R_N of about 154 Ω. Under the assumption that the junction capacitance scales with the junction area this leads to junction dimensions < (0.15×0.15) µm^2 for intrinsic shunted junctions[1], consistent with reported values [57, 58] from theoretical and experimental investigations.
Although typical junction dimensions used herein are well above this limit, one needs to be aware of it from the beginning if new fabrication technologies are developed, which probably get close to the limit. Self-shunting would not only significantly simplify and compress future SQUID designs but most likely further improve their characteristics and facilitate to observe several new properties of Josephson junctions and SQUIDs.

2.3 dc SQUIDs

The dc SQUID, as first proposed by Jaklecvic in 1964 [59], is one of today's most sensitive devices for the detection of magnetic flux. It consists of a superconducting loop with inductance L_{SQ} interrupted by two Josephson junctions, as schematically shown in Figure 2.2. Although there are a variety of other SQUID types, herein I will focus on dc SQUIDs, as these are probably of main significance nowadays. In addition, this thesis will only consider identical Josephson junctions, each with critical current I_C, junction

[1] In this relation the increase of specific junction capacitance due to an increase in critical current density have been neglected. In addition it is known from literature [193], that V_{Gap} decreases for very high critical current densities, which leads to a slight increase in the desired junction size.

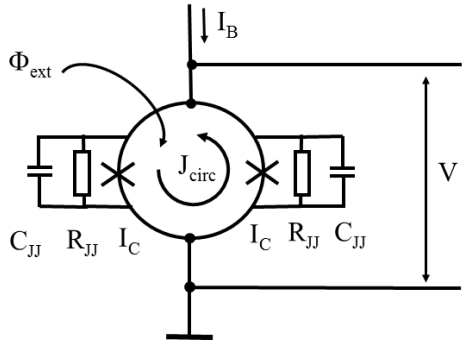

Figure 2.2: Schematic of a dc SQUID with junction critical currents I_C, junction capacitance C_{JJ} and resistor R_{JJ}. The external flux Φ_{ext} results in a circulating screening current J_{circ}, which modulates the measured voltage V, as described in the text.

capacitance C_{JJ} and resistance R_{JJ} as a parallel connection of R_N and R_{Sh}. For a detailed look on SQUID characteristics with non-symmetric SQUID inductance and/ or junction critical currents and shunt resistances, the reader is referred to [60-62].
The critical current of the SQUID is the sum of the junction's critical currents I_{C1} and I_{C2}:

$$I = I_C\left(\sin\varphi_1 + \sin\varphi_2\right) = 2I_C\cos\left(\frac{\varphi_1-\varphi_2}{2}\right)\cdot\sin\left(\frac{\varphi_1+\varphi_2}{2}\right). \tag{2.8}$$

with φ_1 and φ_2 being the phase differences across the two junctions. The difference of them is determined by the magnetic flux in the superconducting loop as

$$\varphi_1-\varphi_2 = 2\pi\frac{\Phi}{\Phi_0} = 2\pi\frac{\Phi_{ext}+L_{SQ}\cdot\left(I_{C1}-I_{C2}\right)}{\Phi_0}, \tag{2.9}$$

with the total flux Φ being the sum of the external flux Φ_{ext} and the flux induced by a circulating current in the loop to maintain flux quantization in the loop.
Therefore, the bias current in a SQUID is redistributed in dependence of the external magnetic flux. For $\Phi_{ext} = n\Phi_0$ no circulating screening current is flowing and the critical current of the SQUID is just $I = 2I_C$, whereas $\Phi_{ext} \neq n\Phi_0$ leads to a suppression of the critical current of the SQUID. The critical current of a SQUID – or in case of a constant current bias the voltage across the SQUID – hence modulates between the two extrema $\Phi_{ext} = n\Phi_0$ and $\Phi_{ext} = n\Phi_0/2$ and has a periodic dependence on Φ_{ext} as shown in Figure 2.3. A measure for the suppression of the critical current of the SQUID is the dimensionless screening parameter

$$\beta_L = \frac{2I_C L_{SQ}}{\Phi_0}. \tag{2.10}$$

The SQUID is typically biased with a dc current $I_B \approx 2I_C$ and converts an external magnetic flux Φ_{ext} or any other physical property that can be transformed into magnetic flux, into a voltage across the SQUID, as can be seen in Figure 2.3 (b). This transducer function is used to accurately measure magnetic flux.
In order to compare SQUIDs with different inductances L_{SQ} one usually refers to the

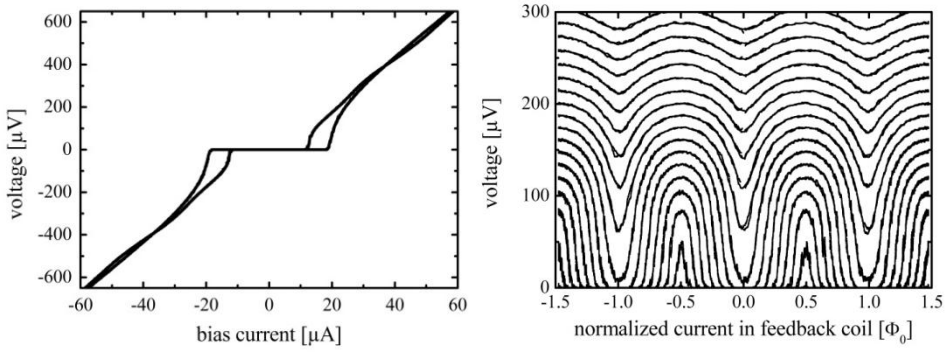

Figure 2.3: Current-voltage characteristics of a SQUID for $\Phi_{ext} = n\Phi_0$ and $\Phi_{ext} = n\Phi_0/2$ and corresponding flux-voltage characteristics. The data was simulated using JSIM, with junction parameters as given in Figure 2.1 and L_{SQ} = 130 pH.

energy resolution ε, i.e. the energy of the signal equal to the intrinsic noise energy in the unit bandwidth. The intrinsic noise of the SQUID is determined by the measured voltage power spectral density S_V. This noise limits the flux resolution in the SQUID $\Phi_n^2(f) = S_\Phi(f) = S_V(f) / V_\Phi$ where S_Φ and V_Φ are called equivalent flux noise power spectral density and SQUID transfer function, respectively. Accordingly the equivalent energy resolution is $\varepsilon = S_\Phi/2L_{SQ}$. The phrase "equivalent" will below be omitted herein.

Assuming that at 4.2 K the dominant white noise source is the Nyquist noise of the shunt resistors, the energy resolution and the transfer function of SQUIDs are given by $\varepsilon = 9k_BTL_{SQ}/R_{JJ}$ and $V_\Phi = R_{JJ}/L_{SQ}$ [63, 64]. Accordingly the optimum energy resolution of the SQUID for $\beta_C \approx 1$ and $\beta_L \approx 1$ [63, 65] can be derived as a function of SQUID inductance L_{SQ} and junction capacitance C_{JJ} as

$$\varepsilon = 16k_BT\sqrt{L_{SQ}C_{JJ}} \tag{2.11}$$

and the flux noise as

$$\sqrt{S_\Phi} = \sqrt{2L_{SQ}\cdot\varepsilon} = 4L_{SQ}^{3/4}C_{JJ}^{1/4}\cdot\sqrt{2k_BT} \tag{2.12}$$

This relation clearly prescribes the way how to improve the SQUID performance: the energy resolution of the SQUID is significantly improved by reducing the SQUID inductance, the working temperature, and the junction capacitance.

However, for practical applicable sensors the coupling to an external signal imposes a lower limit for the SQUID inductance, as the effective area of e.g. a square washer SQUID scales with the linear dimension of the washer hole, which in turn is proportional to L_{SQ}. Hence, there is a tradeoff between a small inductance for a high energy resolution and a sufficiently large inductance for a sufficient effective area and therefore for adequate coupling to external signals.

Whereas the choice of working temperature in scientific questions is most probably limited by the technical facility of the according laboratory, applications as e.g. intended for field operation often restricts to liquid helium temperature at normal pressure. Beside this, the possible impact of developed systems on existing markets also strongly depends on the acceptance of customers to use liquid helium, as this influences both the operator's convenience and costs. As helium is a rare resource, the tendency to use dry cooling-

systems will therefore presumably gain a lot more importance in the future.
To further enhance the SQUID performance, the total junction capacitance C_{JJ} and hence the junction size should be reduced, which is typically limited by the used fabrication process. Furthermore, small area junctions can take advantage of their low capacitance only if careful attention is also been paid on the immediate surroundings of the junctions. An undesired parasitic capacitance $C_{JJ,p}$ of the junction originated by an overlap of superconducting electrodes may affect the performance of superconducting devices. In fact, a low parasitic capacitance is essential for SQUIDs described in this thesis and will be treated in much more detail in chapters 3 and 4.
Additionally, the transfer function V_Φ can also be expressed as a function of SQUID inductance L_{SQ} and junction capacitance C_{JJ} for β_C and β_L about unity:

$$V_\Phi = \frac{R_{JJ}}{L_{SQ}} = \sqrt{\frac{1}{\pi L_{SQ} \cdot C_{JJ}}}. \tag{2.13}$$

As the usable voltage swing across the SQUID is about $\delta V \approx \pi \cdot V_\Phi$ for sinusoidal flux-voltage characteristics, a reduction of the total junction capacitance is not only favorable in respect to a high energy resolution and low flux noise, but will also increase the transfer function and thus the usable voltage swing of the SQUID.

In the previous description of SQUID performance I restricted the discussion to the frequency independent white noise. Above a 1/*f* corner frequency of typically a few Hertz the SQUID response is flat until the operation frequency of the sensor. As the desired system will measure signals in the range between 1 Hz to about 10 kHz, as described in chapter 1 in more detail, I will now briefly comment on possible sensor limitations in the low-frequency range of typically below 10 Hz.
Actually two sources of low-frequency noise in low-T_C SQUIDs have been identified. According to [40, 66] one can distinguish between fluctuations in critical currents of the Josephson junctions and flux noise.
It is generally accepted, that critical current fluctuations originate in a random trapping and release of electrons in defect states in the junction barrier and therefore locally change the barrier height and in this way the critical current of the Josephson junction. The change of this potential leads to a random telegraph noise. The superposition of many of these fluctuations each with an own characteristic life-time leads to a 1/*f* dependence of the power spectral density of the flux noise S_Φ [67-69].
Reference [70] gives a relation for the magnitude of critical current fluctuations in Josephson junctions combining measurement data of junction areas ranging from 4 to 100 μm^2 made from various superconducting materials as niobium and lead and including different junction barrier materials as AlOx, InOx and NbOx. Thereafter, at 4.2 K one can write the spectral density of the critical current noise at 1 Hz as

$$S_{I0}\left(1\text{Hz},\ 4.2\,\text{K}\right) = 144 \frac{\left(I_C/\mu\text{A}\right)^2}{A_{JJ}/\mu\text{m}^2} \frac{\left(\text{pA}\right)^2}{\text{Hz}}. \tag{2.14}$$

According to this formula, Josephson junctions with an area of $(0.8\times0.8)\ \mu m^2$, a critical current $I_C = 10\ \mu A$ and an assumed current sensitivity $M_{dyn} = R_{dyn}/V_\Phi \approx (1\ldots2)\cdot L_{SQ}$ [71] for a SQUID with $L_{SQ} \approx 130\ pH$ at 4.2 K would lead to a flux noise of about

(10…20) $\mu\Phi_0/\mathrm{Hz}^{1/2}$. Here R_{dyn} is the dynamic resistance of the SQUID in the working point.

In contrast, it is commonly accepted, that flux noise arises from movement of trapped vortices in the SQUID washer. As the power spectral density of flux noise scales with V_Φ [66], this contribution vanishes in working points with $\partial V/\partial \Phi = 0$ whereas critical current fluctuations do not. This allows for independent estimations of contributions of critical current and flux noise. In addition, the affinity to trap flux in superconducting structures can be expressed by calculating Gibbs free energy as e.g. done in [72-75]. Accordingly a small size of the superconductor at or nearby the junction is usually favorable to prevent vortex trapping in the superconductor during cool-down. By reducing the linewidth w of superconducting structures to below $\approx (\Phi_0/B)^{1/2}$ this noise should in principle be eliminated.

More recently another source of low-frequency flux noise was identified, but up to now there is no comprehensive understanding of this phenomena and the microscopic origin. It is currently believed that this low-frequency flux noise originates from single electron spins located on the surface of the superconductor. For example in [76] the noise is generated by spins of unpaired electrons hopping on and off defect states due to thermal activation. In this case, the direction of the spins would be locked as long as the electrons are trapped, thus contributing magnetic signal. The superposition of many uncorrelated changes of spin direction would thus sum up to the observed $1/f$ power spectrum. As this source of noise may determine the decoherence time in qubits [77], up to now main investigations are related to very low temperatures as typically used for qubit operation and target on rather low loop dimensions in the µm range. I will discuss this noise contribution in more detail in chapter 5 and will compare recent theories with the observed low-frequency noise dependence of the developed SQUIDs.

2.4 SQUID electronics

The SQUID itself acts as a very sensitive magnetic flux to voltage transducer with nonlinear periodic flux to voltage characteristic and is the major part of the measurement system. In order to obtain a one to one dependence of the voltage over the SQUID from the flux in the SQUID loop and to make use of this sensitivity an adequate SQUID electronics is required.

Within this thesis a directly coupled electronics is used, as schematically shown in Figure 2.4. Due to a more compact design, the suitability for use in multi-channel systems, a sufficient large bandwidth and dynamic range as well as lower power consumption, this type of electronics is adequate for a geophysical receiver system. Solely to investigate the low-frequency noise performance of the developed sensors in Chapter 5.7 a flux-modulated electronics is used.

As described above, the flux quantization in a superconducting ring leads to a periodic, nonlinear voltage dependence of the SQUID on the applied external signal flux Φ_{Sig}. It therefore acts as a flux-to-voltage transducer with a very limited linear working range Φ_{lin}. The SQUID electronics or flux-locked loop (FLL) measures this voltage across the

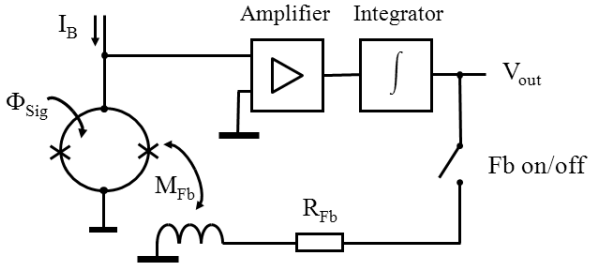

Figure 2.4: Schematics of direct coupled SQUID electronics. R_{Fb} denotes the feedback resistor, M_{Fb} the mutual inductance between feedback coil and SQUID. The external signal Φ_{Sig} coupled to the SQUID is transformed into a voltage, amplified and integrated and fed back as a feedback flux into the SQUID via M_{Fb}. The output voltage V_{out} is therefore linear dependent on the applied flux Φ_{Sig}.

SQUID, amplifies and integrates the signal and feeds it back as a feedback flux Φ_{Fb} to the SQUID via a feedback resistor R_{Fb} and mutual inductance M_{Fb}, as depicted in Figure 2.4. It therefore keeps the flux $\Phi_{Sig} + \Phi_{Fb}$ inside the SQUID constant and the output voltage becomes linearly dependent on the applied external signal threading the SQUID loop with a strongly increased linear working range.

Besides the linearization, the main purpose of the electronics is to read out the voltage across the SQUID without compromising the low voltage noise level of the SQUID. The influence of the read-out electronics on the total flux noise $S_{\Phi,t}^{1/2}$ can be expressed as [71]

$$\sqrt{S_{\Phi,t}} = \sqrt{\left(\sqrt{S_{\Phi,SQ}}\right)^2 + \left(\frac{\sqrt{S_{V,Amp}}}{V_\Phi}\right)^2 + \left(\sqrt{S_{I,Amp}} \cdot M_{dyn}\right)^2}. \qquad (2.15)$$

Here $S_{\Phi,SQ}^{1/2}$ is the intrinsic flux noise of the SQUID, $S_{V,Amp}^{1/2}$ and $S_{I,Amp}^{1/2}$ the preamplifier input voltage and current noise, respectively. This relation does not account for noise contributions due to thermal noise in the feedback resistor. However, in applications for unshielded operation of SQUID sensors this may become important or even dominant.

This becomes visible as one can write the system slew-rate as a figure of merit in systems for unshielded operation as [78, 79]

$$\dot{\Phi}_{max} = \left|\frac{\partial \Phi_{Fb}}{\partial t}\right| = 2\pi \cdot f_{GBP} \cdot \delta V \cdot \frac{M_{Fb}}{R_{Fb}}. \qquad (2.16)$$

Here f_{GBP} is the gain-bandwidth product, a fixed value for a specific amplifier configuration. A high system slew-rate therefore demands a small feedback resistor, which itself produces current noise as $S_I^{1/2} = (4k_BT/R_{Fb})^{1/2}$. Via the inductive coupling to the SQUID with M_{Fb} this noise on the other hand converts in flux noise in the SQUID. For a high slew-rate a large usable voltage swing is therefore desirable. According to relation (2.13) this can be achieved by a reduced total junction capacitance. This will be subject of the subsequent chapter.

3 LTS cross-type Josephson tunnel junctions

The main parameters of Josephson junctions and characteristics determining intrinsic sensitivities of dc SQUIDs have been reviewed in Chapter 2. In relations (2.11) to (2.13) the demand for small capacitance and therefore small area Josephson junctions clearly became visible. The request to shrink the dimensions of the Josephson junctions is not limited to SQUIDs but to almost all applications in superconducting electronics, like in mixer elements in cryogenic low noise receivers [80], for the observation of Coulomb blockade effects [81], in rapid single flux quantum logics [58, 82] or in circuits for quantum computation [83].
This chapter reviews current typically used fabrication technologies and discusses their advantages and limitations. A possible solution will be given in Chapter 3.2 where the approach of cross-type Josephson tunnel junctions is explained in detail.

3.1 State of the art fabrication technologies

Niobium-aluminum-niobium based Josephson junctions proposed by Gurvitch et al. [84] have emerged as the material of choice for most of today's superconducting electronics because of their good performance, reproducibility and reliability. There has been continuous progress in other material systems, but up to now none of them gained these importance and propagation in LTS electronics, especially in applications requiring superior performance with respect to low-frequency noise. I will therefore restrict the discussion on state of the art fabrication technologies mainly to $Nb/AlO_X/Nb$ junctions.
Typical fabrication methods for small area Josephson tunnel junctions are shown in an overview in Figure 3.1. Most of currently used fabrication technologies can be attributed to one of these or represent variations of these processes.
Commonly, $Nb/AlO_X/Nb$ Josephson tunnel junctions are prepared by the deposition and patterning of an Nb base layer and the subsequent in situ deposition of the entire trilayer [85]. Thereafter, the upper electrode of the trilayer is either etched or anodizes [86, 87], or sometimes just the sidewalls of the trilayer are anodized [88]. In addition, fabrication technologies which make use of chemical mechanical polishing (CMP) to planarize the trilayer structure have been reported [88, 89]. An insulating layer is deposited as a last step, including vias to the top electrode and an additional Nb metallization layer which is deposited on top thereby providing a connection to the top electrode.
This method - although completely accepted and used in practice - has some shortcomings: e.g. tolerances in the lithography require wider metallization traces than the

junction dimension itself which produces a substantial parasitic capacitance $C_{JJ,p}$ in parallel to the junction capacitance. Improved lithographic tools for better alignment of the junction trilayer and the metallization wires and the use of insulation material with low ε_r such as SiO_2 instead of Nb_2O_5 [90] may ameliorate this problem. However, as the junction size is reduced to submicron dimensions the parasitic capacitance will become more pronounced or even dominant.

The reproducible definition of the junction size in this technology seems to be limited to linear dimensions of about 2 µm [79]. For smaller junction areas the formed Nb_2O_5 during the anodic oxidation tends to creep under the resist and possibly lift them off what results in malfunction of the junction. Using circular junctions [92, 93] or a hard-mask [94, 95] could move this limit somewhat towards smaller junction sizes, but the fabrication of low-capacitance deep sub-micrometer Josephson junctions seems to be limited in this so-called window-type technology.

More recently a fabrication technology is reported [96] which enables the fabrication of very small SIS Josephson tunnel junctions by making use of a quasi-planarized process and a pretreating of the photoresist to prevent undesired lift-off. Thus, step heights could significantly be reduced, allowing electron beam lithography also in the top wiring layer and hence high-quality Josephson junctions with linear dimensions of down to about 170 nm to be fabricated. Nevertheless, still an undesired parasitic capacitance in parallel to the junction capacitance is formed and up to now it is an open question if this planarization process is feasible on a wafer-scale.

Deep sub-micrometer Josephson junctions have also been fabricated e.g. by focused ion beam etching [81], focused ion beam writing [97, 98], focused ion beam implantation [99, 100], shadow evaporation [101] or edge-type junctions [102-104].

Whereas the first all make use of high-resolution lithography tools, the latter one provides a simple method for very small junction areas even with standard photolithography tools. The junction area is here defined at the ramp of the counter electrode and with minimum feature sizes of about 2 µm Josephson junctions with areas down to about 0.4 μm^2 seem to be possible [56]. The main limitation in this technology arises from strongly varying resistances in parallel to the junctions which emerge from the underlying aluminum layer

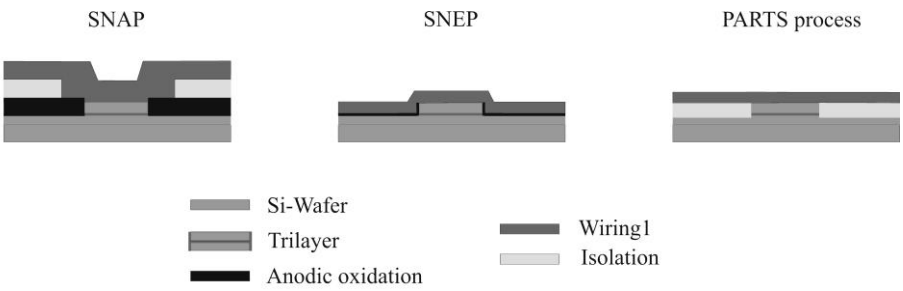

Figure 3.1: Cross-section of typical fabrication technologies for Nb/AlO_x/Nb Josephson tunnel junctions. SNAP denote the selective niobium anodization process [85], SNEP the selective niobium etch process [84] and PARTS the planarized all-refractory technology for low-T_C superconductivity, as introduced in [91]. Note that all of them exhibit a parasitic capacitance in parallel to the junction capacitance due to the overlap between wiring layers.

and are hard to control. Furthermore, as described in [56] the critical current of the junctions shows a strong temperature dependence due to the proximity effect between the niobium and the aluminum layer which restricts the operation to a very limited temperature range.

3.2 Cross-type Josephson junction technology

To overcome the above mentioned limitation in respect to minimum junction size and parasitic capacitance, a fabrication process was developed where the junction is defined by the overlap of two narrow perpendicular strips, as described in [105]. The process is similar to the work in [87, 106-108]. As in these references, any unnecessary overlap of the wiring layer with the base electrode is avoided. Differences to the approach presented therein concern the type of planarization, whether or not the sidewalls are anodized, the type of mask used, and if the junction is defined by etching the entire trilayer or only the counter electrode.

The fabrication flow for the cross-type process is schematically shown in Figure 3.2. The junction fabrication is started with the deposition of the entire Nb/AlO_x/Nb trilayer (a) with 150 nm Nb, 12 nm Al and 100 nm Nb on a 500 µm thick 4 inch silicon wafer. A silicon wafer without thermal oxide is used in order to protect the junctions from electrostatic discharge at room temperature. The oxidation of the Al layer is done in the load-lock chamber of our deposition system in pure oxygen atmosphere. Detailed information on oxidation parameter will be given in Chapter 4 together with results of the junction's characteristics.

Subsequently, the complete trilayer is patterned as a strip with a width corresponding to one linear dimension of the junction (b). Therefore, photolithography is performed with

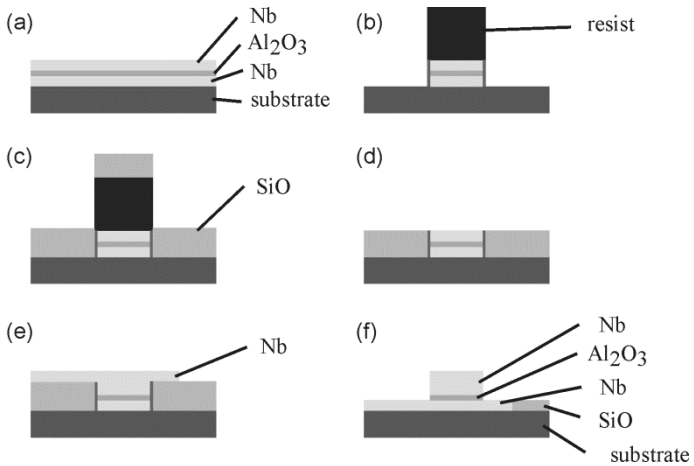

Figure 3.2: Cross section of layers for junction definition in the cross-type technology, as explained in the text. Please note, that (f) is rotated by 90° with respect to (a) – (e). The thicknesses of layers are not to scale.

an i-line stepper providing a minimum feature size of about 0.6 µm, where a 1.5 µm thick photoresist of type AZ5214E is used. The patterning is done with reactive ion etching in CF_4 and sputter etching of the trilayer. To prevent shortcuts across the junction barrier due to possible redeposit from the dry etching process, a sidewall anodization is performed at 25 V. The residues at the sidewall of the trilayer, as can be seen in the completed junction in Figure 3.3, probably originate from re-deposits but do not seem to have any measureable detrimental effect.
Next step is the deposition of SiO (c) of the same thickness as the trilayer, which levels out the step for subsequent layers and leads to a planarized trilayer (d). In this procedure the photoresists for trilayer patterning still remains in place. The resulting trenches beside the trilayer (cf. Figure 3.3) result from a shadowing effect of the photoresist during the deposition on the tilted and rotating wafer. This problem may be overcome by a first lift-off of the resist and a subsequent chemical mechanical polishing of the SiO_x for leveling. However, as no detrimental influence of this trench is observed, this simplified procedure without CMP will be used within this thesis.
Subsequently, a 200 nm thick Nb layer (called wiring 1) is sputter deposited on top. The patterning of this layer as well as the Nb top electrode of the trilayer by reactive ion etching with CF_4 in terms of a strip perpendicular to the trilayer strip results in rectangular junctions (e + f). In this case, the aluminum of the trilayer serves as a natural etch stop. The junction area is therefore defined by the overlap of these two perpendicular strips with junction dimensions according to the width of these strips. Figure 3.3 shows a scanning electron microscope image of a cross-type Josephson tunnel junction with linear dimensions of $(0.6 \times 0.6)\ \mu m^2$, representing the minimum feature size of the used lithography tool.
This self-aligned process for the definition of the junction area and its simplicity with only two lithographic steps are the main advantages of this approach. In addition downsizing the junction area and avoiding any idle region – the undesired overlap between superconducting electrodes around the junction which results in a parasitic capacitance in parallel to the junction capacitance – allows meeting the demand of a small total capacitance of the Josephson junction stated in relation (2.11) and (2.12). A detailed

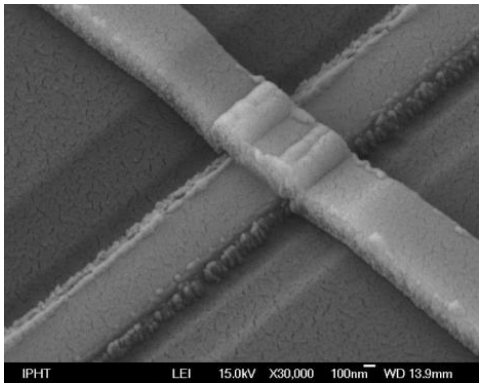

Figure 3.3: Scanning electron microscope image of a cross-type Josephson tunnel junction with linear dimensions of $(0.6 \times 0.6)\ \mu m^2$.

analysis of the junction capacitance will be given in Chapter 4.3. Furthermore, any other metallization around the junction can be avoided, resulting in maximum superconductor dimensions equal to the linear dimension of the junction, which will be discussed in more detail in Chapters 5.4 and 5.5.

In addition to these layers which are used for junction definition, the fabrication of complete SQUID sensors requires several additional layers. Table 3.1 lists all layers which are used for the sensors described in this thesis. In Figure 3.4 a cross-section of a stack of the whole layer packet is shown. One can see that the first niobium wiring layer in addition to the junction definition is typically used as a metallization layer for the SQUID washer.

After completion of the junction definition native oxides on the niobium will be removed for the via definition in order to ensure good electrical contact to subsequent layers and to allow a cut of additional wiring lines by reactive ion etching with CF_4, which have been used for the sidewall anodization of the junctions.

The following two layers of thermally evaporated SiO provide electrical isolation between the upper and niobium wiring layer. To avoid shortcuts due to pinholes in SiO, a two-step lift-off process is used, where a separate resist-mask with a cleaning step in between is used to remove particles from the surface. Each layer is about 400 nm thick to ensure a small capacitance between the two niobium wiring layers.

The subsequent sputter deposition of the second wiring layer of 300 nm thick niobium provides a connection of the Josephson junctions with the following resist layer to damp their dynamics and additionally enables the implementation of integrated coils on top of the SQUID washer. To prevent an etching of underlying structures a 12 nm thin aluminum layer is deposited immediately before the wiring layer which serves as a natural etch stop for the reactive ion etching of this layer.

The following layer of sputter deposited AuPd is on one hand used for the shunt resistors for the Josephson junctions and on the other hand to cover the bond pads to enhance the adhesion to bonding wires. The typical thickness of 100 nm results in a sheet resistance of about $4\,\Omega$/square. For moderately damped $(0.8 \times 0.8)\,\mu m^2$ Josephson junctions this results in a typical shunt dimension of about 5.5 squares. Furthermore, the decrease in layer thickness allows for more compact designs which may be advantage in e.g. SQUID

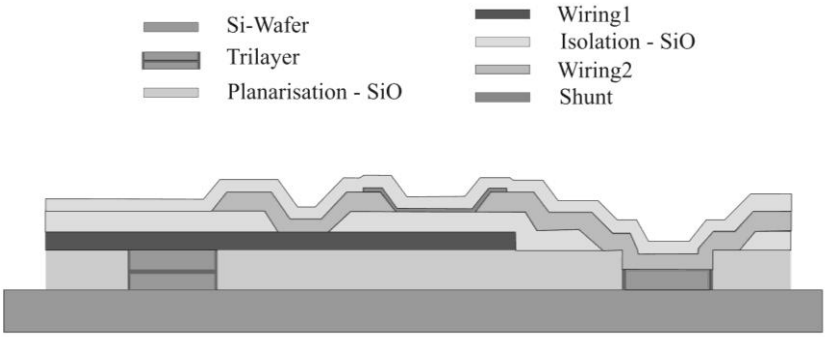

Figure 3.4: Cross-section view of complete stack of layers for the fabrication of SQUID sensors within the cross-type Josephson junction technology.

Table 3.1: List of layers used in the cross-type technology for the fabrication of SQUID sensors.

layer function	material	thickness [nm]	deposition method	patterning method
Trilayer	Nb/Al-AlOx/Nb	150/12/100	sputtering	RIE (CF4)
Nb wiring 1	Nb	200	sputtering	RIE (CF4)
Via definition				RIE (CF4)
Cut				RIE (CF4)
Isolation 1	SiO	400	thermal evaporation	Lift-off
Isolation 2	SiO	400	thermal evaporation	Lift-off
Nb wiring 2	Nb	300	sputtering	RIE (CF4)
Resistor	AuPd	100	sputtering	Lift-off
Protection	SiO	400	thermal evaporation	Lift-off

current sensors or amplifiers.
Finally, a 400 nm thick layer of SiO is thermally evaporated and patterned by lift-off in order to mechanically protect the complete circuitry.

4 Junction Characterization

In the last chapter conventional state of the art technologies for the fabrication of small area Josephson junctions and their limitations with respect to e.g. minimum achievable junction sizes or process reliability has been described. These considerations led to the introduction of the cross-type fabrication technology which enables downsizing of the junction areas into the sub-micron range as well as avoiding any unnecessary parasitic capacitance in parallel to the junctions, limiting the performance of superconducting electronic devices.
Within this chapter I will provide a detailed look on electrical characteristics of the fabricated junctions as well as on the scalability of the presented approach. Furthermore, the current density profile over the junction width is obtained from Fraunhofer diffraction pattern measurements, as will be shown in detail in Chapter 4.2. From Fiske step measurements the specific junction capacitance is obtained representing one of the main figures of merit for the presented approach.

4.1 Electrical characterization

For the electrical characterization of Josephson junctions and SQUIDs a measurement setup developed at IPHT Jena, as schematically shown in Figure 4.1, was used. It consists of three individual galvanically isolated ground potential free current sources and a low-noise differential amplifier. Each current source can be controlled with either external or internal generator and allows to adjust a dc current as well as to drive current sweeps. It can be tuned in steps to ranges of 1 µA/V to 10 mA/V, each step with an increased amplitude factor of ten. The current running through the junction is measured via a monitor. The gain of the amplifier could be adjusted to values from 1 to 1000 in steps of ten. Whereas for the characterization of single junctions just one current source was used,

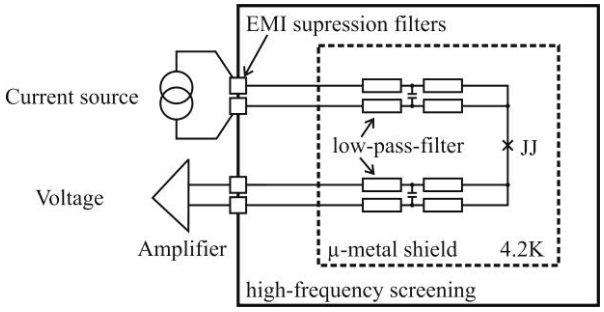

Figure 4.1: Measurement setup for the electrical characterization of Josephson junctions.

the other two were used for the characterization of SQUIDs with integrated feedback- and input-coils which will be discussed in Chapter 5.
For data recording a CompactDAQ system from *National Instruments* [109] was used. A PC allows to adjust the measurement conditions via a Labview-Software [110] developed at IPHT Jena [111]. The typical frequency for current sweeps ranges from 1 to 100 Hz.
All measurements for the electrical characterization of the Josephson junctions were done while the samples were immersed in liquid helium at 4.2 K inside a µ-metal shield. The bias-lines were low-pass filtered inside the dipstick at room-temperature and at 4.2 K. A typical current-voltage characteristic of a (10 × 10) µm^2 cross-type Josephson junction can be seen in Figure 4.2, where specific parameters which were used for junction characterization are depicted.
Therein one can see the junction critical current I_C, the current at the gap I_{Gap} and the gap voltage V_{Gap}, the normal state resistance R_N, which is defined at 4 mV, and the subgap resistance R_S defined by the current at 2 mV. High quality junctions are characterized by a low subgap leakage current and a therefore high R_S/R_N ratio. In addition, values like a high I_CR_N-product, for Nb-based junctions in the range of (1.5-1.8) mV and a high quality parameter $V_m=I_CR_S$, with typical values of about (40-70) mV indicate a high junction quality.
As deviations in the measured critical current may occur because of e.g. thermal noise, high-frequency disturbances or tolerances in the junction dimension due to the used lithography tool, within this thesis the critical current density is determined on rather large Josephson junctions with linear dimensions of (10 × 10) µm^2. The critical current density for the junction shown in Figure 4.2 is therefore 1.8 kA/cm^2.
As the aim of the development is the reliable and reproducible fabrication of high quality Josephson junctions and SQUIDs, a decision was taken not to work at the technical limit of the used projection lithography tool, as in this case deviations due to the lithography will most likely show larger effect on device characteristics. The used i-line stepper enables minimum feature sizes of about 0.6 µm. Therefore, from the desired linear junction dimensions of about 0.8 µm to 1 µm and the self-imposed target parameter of a

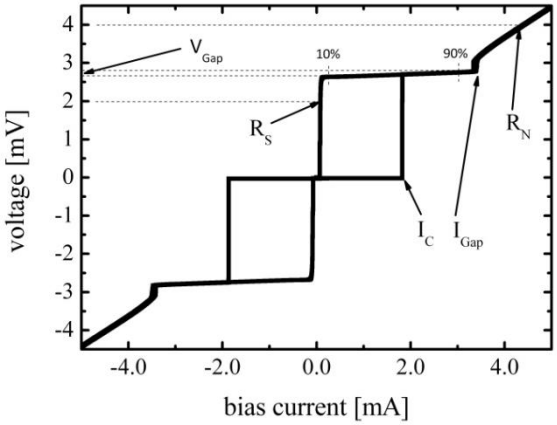

Figure 4.2: Typical current-voltage characteristic of a (10 × 10) µm^2 Josephson junction measured at 4.2 K and corresponding parameter for junction characterization as explained above.

junctions critical current of about 10 µA to 15 µA, the required critical current density results to about 1.7 kA/cm^2.

To meet this criterion, the dependence of the junction's critical current density j_C on oxygen exposure during the formation of the AlO_x barrier was investigated. Figure 4.3 shows the dependence obtained on Josephson junctions with linear dimensions of (10 × 10) µm^2 and a linear fit of the data to $j_C = 3500\ \mathrm{A/cm^2} \cdot x^{-0.47}$, with x being the oxygen exposure in units [mbar·minutes] as a solid line. The dashed lines represent deviations of ± 20% from this dependence. In addition typical relations as given in the literature [96, 112] are shown, indicating the general agreement. Deviations may result from specific properties of the used deposition systems, substrate temperature during Nb sputtering or possibly indicate the influence from contaminations in the oxidation chamber.

For critical current densities in the range of 70 A/cm^2 to 300 A/cm^2 an oxygen pressure of about 10 mbar was used, whereas higher critical current densities require an oxygen pressure of about 1 mbar or less for a reproducible control of the critical current density. Josephson junctions with j_C-values up to about 20 kA/cm^2 have been fabricated, where the latter were carried out for the fabrication of even smaller junction sizes, which are not the main subject of investigations in this thesis and will be shortly discussed in the Appendix. If not stated otherwise in the following a critical current density of about 1.7 kA/cm^2 was used herein.

The choice of this critical current density moreover enables the combination of sensitive superconducting sensors, typically working at or close to the thermal limit at 4.2 K, and digital logic and interface circuits to room-temperature electronics with typical critical currents in the range of 125 µA to 500 µA. Even for this large spread of junctions critical currents, the presented cross-type process may allow integrated superconducting mixed signal applications for unshielded operation, in which all junction sizes are below the limit $(\Phi_0/B)^{1/2}$ for vortex trapping during cool-down in Earth's field. This fact may gain

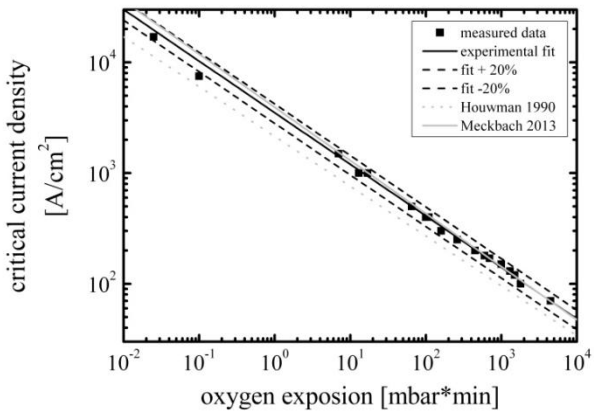

Figure 4.3: Dependence of the critical current density on oxygen exposure. In addition to the measured values, shown as filled squares, an experimental found scaling law is depicted as a solid line. The black dashed lines represent deviations of ± 20% from this experimental fit. Moreover the figure shows dependences from the literature, as given in the text.

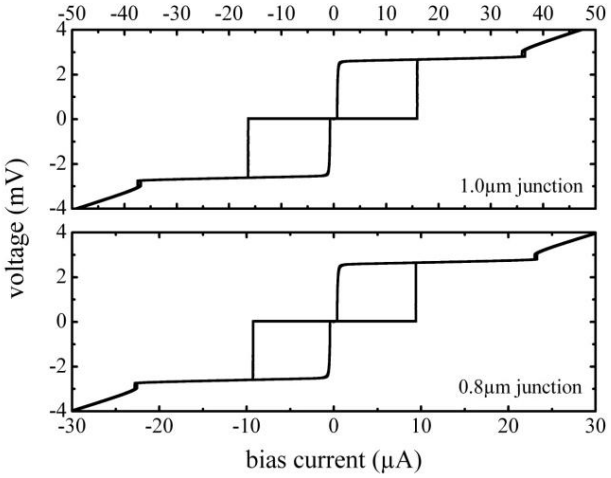

Figure 4.4: Current-voltage characteristics of unshunted Josephson tunnel junctions of size (1.0 × 1.0) µm^2 (top) and (0.8 × 0.8) µm^2 (bottom).

its importance e.g. in combination of future superconducting radiation detectors with integrated digital readout circuits [113, 114].

Within the cross-type technology square-shaped Josephson junctions with linear dimensions of 10 µm down to 0.6 µm have been fabricated. Figure 4.4 shows typical current-voltage characteristics of Josephson junctions with dimensions of (1.0 × 1.0) µm^2 (top) and (0.8 × 0.8) µm^2 (bottom).

Table 4.1 lists characteristic parameters for various junction sizes. The good superconducting properties of the niobium electrodes can be seen in the high gap-voltage of about 2.8 mV. Furthermore, the high ratio of the subgap to normal-state resistance of about 40 and quality-parameters of about 45 mV, independent of the junction size, indicate the high quality of the junctions. In addition one can see, that critical currents in

Table 4.1: Characteristic parameters of cross-type junctions measured at 4.2 K.

junction size (µm^2)	(0.6×0.6)	(0.8×0.8)	(1.0×1.0)	(1.5×1.5)	(3.0×3.0)	(10×10)
I_{Gap} (µA)	13.5	23.5	37	76	320	3400
V_{Gap} (mV)			~ 2.8			
I_C (µA)	4.8	9.2	16	30	160	1850
R_N (Ω)	225	131	82.5	44	10	0.91
R_S (kΩ)	10.0	5.0	2.86	1.5	0.31	0.024
R_S/R_N	44	38	35	34	31	26
I_CR_S (mV)	48	46	46	45	50	44
I_CR_N (mV)	1.08	1.21	1.32	1.32	1.6	1.68

the range of about 10 µA tend to be slightly suppressed, which is most likely due to radio-frequency interferences. Therefore, the $I_C R_N$-product of the smaller junctions decreases due to the decreased measured I_C's, which do not necessarily need to represent the internal limit of the junctions.
Nevertheless, even for the smallest junctions no relative increase in the subgap current was observed, which leads to the conclusion, that the transparency of the tunnel barrier is dominated by its intrinsic properties and not by edge effects. Accordingly it should be possible to extend this technology to even smaller junction sizes by use of lithography tools enabling smaller feature sizes, as will be discussed in the Appendix.
In conclusion, these electrical parameters indicate very high quality Josephson junctions which should be suitable for the fabrication of highly sensitive SQUIDs.

4.2 Junction quality – Fraunhofer diffraction pattern and calculation of the current density profile

In addition to the electrical characterization, the magnetic field dependence of the maximum critical current, the so-called Fraunhofer diffraction pattern, has been measured for a variety of cross-type Josephson junctions. For these measurements a magnetic field was applied in plane of the junction barrier by a superconducting magnet from Oxford Instruments operated in the persistent current mode [115]. A schematic of the measurement setup is shown in Figure 4.5.
With the setup for the electrical characterization of Josephson junctions, as described earlier, for each value of the background magnetic field the corresponding current-voltage characteristic was recorded, while the Josephson junctions have been immersed in liquid helium at 4.2 K. Figure 4.6 shows the measured normalized maximum critical current as a function of the external magnetic flux for cross-type Josephson junctions with linear dimensions of (1.5×1.5) µm^2 and (0.6×0.6) µm^2 as an example. The maximum critical current amounts to 38.5 µA and about 4 µA for the (1.5×1.5) µm^2 and (0.6×0.6) µm^2 junctions, whereas the first minima correspond to about 11.5 mT and 38.8 mT,

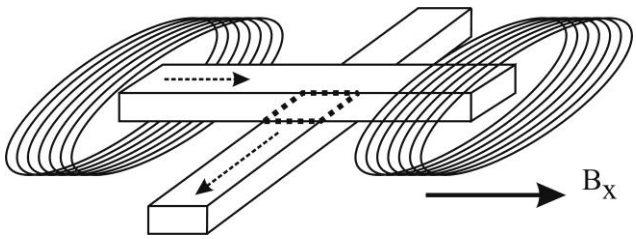

Figure 4.5: Measurement setup used to determine the magnetic field dependence of the maximum critical current of the cross-type Josephson junctions. The magnetic field was applied in plane of the junction barrier, indicated with a dashed square. The arrows indicate the bias current through the junction.

respectively.

It should be emphasized, that the critical current reduces to zero indicating a homogeneous thickness of the oxide tunnel barrier. Moreover, the general dependency roughly agrees with the expected $\sin(x)/x$ model for rectangular junctions in the short junction limit [116]. Deviations due to self-field effects of currents flowing through the junctions can be neglected, as the ratio of the linear dimension of the junctions to the Josephson penetration depth λ_J is about 0.15 for the (1.5 × 1.5) μm^2 junctions and about 0.05 for the (0.6 × 0.6) μm^2 junctions.

As pointed out in [117, 118] it was found that the measured data could be best described by a model representing a symmetric and convex current density distribution over the junction width, given by the relation

$$\frac{I_C(\Phi_{ext})}{I_0} = \left| \frac{1+\cosh\kappa}{\cosh\kappa} \cdot \frac{\sin\Phi^*}{\Phi^*} - \frac{1}{\kappa^2+\Phi^{*2}} \cdot \left[\Phi^* \cdot \sin\Phi^* + \kappa \cdot \tanh\kappa \cdot \cos\Phi^* \right] \right|, \tag{4.1}$$

with the flux ratio

$$\Phi^* = (\pi \Phi_{ext}/\Phi_0). \tag{4.2}$$

Here $\kappa = \alpha l/2$, where α specifies the decrease of the current density at the boundary of the junction and l being the junction width. The solid lines in Figure 4.6 represent least square fits of the measured data to this relation with $\kappa = 1.23 \pm 0.08$ and $\kappa = 1.06 \pm 0.06$ for the (1.5 × 1.5) μm^2 and (0.6 × 0.6) μm^2 junction, respectively.

The current density profile can be obtained by the Fourier transformation of equation (4.1), as in detail explained in [116] for the opposite case of a concave current density distribution. One can therefore write

$$j(x) = j_0 \cdot \frac{1+\cosh\left(\frac{\alpha l}{2}\right) - \cosh(\alpha x)}{\cosh\left(\frac{\alpha l}{2}\right)}. \tag{4.3}$$

Figure 4.7 shows the current density profiles along the junction width of the two junctions

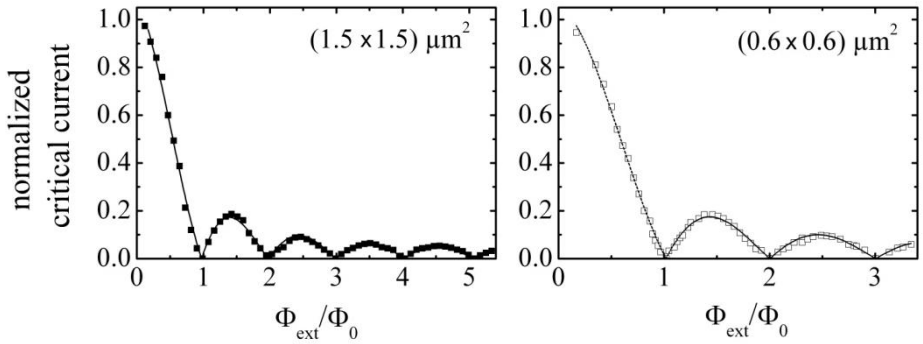

Figure 4.6: Measured normalized maximum critical current of the Josephson junction as function of external magnetic flux and best fit according to relation (4.1). (a) Shows data on a junction with an area of (1.5 × 1.5) μm^2 and (b) with an area of (0.6 × 0.6) μm^2, respectively.

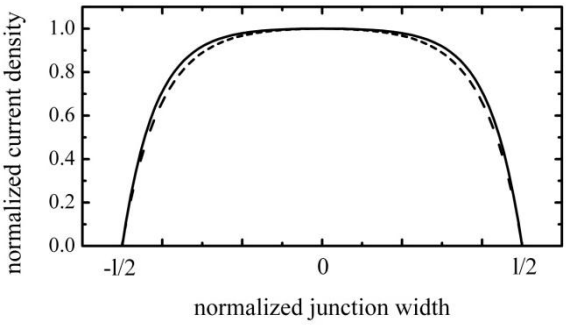

Figure 4.7: Current density profile along the junction width according to a model described by relation (4.3), with parameter $\kappa_{1.5\mu m} = 1.23 \pm 0.08$ and $\kappa_{0.6\mu m} = 1.06 \pm 0.06$, obtained from a fit as described in the text. Solid and dashed lines represent the junction area of $(1.5 \times 1.5)\ \mu m^2$ and of $(0.6 \times 0.6)\ \mu m^2$, respectively.

according to this relation with parameters κ as obtained above. One can see that the reduction of the current density at the junction edges increases slightly with decreasing junction size, which is most likely caused by the anodization of the junction's sidewalls or by small damages due to the reactive ion etch process for patterning the trilayer strip.
Nevertheless, even for the smallest fabricated junctions with an area of $(0.6 \times 0.6)\ \mu m^2$ a large nearly homogeneous region exists around the center of the junction. In conclusion, these measurements of the magnetic field dependences of the maximum critical current of the Josephson junctions do not imply a technological limitation for this junction dimensions and the cross-type technology can probably be extended to even smaller junction sizes, which are not only a major issue for further SQUID development but may also enhance the performance of future superconducting electronic devices.

4.3 Junction capacitance – Fiske steps

The junction capacitance was determined by the evaluation of Fiske steps in rectangular shaped Josephson junctions. These steps, as first described in [119, 120], occur at voltages V_F, where the frequency of the oscillating Josephson current corresponds to the geometric resonance frequencies of the electromagnetic cavity modes, given by the physical dimensions of the junction. In the particular case of vanishing maximum Josephson current density at specific external magnetic field amplitudes, the spatial distribution of the Josephson current density matches a standing wave, resulting in a constant voltage for a certain current interval.
Therefore, a measurement configuration as depicted in Figure 4.5 was used, where an external coil induces a magnetic field in plane of the junction's tunnel barrier and aligned along to the longer linear dimension of the junction. Both, coil and the junction are located inside a µ-metal can immersed in liquid helium at 4.2 K.
In particular, junctions with a width of 3 to 10 µm and a length ranging from 20 to 50 µm have been measured. Figure 4.8 shows a scanning electron microscope image of a $(3 \times 50)\ \mu m^2$ junction. Representative current-voltage characteristics of a $(3 \times 20)\ \mu m^2$

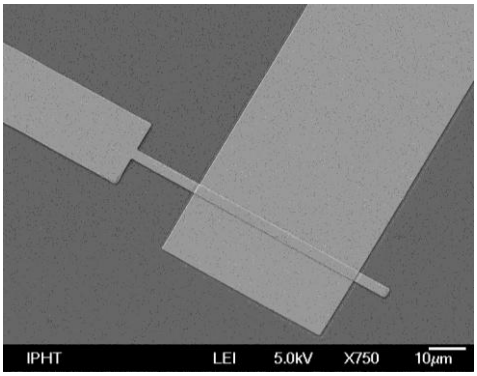

Figure 4.8: Scanning electron microscope image of a (3 × 50) µm^2 Josephson junction.

Josephson junction (a) and of a (3 × 50) µm^2 (b) Josephson junction are depicted in Figure 4.9, showing all measured Fiske steps due to a superposition of many *I-V* characteristics for sweeping of the external magnetic field.

It should be noted, that the junctions are of comparable good quality as the square junctions described in Table 4.1, except a slightly lower value for the ratio of the subgap to the normal resistance R_S/R_N of approximately 25.

According to [121] the step voltage can be described by

$$V_F^2 = \left(\frac{c_0\Phi_0}{2a_0}\right)^2 \cdot \left(\frac{t_{ox}}{\varepsilon_r}\right) \cdot \left(\frac{1}{t_{ox}+2\lambda_{L,Nb}}\right) \cong \left(\frac{c_0\Phi_0}{2a_0}\right)^2 \cdot \left(\frac{t_{ox}}{\varepsilon_r}\right) \cdot \left(\frac{1}{2\lambda_{L,Nb}}\right), \qquad (4.4)$$

with c_0 being the light velocity in vacuum, a_0 the width of the tunnel junction, ε_r being the relative permittivity of the barrier, and t_{ox} the thickness of the tunnel oxide barrier in the Josephson junction.

Under the assumption of a parallel plate configuration the specific junction capacitance c_S can be calculated as

$$c_S = \frac{C_{JJ}}{A_{JJ}} = \left(\frac{\varepsilon_r}{t_{ox}}\right) \cdot \varepsilon_0 = \left(\frac{c_0\Phi_0}{2a_0 \cdot V_F}\right)^2 \cdot \left(\frac{1}{2\lambda_{L,Nb}}\right) \cdot \varepsilon_0 \qquad (4.5)$$

with C_{JJ} as the junction capacitance, A_{JJ} the junction area and ε_0 as the vacuum permittivity.

For the calculation of the specific junction capacitance the open squares in Figure 4.9 were used. For junctions with a width of 3 to 10 µm and a length ranging from 20 to 50 µm values for c_S between 61.9 and 62.9 fF/µm^2 have been obtained, as listed in Table 4.2 for two different wafers. As this value shows a very weak dependence on the critical current density, for subsequent discussions a mean value of about 62.5 fF/µm^2 will be used as the specific capacitance of the Josephson junctions with a critical current density of about 1.7 kA/cm^2. According to [122] a 10% change in the critical current density would change the specific junction capacitance to just about 1%.

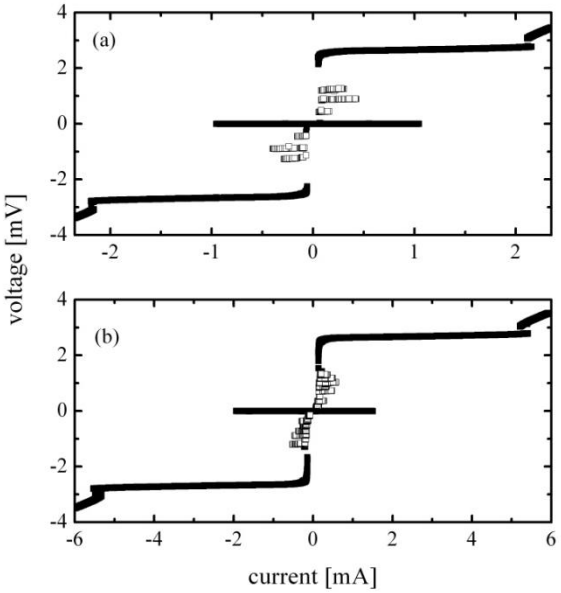

Figure 4.9: Current-voltage characteristics of a (3 × 20) μm^2 Josephson junction (a) and of a (3 × 50) μm^2 Josephson junction (b) with alternating external magnetic field.

Finally, the measured values show reasonable good agreement with the literature [122, 123]. Deviations may results from the use of different methods for the determination of the specific junction capacitance. For example, the evaluation of the specific junction capacitance by the measurement of the Josephson plasma resonance frequency from current-voltage characteristics [124, 125] seems to give somewhat lower values as reported in [122].

Therefore the total capacitance of the smallest fabricated junctions of (0.6 × 0.6) μm^2 amounts to about 20 fF. Compared to the conventional window-type junction technology, for which a total junction capacitance of about 690 fF was estimated in [79], this represents a reduction in the total junction capacitance to a factor of up to 34 and may still be enhanced with improved lithography tools.

As a conclusion, cross-type Josephson tunnel junctions with sub-micrometer dimensions do not only show excellent electrical characteristics, but also provide a very low total junction capacitance, which is achieved by downsizing the junction area as well as by avoiding any unnecessary overlap of the junction electrodes resulting in parasitic

Table 4.2: Measured specific junction capacitance for two wafers.

junction size (μm^2)	Wafer 1983	Wafer1991
(3 × 20) μm^2	62.4 fF/μm^2	62.9 fF/μm^2
(3 × 50) μm^2	61.9 fF/μm^2	62.8 fF/μm^2
(10 × 50) μm^2	-	62.7 fF/μm^2

capacitances in parallel to the junction capacitance. They are therefore well suited for superconducting electronic devices that benefit from a low total capacitance, like e.g. very low-noise and high-performance SQUIDs.

5 SQUID Characterization

In the prior chapters fundamental relations describing the performance of SQUID magnetometers were given, leading to a prescription towards low-capacitance Josephson junctions. The presented cross-type technology was then evaluated in respect to the fabrication of high-quality Josephson junctions via their electrical characteristics as well as by measurements of the magnetic field dependence of the maximum critical current. In addition, measurements of Fiske steps result in a total junction capacitance as low as 20 fF for junction sizes of $(0.6 \times 0.6)\ \mu m^2$.
Therefore, within this chapter I will estimate achievable improvements on SQUIDs due to the reduced junction capacitance, which will be compared with experimental results on SQUID magnetometers developed for the use in a geophysical receiver system for transient electromagnetics in Chapter 5.3. Additionally, results on the field stability of these sensors will be shown and discussed for cool-down in magnetic background fields as well as the behavior in changing applied magnetic fields in the mT-range during operation. In Chapter 5.6 a detailed characterization of a magnetometer family fabricated within this technology, developed for various application-scenarios, will be given. Finally, in Chapter 5.7 I will discuss the low-frequency noise behavior of these sensors indicating a clear dependence of low-frequency magnetic flux noise on the device effective areas, similar to a model of fluctuating surface spins as e.g. given in [76].

5.1 Estimation of improvements on SQUIDs due to low capacitance cross-type junctions

As described in Chapter 3.1, in the commonly used window-type technology the total junction capacitance consists of a capacitance $C_{JJ,0}$ given by the barrier thickness and the dimension of the junction area and a parasitic capacitance $C_{JJ,p}$ due to the idle region, the undesired overlap between wiring layers forming a capacitance in parallel to the junction capacitance. For this process the total junction capacitance C_{JJ} was estimated to about 690 fF for a junction size of $(3.2 \times 3.2)\ \mu m^2$ e.g. in [79].
Within the cross-type technology, the junction capacitance is reduced by downsizing the junction area into the sub-micrometer range as well as by avoiding any idle regions. Therefore, according to results of Fiske step measurements in Chapter 4.3 the minimum junction capacitance in the cross-type technology amounts to about 20 fF.
I will now consider the improvements on SQUID performance due to the reduced junction capacitance: According to relation (2.12) the figure of merit for a magnetometer

– the equivalent[2] magnetic field noise spectral density S_B of the SQUID – can be expressed as

$$\sqrt{S_B} = \frac{\sqrt{S_\Phi}}{A_{eff}} = \frac{4L_{SQ}^{3/4}C_{JJ}^{1/4} \cdot \sqrt{2k_B T}}{A_{eff}}, \tag{5.1}$$

with $A_{eff} = \partial\Phi/\partial B$ being the effective area of the magnetometer.
According to relation (2.13) the transfer-function V_Φ and thus the usable voltage swing δV scales as $V_\Phi \propto \delta V \propto C_{JJ}^{-1/2}$.

Accordingly for (0.6 × 0.6) μm^2 Josephson junctions with capacitance of about 20 fF, one can estimate that the intrinsic flux noise reduces by a factor of approximately 2.4 compared to [79]. The transfer function and voltage swing are increased as well by a factor of about 5.9, therefore simplifying the read-out of these sensors. The corresponding energy resolution of e.g. a SQUID with an inductance L_{SQ} = 100 pH would therefore be as low as 2 h at 4.2 K using relation (2.11).

A detailed discussion on the achievable sensitivities will be given in the next chapters together with a comparison to real fabricated devices.

5.2 Design considerations on SQUID magnetometer for TEM

In [126] the four possible layout-types for coupling of an external signal to a SQUID have been discussed. These are namely the galvanometer-SQUID, the washer or flux-concentrator-SQUID, the multiloop-SQUID, and the flux-transformer or Ketchen-type SQUID. Although the discussion referred to SQUID gradiometer, the basic dependencies also remain valid for SQUID magnetometer.
As pointed out, the ratio of the SQUID-inductance to the effective area is much larger for the first two compared to the latter two types. According to relation (5.1) for a given effective area of the magnetometer the SQUID-inductance and accordingly the field noise spectral density would be much larger for the galvanometer- and washer-type SQUID. Therefore, both of these concepts will not be considered here.
The latter two types differ in the fact that in the multiloop-magnetometer the SQUID itself acts as the sensitive area, whereas the Ketchen-type SQUID is inductively coupled to an antenna. As the theoretical limit of ideal coupling without losses will per se not be achieved in reality, the multiloop-magnetometer layout is to be favored regarding a lower field noise for equal SQUID inductances.

In an advanced system a multiloop-magnetometer may be used as a first stage SQUID in combination with a second-stage SQUID amplifier like a SQUID-array of SQIF. The

[2] It is called equivalent magnetic field noise spectral density since it is calculated from the equivalent flux noise spectral density S_Φ which is derived from the measured voltage noise spectral density S_V.

advantage of such a system, like the adjustable flux gain between these two stages allows neglecting the contribution of the room-temperature electronics to the overall system noise. However, an increased flux gain results in a reduced linear flux range and therefore in a lower slew-rate of the system [71] which forces to a compromise between low noise on one hand side and a high slew-rate of the measurement system on the other side.
Moreover, the need for additional wires between room-temperature and the cryogenic region to control the additional amplifier SQUID raise the thermal load on the liquid helium bath, limiting the operation-time, an essential aspect for a measurement system in the field. A larger number of wires in addition potentially lower the system stability against high-frequency disturbances.
The intended purpose of the developed system for magnetically unshielded field operation in various conditions and even by non-profession personal requires very reliable and robust systems. Therefore, the operator's convenience as well as the attempt to minimize incidences of fault operation put additional constraints with respect to a fully automated setup of the working points and the complexity of the electronics, which are much easier to meet in single-stage configurations.

The direct use of series SQUID arrays as a current sensor to read out the flux induced screening current in a pickup loop is not feasible, as inevitable inaccuracies in the lithography and hence small variations in SQUID geometries lead to amplitude modulation of the flux-voltage characteristics for large flux bias values [71]. Trapped flux in the individual SQUIDs of the array may cause distortions in the flux-voltage characteristics in typical state of the art series SQUID arrays too if they need to be operated not only in Earth's magnetic field but even in additional applied magnetic fields like in TEM.
More sophisticated concepts like the (double) relaxation oscillation SQUID [127, 128] may be able to combine a low sensor noise and a high slew rate, if an on-chip feedback scheme is implemented [129]. However, like their digital SQUID counterparts based on single flux quantum technique [130] they put great demand on the fabrication technology, which contradicts the request of high reliability and reproducibility of the developed sensors within this thesis. Moreover the correct operation of RSFQ circuits is limited by their influence on external magnetic fields currently to a working range of -2 µT to +7 µT [130].
The recently experimentally demonstrated combinations of a current-sensor SQUID and a SQUID-array [131] or a SQUID magnetometer together with a SQIF [36], both comprising local on-chip feedback schemes are very promising, even though up to now detailed information for instance of the influence of magnetic background fields on such advanced concepts are missing. More information on such SQIF-based dc SQUID amplifier with intrinsic negative feedback based on multiloop magnetometer developed within this thesis will be given in the Appendix.
Due to the above considerations, this thesis will focus on a single stage sensor concept based on a multiloop SQUID magnetometer, although such advanced concepts will most likely gain their importance in future.

In the multiloop magnetometer, as described in detail in [132-135], the superconducting pickup loop is divided into a number of separate loops connected in parallel to reduce the total SQUID inductance. This allows a lower SQUID inductance while maintaining a large effective area.

Based on the analytical expressions summarized in [135], a multiloop magnetometer suited for the use in a geophysical receiver system for transient electromagnetics was developed. The application scenario leads to the following constraints: For a desired field resolution of below 20 $fT/Hz^{1/2}$ in the white noise region of the spectrum and for a realistic value of the flux noise density of the SQUID of about $(2 – 10)\ \mu\Phi_0/Hz^{1/2}$, a magnetometer inverse effective area of $(2 – 10)\ nT/\Phi_0$ is necessary. A reasonable compromise for the inverse effective area of about 5 nT/Φ_0 has therefore been chosen.

According to recommendations given in [79] concerning the vortex entry into superconducting thin films during sensor movement in Earth's magnetic field, the maximum linewidth of all superconducting structures should be below 60 µm. Being more restrict, the linewidth of all superconducting structures was designed to be well below this value in order to increase the threshold for vortex entry, if there is no significant decrease in device performance.

The basic equations for the subsequent optimization of the multiloop SQUID magnetometer can in detail be found in [135]. Figure 5.1 shows the characteristic magnetometer layout and depicts main geometric parameters used for the calculations. In the optimization process I used the following specific parameters for the presented technology: $A_{JJ} = (0.8 \times 0.8)\ \mu m^2$, $I_C = 10\ \mu A$, $C_{JJ} = 40\ fF$, $R_{JJ} = 18\ \Omega$. It results in a moderate McCumber parameter β_C of about 0.4, which is close to the experimentally obtained values, as described in Chapter 5.3.

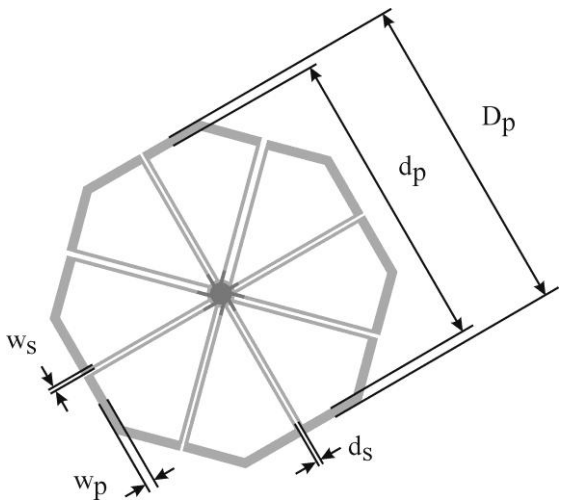

Figure 5.1: Layout of the multiloop magnetometer describing the characteristic parameter for the calculations. Therein D_p denotes the outer pickup coil dimension, $d_p = D_p\text{-}2w_p$ the inner pickup loop dimension, w_p the pickup loop width, w_s the spoke width, and d_s the width of the slits between the spokes.

As a first step the outer dimension of the pickup coil D_p has been varied. Figure 5.2 (a) shows the corresponding dependencies for the effective area on the number of parallel loops N for D_p ranging from 1.5 to 3 mm in steps of 0.5 mm. Here the following parameters have been used: linewidth of the pickup coil w_p = 60 µm, spoke linewidth w_s = 20 µm, and slit width between spokes d_s = 3 µm. For each value D_p for the pickup coil the corresponding number of parallel loops, which leads to the desired effective area of approximately 0.4 mm^2, is highlighted by an encircled dot. One can clearly see, the desired effective area can by realized with moderate number of parallel loops for all listed dimensions of the outer pickup coil.

In addition, the dependence of the SQUID inductance on D_p and N, which has two major contributions, is depicted in Figure 5.2 (b). One contribution is L_p/N^2 which is caused by the separation of the pickup loop inductance L_p into N parallel sections. The second is the term L_s/N and stems from the N parallel spoke inductances L_s. It is obvious that for a large number of parallel connected loops N the second contribution will have an important influence to the total SQUID inductance L_{SQ}. For the sensors in this work, a slit width of d_s = 3 µm is used which results from technological limitations and determines the stray flux into the slit and thus the inductance of the spokes. This contribution may be reduced by a change from coplanar spokes, as used in the sensors within this thesis, to stripline spokes. The stripline configuration is not used for the sensors within this thesis because the resulting parasitic capacitance may strongly influence the device performance. Table 5.1 lists the calculated values for the above derived parameters.

Especially the value L_{SQ}/A_{eff} shown in Figure 5.2 (c) is relevant for the sensor optimization since it describes the effectiveness of the transformation of a given SQUID inductance into an effective area. Both dependencies L_{SQ}/A_{eff} and the achievable magnetic field noise $B_n(f) = S_B^{1/2}(f)$ which is shown in Figure 5.2 (d), still decrease for a larger number of parallel loops N in the range up to 25. Another general tendency for the best achievable magnetic field resolution found in Figure 5.2 is towards larger D_p.

Further calculations with a variable linewidth of the pickup coil and spokes guide towards an increase in D_p and N for a decreased field noise too. However, according to the prior discussed restriction in the maximum linewidth of the superconducting structures w_p is limited to about 60 µm and an increase in the spoke width to values larger than 20 µm does not lead to a significant improvement in sensor noise. Therefore, linewidths exceeding these values are not realized in favor to a potentially improved stability towards magnetic background fields during operation.

There is another limitation which directly relates to the sensor performance – the input noise of the electronics which will be used in the instrument. At a defined dimension D_p of the pickup loop a high magnetic field resolution is achieved for large number N of parallel connected loops which leads to very low intrinsic voltage respectively flux noise of the sensors. These low noise levels are not directly measurable since they are typically lower than the electronics input noise.

For all the above discussed reasons a tradeoff has been done in this work. An outer pickup coil dimension of D_p = 2.0 mm was chosen.

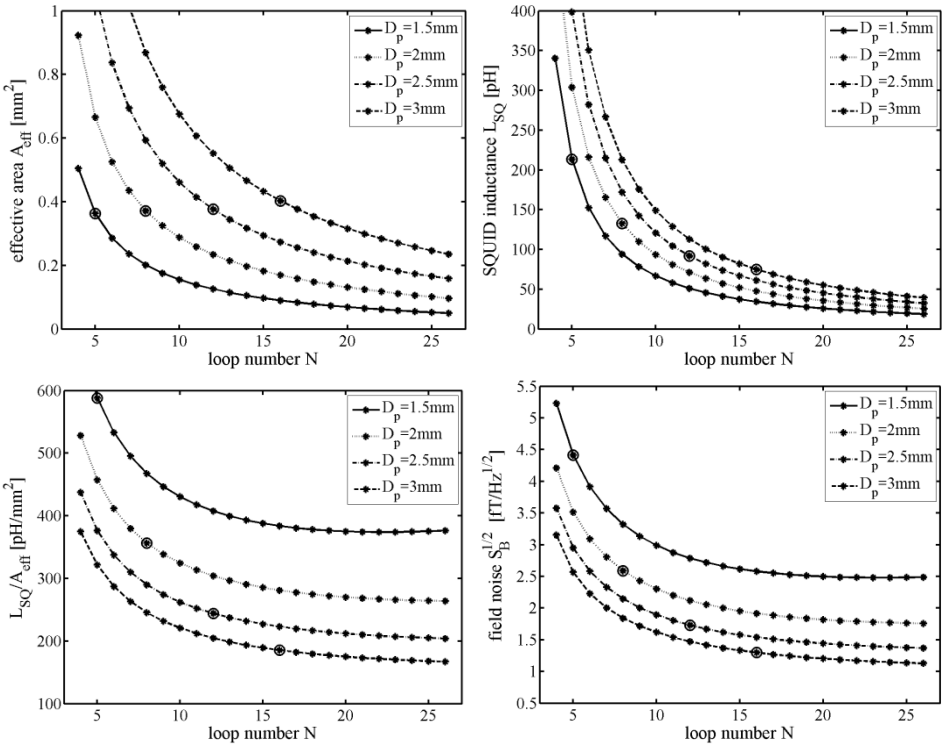

Figure 5.2: Results of calculation for multiloop SQUID magnetometer according to equations given in [135] and characteristic junction parameters as given in the text. (a) shows calculated effective areas A_{eff}, (b) the SQUID inductance L_{SQ}, (c) the ratio $L_{\mathrm{SQ}}/A_{\mathrm{eff}}$, and (d) the calculated magnetic field noise vs. the number N of parallel loops in the multiloop magnetometer.

Secondary reasons for this choice of D_{p} are on one hand that for multichannel systems a small chip sizes is favorable to enable a large number of sensors and to reduce cross talk between them. On the other hand the overall dimension could be reduced und thus a cryostat with small neck could be used which enables a longer hold and respectively operation time of the instrument. Since the dependence of the minimum magnetic field

Table 5.1: Calculated values for multiloop magnetometer based on cross-type Josephson tunnel junctions as shown as encircled data points in Figure 5.2. Note, that the flux and field noise represents the white noise levels.

D_p	N	A_{eff} [mm^2]	L_{SQ} [pH]	$S_B^{1/2}$ [fT/Hz$^{1/2}$]	$S_\Phi^{1/2}$ [$\mu\Phi_0$/Hz$^{1/2}$]	L_{SQ}/A_{eff} [pH/mm^2]
1.5 mm	5	0.363	213	4.2	0.73	588
2.0 mm	8	0.372	133	2.5	0.44	356
2.5 mm	12	0.376	92	1.6	0.30	244
3.0 mm	16	0.403	75	1.2	0.24	186

resolution from the number N of required parallel loops is rather weak according to Figure 5.2 (d), the number of loops was set to 8 in order to meet the required effective area of 0.4 mm^2.
In summary, for the use in a receiver system for transient electromagnetics a multiloop SQUID magnetometer with the following parameter will be used: $D_p = 2$ mm, $N = 8$, $w_p = 60$ µm, $w_s = 20$ µm, and $d_s = 3$ µm. This sensor layout will be denoted as ML2A within this thesis.

5.3 Results on SQUID magnetometer for TEM

The main goal of the development of SQUID based magnetometer, as already stated in the preface of this chapter, are sensors with increased voltage swing, improved energy resolution and an increased tolerance respect magnetic background fields compared to sensors based on Josephson junctions fabricated in conventional window type technology. This sub-chapter will focus on the aspect of SQUID sensors with increased voltage swing while the Chapter 5.4 and Chapter 5.5 will show results on the other aspects of the SQUID magnetometer intended for the use in transient electromagnetic receiver systems.
For the electrical characterization of the SQUID sensors the measurement setup as described in Chapter 4.1 has been used. Typical obtained current-voltage and flux-voltage characteristics for magnetometer of type ML2A with (0.8×0.8) µm^2 Josephson junctions are shown in Figure 5.3. The flux in the SQUID has been modulated by a current through an integrated feedback coil. The mutual inductance corresponds to about 5.1 µA/Φ_0.
Typical values of the fabricated SQUIDs are: $I_C \approx 9.5$ µA and $R_{Sh} = 20\ \Omega$. For moderate damping of the Josephson junctions with β_C about 0.4 the typical usable voltage swing amounts to $\delta V = 170$ µV, which is roughly about a factor of 3 larger than for SQUID magnetometer fabricated in the conventional window type technology with McCumber parameter β_C about 1.
In addition Figure 5.3 (left) shows the simulated current-voltage characteristics obtained with JSIM [46, 47] and junction parameter as listed above. One can see a reasonable good agreement with the measurements. The dip in the *I-V* characteristic at about 200 µV is due to the insufficient damping of the washer resonance. Moreover, one has to note that the resonance at 380 µV can be found in both measurements and simulations, leaving further room for improvement towards optimized McCumber parameter together with precise control of resonances within the sensor.
SQUID sensors with such a moderate damping of $\beta_C \approx 0.4$ will be deployed for the use in an instrument for TEM.

Based on the relations given in [135] one can estimate the intrinsic voltage noise of the magnetometer to be about 125 pV/Hz$^{1/2}$. Compared with the input voltage noise of the used low-noise SQUID electronic from Supracon [136], which amounts to 0.33 nV/Hz$^{1/2}$, one can clearly see, that the measured noise would be dominated by the SQUID electronics.

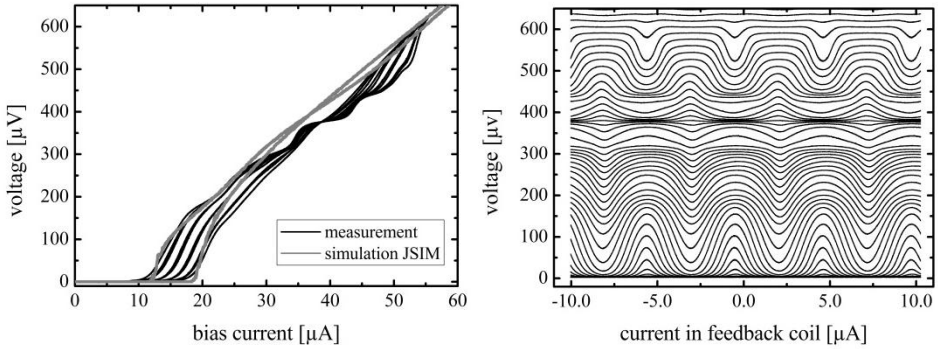

Figure 5.3: (left) Typical *I-V*-characteristic of multiloop magnetometer of type ML2A with (0.8 µm × 0.8) µm^2 Josephson junctions for Φ_{ext} ranging between $\Phi_{ext} = n\Phi_0$ and $\Phi_{ext} = n\Phi_0/2$ and corresponding set of flux-voltage characteristics (right) for bias currents ranging from 0 to 56 µA in steps of 1 µA.

In order to measure the intrinsic noise of the SQUID magnetometer another SQUID was used as a low-noise preamplifier as described in [137]. The schematic of such a two-stage setup can be seen in Figure 5.4. The used SQUID electronics allows the bias supply for two independent SQUIDs as well as to switch the feedback current to couple inductively either to the first or the second SQUID. Hereafter they will be denoted as detector and amplifier SQUID, respectively. Applying a feedback signal to the detector SQUID allows for the determination of the overall transfer function independent of the working point and subsequent noise measurements. The influence of different working points can easily and fast be acquired. This operation mode was used in most cases for the noise measurements within this thesis.

The operation mode with feedback signal applied to the amplifier SQUID gives the opportunity to investigate the noise even in reversal points with $\partial V/\partial \Phi = 0$. This

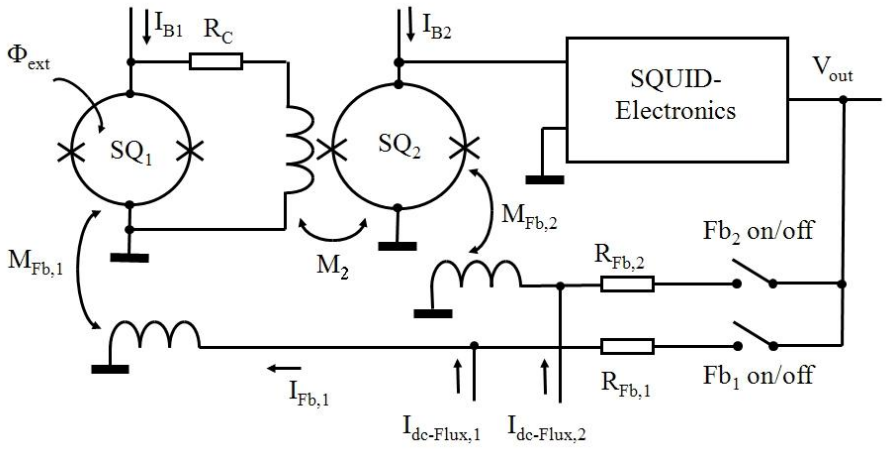

Figure 5.4: Schematic of measurement setup for two-stage noise measurements. Therein the flux noise of SQUID SQ_1 is measured with a second stage SQUID SQ_2 operated as a low noise preamplifier.

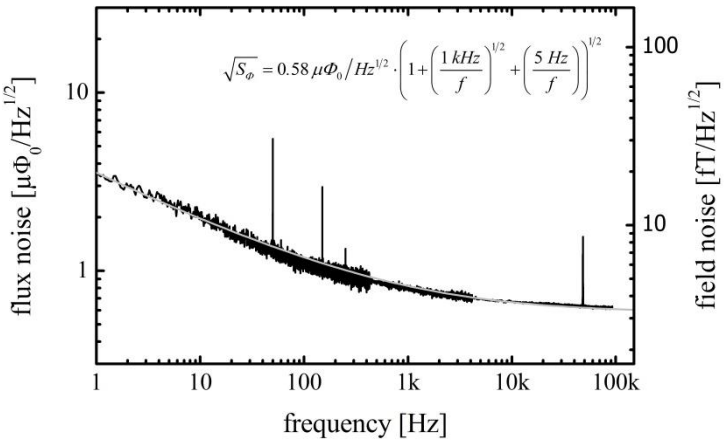

Figure 5.5: Typical noise spectra of a multiloop SQUID magnetometer of type ML2A with (0.8×0.8) µm^2 Josephson junctions and corresponding experimental fit shown as a grey solid line. Obviously, it starts to slowly increase below relative high frequencies of about 10 kHz, contrary to common expectations.

operation mode was solely used in Chapter 5.7 for the determination of the low-frequency noise, as described therein.

Both SQUIDs were immersed in liquid helium inside a lead and µ-metal shield for the noise measurements. The noise spectra were recorded using a PXI based data acquisition from National Instruments ® with 24 bit analogue to digital converters (ADC) on a PXI-4462 card [109] inside the laboratory. The maximum sampling frequency was 200 kHz, whereby noise spectra up to a frequency of 100 kHz can be obtained.

As an amplifier-SQUID a current sensor SQUID of type CCblue [136] was used. The coupling resistor was $R_C = 4\ \Omega$.

One typical example of the measured flux noise spectrum is shown in Figure 5.5. The flux noise was scaled to the magnetic field noise on the right hand side by using the measured effective area of the device of about 5.55 nT/Φ_0. For the measurement of the effective areas a Helmholtz coil system as described in [138] was used.

The measured frequency dependence of the noise can be described as $S_\Phi{}^{1/2} = 0.58\ \mu\Phi_0/\mathrm{Hz}^{1/2} \cdot [1+(1\ \mathrm{kHz}/f)^{1/2}+(5\ \mathrm{Hz}/f)]^{1/2}$ as represented in Figure 5.5 by the solid grey line. The white magnetic field noise amounts to about 3 fT/Hz$^{1/2}$. Although the SQUID magnetometer show very good results regarding the white noise level, the low-frequency noise dependence is quiet unusual. Below about 10 kHz the power spectral density of flux noise scales as $1/f^{1/2}$, with f being the frequency. Chapter 5.7 will focus on this low-frequency noise dependence.

Further, it is important to note, that the energy resolution of this SQUID with $L_{SQ} = 130$ pH amounts to about 7 h at 4.2 K in the white noise region.

In a single stage configuration the transfer function of the SQUID in the working point was measured. It amounts to about 650 µV/Φ_0. The inverse current sensitivity $\partial I_B/\partial \Phi$ of the SQUID was determined to 15 µA/Φ_0. Using these values to scale the SQUID electronics preamplifier voltage and current noise [136] into flux noise contributions of

0.51 $\mu\Phi_0/Hz^{1/2}$ and 0.43 $\mu\Phi_0/Hz^{1/2}$, it is obvious that it is not possible to measure the intrinsic noise due to the noise contribution of the SQUID electronics in a single stage setup.
Taking the input noise of the SQUID electronics in a single stage into account, the measured white noise amounts to 0.9 $\mu\Phi_0/Hz^{1/2}$ corresponding to 5 $fT/Hz^{1/2}$. This value represents the lower bound one can achieve in a single stage configuration with such SQUID electronics and may be sufficient for a number of applications, like e.g. in biomagnetism. In systems requiring a high dynamic range or slew rate contributions from other noise sources, like thermal noise from the feedback resistors, may become remarkable or even dominant. As will be discussed in more detail in Chapter 6 one therefore has to compromise between sensor sensitivity, slew rate and dynamic range.
Compared to reported values for similar magnetometers in the literature [135, 139] these SQUID magnetometers show about half the intrinsic field noise together with a much larger usable voltage swing. According to relation (2.15), the increased transfer function reduces the contribution of the input voltage noise of the SQUID electronics and enables the readout of nearly the intrinsic sensor noise in a single stage setup. This may decisively simplify multichannel systems as e.g. in biomagnetism, as the need for special readout schemes like additional positive feedback [140] would not significantly improve sensor resolution in this case.

5.4 Sensor properties during cool-down

Besides the described improvements of SQUID sensors with respect to the intrinsic noise and usable voltage swing by the use of low capacitance cross-type Josephson junctions, the intended purpose of unshielded operation imposes special requests for the robustness against magnetic background fields during cool-down as well as during operation. Flux trapping in or close to the Josephson junctions would reduce the junction's critical currents, leading to a degradation of sensor performance.
As briefly described in Chapter 2.3 small geometric dimensions of superconducting circuit structures at or nearby the junctions are usually favorable, as the critical field for vortex trapping scales as $B \propto \Phi_0/w^2$ with w being the width of the superconducting structures [72-75].
For the investigation of the dependence of trapped flux in the Josephson junctions on the linewidth of the superconductor and correspondingly on the linear dimension of the junction, multiloop SQUID magnetometer of type ML2A based on cross-type Josephson junctions with areas in the range between (1.5 × 1.5) μm^2 and (0.6 × 0.6) μm^2 have been produced.
A setup as schematically shown in Figure 5.6 was used for the measurement. The flux-voltage characteristic was recorded, while the SQUID was in operation with a constant bias of $\approx 2I_C$. A constant magnetic background field was applied normal to the chip surface by a superconducting magnet [115], a superconducting coil in persistent current mode. The SQUID chip was heated during the investigation well above the superconducting transition temperature and cools down in this background field. Flux

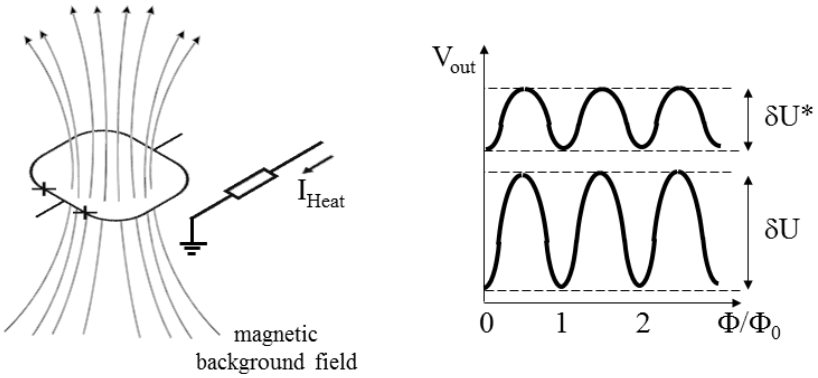

Figure 5.6: Schematics of measurement setup to investigate the dependence of flux-trapping in Josephson junctions on their linear dimension. The SQUID chip was cooled down in a static magnetic background field applied perpendicular to the chip surface. Flux trapping in the Josephson junctions is indicated by an altered flux-voltage characteristic.

trapping was then identified by a change of the junction's critical current and an altered voltage swing δU*.

This procedure has been performed at stepwise increasing background fields for each SQUID to be measured, obtaining a histogram-like characteristic for the flux-trapping probability, as shown in Figure 5.7 for a multiloop magnetometer with (1×1) μm^2 Josephson junctions. In this plot each data point represents the average of 30 measurements. The crossover-width from no flux trapping (open squares) to a 100% flux trapping probability (filled squares) is only ± 50 μT at a background field of about 2.7 mT for the (1×1) μm^2 Josephson junctions.

Figure 5.8 displays the measured magnetic background fields for a flux-trapping probability of 50 % in dependence of the linear dimension of the junctions. The open squares represent the investigation of SQUIDs based on cross-type junctions. The solid and dashed black lines indicate the dependencies given in [74] and [75], respectively.

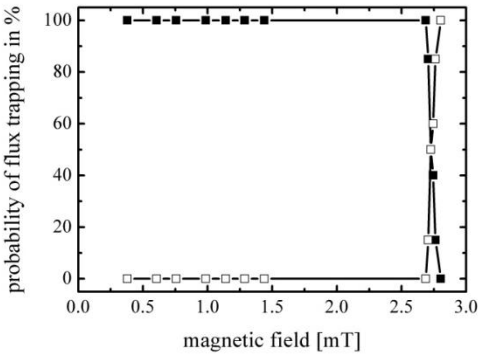

Figure 5.7: Flux-trapping probability for a multiloop SQUID magnetometer of type ML2A with (1×1) μm^2 Josephson junctions. Open squares represents no flux trapping whereas filled squares correspond to a flux trapping probability of 100%.

They both report a scaling law as $B = \alpha \cdot \Phi_0 / w^2$, with different pre-factors α indicating different stabilization criteria.

In addition, the filled squares in Figure 5.8 indicate values for the flux-trapping probability for larger window-type Josephson junctions, as given in [79]. It is important to note, that these points do not belong to the dimension of the junction window, which represents the junction area, but to the dimension of the base electrode, which needs to be larger than the junction area to rule out lithographic alignment errors between different layers. All junctions in this case had the same size of $(3.2 \times 3.2)\ \mu m^2$ and therefore the same critical current. One can see, that in both cases the measured data can be well described with the above expression.

It is obvious that downsizing the linear dimensions of the junctions as well as reducing or even avoiding any metallization close to the junctions lead to significant improvement in the stability against magnetic background fields during cool-down. In doing so, multiloop SQUID magnetometer of type ML2A with $(0.6 \times 0.6)\ \mu m^2$ withstand magnetic background field during cool-down of more than 6.5 mT [117]. This is about a factor of 100 better than in actual sensors, which typically withstand fields of up to (60–80) µT [139]. Moreover, due to the excellent scaling with theory one can expect further improvement by onward reducing the junction's dimension respectively the linewidth of the superconducting structures.

The critical magnetic background field for SQUID sensors with linear junction dimensions of 0.8 and 1.0 µm corresponds to 3.9 mT and 2.7 mT, respectively. This completely fulfills the requirements for the use in a geophysical receiver system for transient electromagnetics. Here it is important to note, that due to e.g. high magnetic overburden background fields as high as about 1 mT have been measured at the position of a ground based measurement system close to the soil surface.

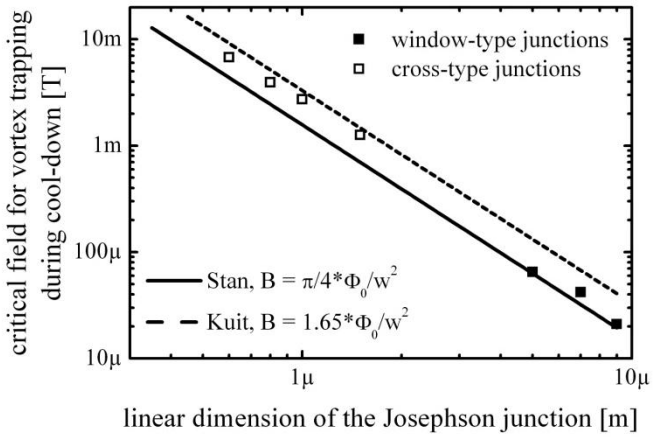

Figure 5.8: Critical field for vortex trapping in Josephson junctions in dependence of the linear dimension of the junctions. Open squares depict measured cross-type junctions, whereas filled squares depict data on window type junctions, as explained in the text. Solid and dashed lines represent theoretical dependencies given in [74, 75].

5.5 Behavior of SQUID magnetometer in applied magnetic fields

As transient electromagnetics is an active method the SQUIDs within a measurement system will experience applied magnetic fields. The magnitude of these signals depends e.g. on the actual transmitter loop configuration, the strength of the exciting primary field, and the position of the measurement system with respect to the transmitter loop. Thus, the amplitude of typical applied magnetic fields can amount up to mT at the position of the measurement system.

In addition to the stability against static magnetic background fields during cool-down, discussed in the previous chapter, I will here comment on the stability against an applied magnetic field for instance a polarizing field in NMR applications during sensor operation [141].

The same setup as described in Figure 5.6 was used for the measurements. The SQUIDs have been immersed in liquid helium inside a stainless steel screen. Instead of a static magnetic background field now magnetization "pulses" for the polarization field were used which were provided by the superconducting magnet. However, the magnet power supply limited the maximum rate of magnetic field change to about 0.91 mT/s. Because of this limitation the magnetization 'pulses' are sweeps in the background field with this maximum rate.

The same multiloop magnetometers of type ML2A, as described in the previous chapter, have been measured. They were operated in an open loop with constant bias of about $2I_C$. The SQUID voltage was recorded for a sweeping current through the integrated feedback coils on the SQUID chips. Magnetization pulses were applied either perpendicular to or in plane of the chip. Flux trapping within the Josephson junctions was again identified by a change in the junction's critical currents as well as in altered flux-voltage characteristics.

The measured dependence of the critical field for vortex trapping for a polarization field perpendicular to the chip plane respect the linear dimension of the junctions is shown in Figure 5.9 as open and filled squares. Two characteristic magnetic fields and accordingly two occurring effects have been observed.

The open squares represent a magnetic field B_1, for which the voltage-flux characteristic starts to lag behind the field change after the magnetization pulses. The observation is, that immediately after returning to zero magnetic field amplitude the voltage modulation is slightly decreased. During a certain time interval it increases to the voltage swing as before the pulse. This is presumably caused by creep of flux entering in the vicinity of the Josephson junctions and being expelled from this region later on.

The solid squares in Figure 5.9 represent a measured magnitude B_2 of the magnetization pulse, which leads to stable new working points of the SQUIDs, due to a change in the junction's critical current caused by frozen flux in or close to the Josephson junctions.

In addition one can see, that both characteristic magnetic fields can be described by a scaling law $B = \alpha \cdot \Phi_0 / w$, where α denotes a constant pre-factor, obtained from a fit to the measurement data.

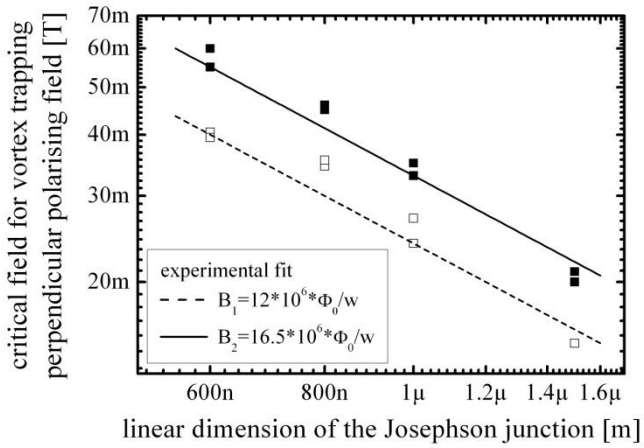

Figure 5.9: Critical field for vortex trapping for perpendicular polarization fields in dependence of the linear dimension of the junctions. Open and filled squares represent the data as described in the text; corresponding experimental linear fits are dashed and solid lines respectively.

For applications the magnitude of the polarization pulse B_1 indicates the maximum working range of the sensor if one needs to lock the FLL immediately after the magnetization pulse. By appropriate design changes this value could possibly be extended up to B_2, which seems to be the upper limit for the considered junction dimensions.

For the case of polarizing fields in plane of the chip, a critical magnitude of the polarizing field for vortex trapping of about 76 mT independent of the junction size was determined for most of the samples. However, some samples show even higher critical field amplitudes of up to several hundred milli-tesla. As these higher values vary from sample to sample, one may suspect that this effect is caused by slight technological variations so the pinning forces for the vortices may probably be lower and the trapped magnetic flux could be expelled from the superconducting film during ramp down. During the measurements these SQUID seem to withstand larger magnetization pulses before changing the junction's critical current.

In conclusion, downsizing the linear dimensions of the junctions does not only improve the sensor performance in respect to usable voltage swing, white flux noise and energy resolution, but the small junction dimensions lead to significant improvement in the stability against magnetic background fields during cool-down and operation.

Magnetization fields of up to about 40 mT for perpendicular polarization fields and about 76 mT for polarization fields in plane of the chip are to my knowledge the highest values for magnetization fields integrated SQUID sensors could withstand so far. This not only enables the use of these sensors in measurement systems for transient electromagnetics, but they even seem to be perfect candidates for combined MEG/ MRI systems [142, 143].

5.6 Complete ML Sensor family

In addition to the magnetometer of type ML2A, I will here present a complete family of magnetic field sensors. All SQUIDs were designed as multiloop SQUID magnetometers, as described in Chapter 5.2. They mainly differ in the outer pickup loop dimension and the number of loops, which results in different effective areas and SQUID inductances – depending on the particular application case [141].
Table 5.2 summarizes main parameters of the sensors. The number in the device names, which is an abbreviation for **M**ulti**L**oop magnetometer, indicates the outer pickup loop dimension of the SQUID. The same procedure as described in Chapter 5.2 was used for the optimization. Some layouts were chosen so to intentionally deviate from the optimization towards the lowest intrinsic sensor magnetic field noise in favor of their practical usability. The values in this table base on the equations in [135] using the measured junction parameter. The junction critical currents I_C, the damping resistance R_{Sh}, and the usable voltage swing were measured with the setup described in Chapter 4.1, whereof the McCumber parameter β_C and the screening parameter β_L were calculated according to equations (2.6) and (2.10). The noise was measured in a two stage configuration as described in Chapter 5.3. The measured energy resolution results from the measured white flux noise according to $\varepsilon = S_\Phi/2L_{SQ}$. A The effective areas were again determined using a Helmholtz coil system [138].
Table 5.2 lists information on five different planar-type magnetometer versions. There are two versions with an outer loop dimension of 2 mm, fabricated on a (2.5×2.5) mm^2 chip. In parallel to the prior discussed version ML2A, a version ML2B with four parallel loops and about twice the effective area was developed. It is to be favored in very compact single-stage setups where one would like to exploit the sensor noise performance with room-temperature electronics and were other restrictions, like e.g. the dynamic range do not impede this choice.
In order to reduce possible degradation of the energy resolution with increasing screening parameter $\beta_L > 1$ a damping resistance $R_D \approx R_{Sh}$ in parallel to the SQUID inductance, as described in [144], is introduced in all these devices. This enables fabrication of all these devices with effective screening parameters $\beta_{L,eff} \approx 1$ [135] on the same wafer, although value for SQUID inductance varies by a factor of about 3.

Typical flux-voltage characteristics for SQUIDs of type ML5 and ML12 are shown in Figure 5.11. These well damped dc-SQUIDs with McCumber parameters of $\beta_C \approx 0.4$ already show usable voltage swings of more than 100 µV. Smooth flux-voltage characteristics have been obtained in almost all cases with this moderate damping. Nevertheless, increasing towards optimized McCumber parameters leave further room for improvements, as already described in Chapter 5.3.
An asymmetry in the flux-voltage characteristic of the sensor ML12 is observable in Figure 5.11 because of the asymmetry of the SQUID inductance regarding the point for bias injection. This leads to a horizontal shift of flux-voltage characteristics at various bias currents and would diminish the influence of preamplifier current noise due to a reduced current sensitivity $|M_{dyn}| = |\partial\Phi/\partial I_B|$ on the left slope of the flux-voltage

Table 5.2: Characteristic parameters for a set of multiloop SQUID magnetometer based on low capacitance cross-type Josephson tunnel junctions measured at 4.2 K.

Device name	ML2A	ML2B	ML4.5	ML7	ML12
Number of loops, N	8	4	8	10	12
Chip size (mm × mm)	2.5 × 2.5	2.5 × 2.5	5.0 × 5.0	7.5 × 7.5	12.5 × 12.5
Outer pickup loop dimension D_p (mm)	2.0	2.0	4.5	7.0	12.2
Transfer function, $1/A_{eff}$, (nT/Φ_0)					
measured	5.55	3.03	1.09	0.57	0.25
calculated	5.54	2.48	1.10	0.56	0.26
Junction size, A_{JJ}, (µm × µm)	0.8 × 0.8	0.8 × 0.8	0.8 × 0.8	0.8 × 0.8	0.6 × 0.6
Junction critical current, I_C, (µA)	9.3	11.9	8.0	7.5	2.3
Shunt resistance, R_{Sh}, (Ω)	19.8	16.0	19.8	18.6	47.8
Calculated SQUID inductance, L_{SQ}, (pH)	130	375	270	325	300
β_L	1.19	4.30	2.10	2.34	0.67
β_C	0.44	0.37	0.38	0.31	0.36
Voltage swing (μV_{pp})					
measured	170	145	135	110	100
calculated	175	150	135	115	110
SQUID noise					
Intrinsic flux noise ($\mu\Phi_0/Hz^{1/2}$)					
measured	0.55	1.50	0.92	1.23	1.34
calculated	0.42	1.21	0.82	1.00	0.75
Measured intrinsic field noise ($fT/Hz^{1/2}$)	3.5	4.5	1.0	0.7	0.33
Energy resolution (h)					
measured	7.0	19.5	9.5	15.1	19.3
calculated	4.4	12.7	8.0	10.0	5.8

characteristic in the figure.

Figure 5.10 shows typical noise spectra for these two magnetometer versions. The SQUIDs were immersed in liquid helium inside a lead and µ-metal shield during these measurements. The time series of the FLL output signal was again recorded with the PXI based instrument described earlier. The corresponding noise spectra were calculated via a fast Fourier transformation (FFT).

The white magnetic field noise level of the devices indicated by the dashed line amounts to about 1 $fT/Hz^{1/2}$ for magnetometer of type ML5 with $(0.8 \times 0.8)\ \mu m^2$ Josephson

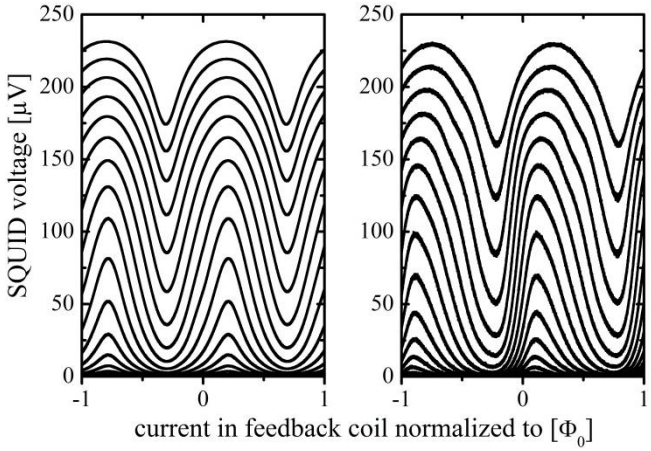

Figure 5.11: Typical set of flux-voltage characteristics of multiloop magnetometers of type ML5 (left) with $(0.8 \times 0.8)\ \mu m^2$ and ML12 (right) with $(0.6 \times 0.6)\ \mu m^2$ Josephson junctions, respectively.

junctions and to about 0.35 fT/Hz$^{1/2}$ for magnetometer of type ML12 with $(0.6 \times 0.6)\ \mu m^2$ Josephson junctions, respectively. This is roughly about a factor of two lower than white noise values of comparable integrated planar multiloop magnetometer reported in the literature [139]. This sensitivity seems adequate even for very demanding applications, like e.g. in AFMAG [145], where the EM responses to natural polarization fields are measured.

Although the presented SQUID magnetometers show very good results regarding their white noise level, they show rather unusual low-frequency noise dependences. In the next chapter this question will be discussed in more detail.

In summary from these measurements and the data listed in Table 5.2, there is reasonable good agreement between measured and calculated characteristics for the fabricated SQUID magnetometer based on cross-type Josephson junctions with linear dimension in the sub-micrometer range. The excellent sensor performance not only enables the use in geophysical receiver systems for transient electromagnetics, but even the implementation

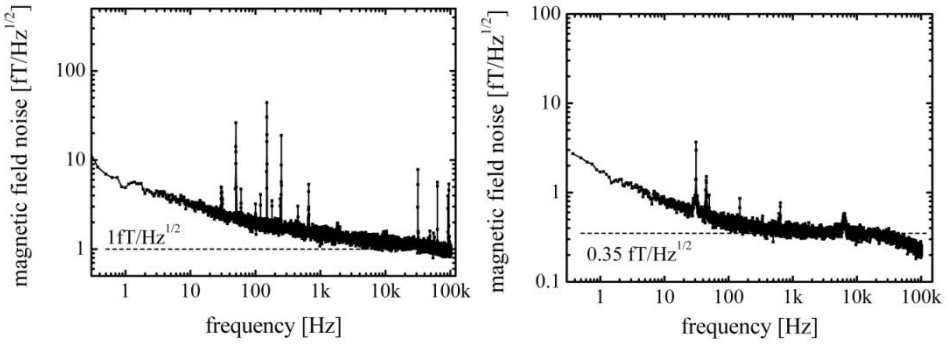

Figure 5.10: Typical noise spectra of multiloop SQUID magnetometer of type ML5 (left) with $(0.8 \times 0.8)\ \mu m^2$ Josephson junctions and of type ML12 (right) with $(0.6 \times 0.6)\ \mu m^2$ Josephson junctions.

of different SQUID magnetometer versions into a so called *Multipurpose SQUID receiver system* which will be discussed subsequently in Chapter 6.
It is worth to notice here, that the energy resolution in the white noise region of these magnetometers is typically of the order of $\varepsilon \approx 10$ h and according to Table 5.2 reaches values as low as about 7 h for type ML2A. This is up to about a factor of 4 lower than values reported in the literature for comparable sensors, as e.g. given in [146] and do correspond to expectations as ε scales with $\varepsilon \propto S_\Phi \propto C_{JJ}^{1/2}$.
One may therefore expect similar sensitivity improvement due to the use of low capacitance cross-type Josephson junctions in other SQUID types, as e.g. in SQUID current sensors, which will be discussed in more detail in the Appendix.

5.7 Low-frequency noise of the sensors

In the noise spectra shown earlier, rather unusual low-frequency noise dependencies are observed together with very low white noise levels for the fabricated SQUID magnetometer. The power spectral density of flux noise scales below about (1-10) kHz with $1/f^{1/2}$, with frequency f. For frequencies below about 1 Hz in the flux noise spectra e.g. in Figure 5.10 one may suppose an increase of the slope α of the low-frequency $1/f^{\alpha}$ scaling of flux noise.
To clarify the scaling of low-frequency noise as well as to distinguish between the individual low-frequency noise sources, the Allan variance [147] was calculated from the recorded time series of a two-stage noise measurement for a magnetometer of type ML2A. The Allan variance is a statistical measure which is typically used to determine the stability of oscillators, clocks, and amplifiers. It is well suited to analyze especially slow noise processes within these systems.
Figure 5.12 shows the flux noise spectra calculated from the recorded time series of measured output voltage of the SQUID as well as the corresponding Allan standard deviation vs. the cluster time τ, which can be seen as the inverse frequency in the FFT. In addition, calculated Allan standard deviations for synthetic signals containing white noise, $1/f^{1/4}$ and $1/f^{1/2}$ flux noise, and random walk are plotted. The magnitudes of the individual noise sources have been adjusted to fit to the measured curve. According to [147] the different slopes in Figure 5.12 (bottom) indicate the individual noise processes.
One can now clearly identify and separate the different branches of the scaling law of flux noise with frequency. For $\tau < 1 \cdot 10^{-3}$ s (corresponding to $f > 1$ kHz in the associated FFT) the SQUID exhibits white flux noise. In the range between $1 \cdot 10^{-3}$ s $< \tau \leq 5$ s the flux noise scales as $1/f^{1/4}$. For 5 s $\leq \tau \leq 50$ s the magnetic flux noise $S_\Phi^{1/2}$ has a dependence of $1/f^{1/2}$. Above $\tau \approx 100$ s the system shows a random walk characteristic, which is probably due to thermal drift in the SQUID electronics. The bump at $\tau \approx 0.01$ s corresponds to the measured power line interferences.
These results give reason to assume two – probably independent – low-frequency noise sources in the measured SQUID.

Extrapolating the observed $1/f^{1/2}$ dependence of flux noise in the frequency range $20\,\mathrm{mHz} \le f \le 0.2\,\mathrm{Hz}$ to about 1 Hz yields a magnitude of flux noise of about $1.5\,\mu\Phi_0/\mathrm{Hz}^{1/2}$ at this frequency. Although it is not yet established, if the flux noise dependence for $f < 0.2$ Hz is due to critical current fluctuations in the Josephson junctions, this is very likely, as recent experiments [148] have determined the magnitude of critical current fluctuations to

$$\frac{S_{I0}}{I_C^2} \approx \frac{1}{A_{JJ}/\mu\mathrm{m}^2} \cdot \left(\frac{T}{1\,\mathrm{K}}\right) \cdot \frac{1}{f} \cdot 10^{-13}\,\mathrm{Hz}^{-1}. \tag{5.2}$$

For Josephson junctions with a critical current of 10 µA for a junction area of $A_{JJ} = 0.64\ \mu\mathrm{m}^2$ in conjunction with a current sensitivity $M_{dyn} \approx 2 \cdot L_{SQ} \approx 260$ pH this results in about $1\ \mu\Phi_0/\mathrm{Hz}^{1/2}$ which is close to the above extrapolated value.

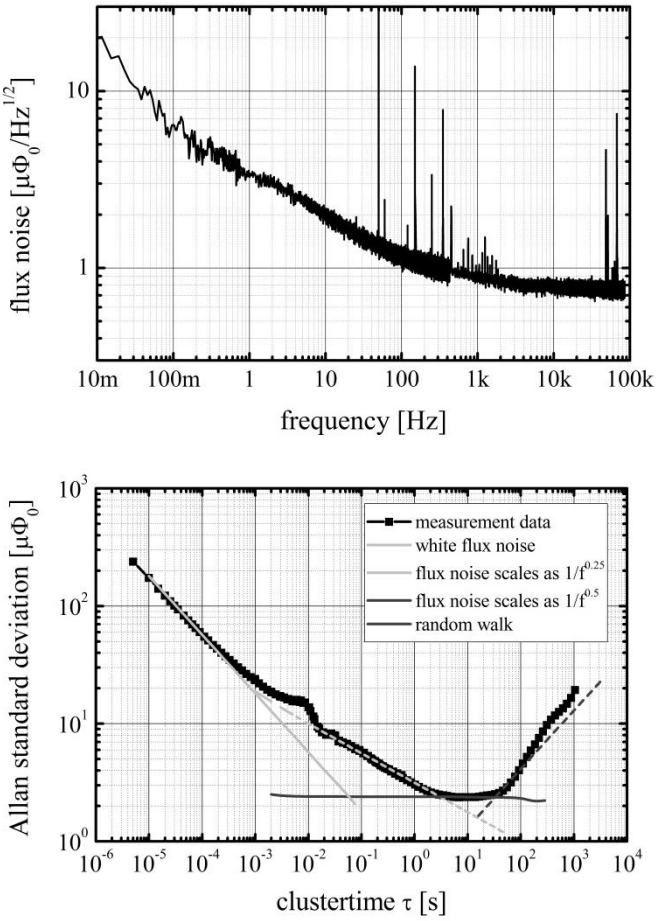

Figure 5.12: Top: Flux noise of magnetometer of type ML2A. Bottom: Allan standard deviation calculated from the same time series as the above FFT and corresponding calculated dependencies for white, $1/f^{1/4}$, $1/f^{1/2}$ flux noise and random walk in the measurement system, as described in the text.

As the frequency of interest for the intended application is about 1 Hz to several kHz, I will mainly restrict the following discussion to this range. As discussed earlier, in this case two major low-frequency noise sources have to be distinguished in the investigation of the origin of the low-frequency noise: the critical current fluctuations in Josephson junctions and real flux noise having magnetic nature, e.g. due to movement of trapped vortices [66].

To rule out the first source, low-frequency noise measurements with an ac-biased flux-modulated SQUID electronics [149] have been performed in the frequency range $f \geq 1$ Hz in addition to the prior described noise measurements with a direct coupled SQUID electronics [136]. As in detail described in [141] the noise of a SQUID magnetometer of type ML2A has been measured open loop at different working points *W*, as depicted in the inset of Figure 5.13. The measured voltage noise of the SQUID immersed in liquid helium inside a superconducting and μ-metal shield is shown in Figure 5.13.

For the working point W_1 in Figure 5.13 with a nonzero transfer function an increase in the low-frequency voltage noise proportional to $1/f^{1/4}$ (dashed line) has been observed, whereas in W_2 – where the sensor is insensitive to magnetic signals – the measured noise remains white in the whole frequency range. In conclusion, the increase in this frequency range is mainly caused by a magnetic signal and not by critical current fluctuations in the Josephson junctions.

In addition, fluctuations of the external magnetic field e.g. due to environmental noise inside the laboratory can be ruled out, as this noise source would scale with the effective areas of the magnetometer. As no scaling of the low-frequency magnetic field noise with the device effective areas has been observed in these measurements one can conclude that the source of this noise has to be local – within the dimension of the effective area.

For the investigation of magnetic noise caused by the motion of vortices trapped in the SQUID structure, a magnetometer similar to type ML2A was fabricated, where all superconducting parts were slotted with a maximum superconducting linewidth of 5 μm,

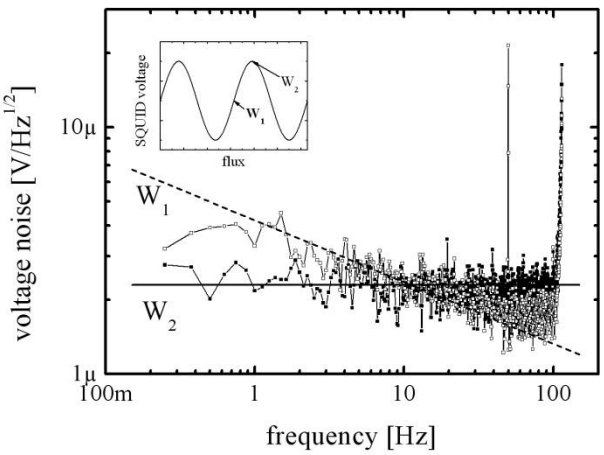

Figure 5.13: Low-frequency noise of a multiloop magnetometer of type ML2A at different working points (as shown in the inset in the flux-voltage characteristic), measured at 4.2 K inside a superconducting shielding and μ-metal shield. Note, that the decrease below about 1 Hz in working point W_1 is due to the ac-coupling of the input of the used spectrum analyzer.

similar to [150]. The inverse effective area of this device didn't change significantly due to the slots and a value of 5.15 nT/Φ_0 was determined compared to 5.55 nT/Φ_0 for the magnetometer with solid washers. As no difference regarding the low-frequency noise between the slotted version and the magnetometer ML2A with solid structures was observed, one can rule out the motion of trapped flux as a source of 1/*f* noise in these devices.
Contaminations during device fabrication, which are, however, very unlikely, do not seem to contribute to the measured noise, as e.g. SQUID magnetometer from a fabrication run in another, recently installed sputter system with a different Nb target in addition with a much better base pressure in the sputter chamber lead to the same results. It is worth to mention, that Josephson junctions within this new fabrication system show the same excellent quality with e.g. R_S/R_N values of about 40 for (0.8×0.8) µm^2 Josephson junctions with a critical current density of 1.7 kA/cm^2. This again indicates the robustness and reliability of the developed junction fabrication process.
None of the changes of the noise measurement setup had any influence on the measured magnetic noise level. Neither strong filters of electrical connection lines of the SQUID electronic nor the change of mutual inductance for the feedback lead to a change in the measured noise. Even the influence of other hypothetical noise sources like the typically used SQUID support material FR4 are very unlikely, as a change to e.g. hard paper didn't show any measurable effect within this frequency range.

It is important to note, that the observation of this noise for the multiloop magnetometer in this work is consistent with results as e.g. given in [66, 151, 152]. Accordingly, the remaining observed magnitude of low-frequency flux noise has been attributed to some unknown origin and has been a puzzle for about the last 30 years. At 4.2 K typical reported values for the magnitude of flux noise $S_\Phi^{1/2}$ at 1 Hz range between $(1 - 10)$ µΦ_0/Hz$^{1/2}$ and only a slow scaling with SQUID dimensions have been reported yet.
It has been shown recently, that low-frequency flux noise of the same kind and magnitude – and therefore probably originating from the same local noise sources – leads to dephasing in flux [153, 154] and phase qubits [155, 156]. According to recent investigations in qubits [76, 156-161], it is currently believed, that this low-frequency flux noise originates from single electron spins located on the surface of the superconductor. For example in the model in [76], the noise is generated by spins of unpaired electrons hopping on and off defect states due to thermal activation. In this case, the direction of the spins would be locked as long as the electrons are trapped, thus contributing magnetic signal. The superposition of many uncorrelated changes of spin direction would sum up to the observed 1/*f* power spectrum [67]. In [156, 158, 160] a scaling of the flux noise spectral density as *d*/*w* was proposed, with *d* being the inner pickup loop dimension of the SQUID and *w* the loop width. Unfortunately, most investigations reported in the literature up to now were limited to square washer-type SQUIDs and target on rather small loop dimensions in the µm range or do not systematically vary device dimensions.

The development of magnetic field sensors with effective areas ranging over several orders of magnitude as reported in Chapter 5.6 herein enables the investigation of the

scaling of low-frequency flux noise with device dimensions. Hence, it may experimentally prove current microscopic theories and may probably help to reveal the underlying noise mechanism.

Various SQUID magnetometer introduced within this thesis had been measured in a two-stage configuration as shown in Figure 5.4. It should be pointed out, that due to the low capacitance of the used cross-type junctions the white flux noise $S_\Phi^{1/2}$ typically amounts to about 1 $\mu\Phi_0/\mathrm{Hz}^{1/2}$ at 4.2 K, whereas magnitudes of $S_\Phi^{1/2}$ at 1 Hz as a measure for the low-frequency noise were determined to be in the range of about 1.4 to about 8 $\mu\Phi_0/\mathrm{Hz}^{1/2}$. The measured noise values and effective areas of these devices are listed in Table 5.3. The dimension of the junctions were $(0.8 \times 0.8)\ \mu\mathrm{m}^2$ except for magnetometer of type ML12 which had $(0.6 \times 0.6)\ \mu\mathrm{m}^2$ Josephson junctions. All junctions exhibit nearly the same critical current density of about 1.7 $\mathrm{kA/cm}^2$.

In addition to the multiloop magnetometer introduced in Table 5.2, a square washer-type SQUID called WS10µm with rather low effective area and $(1.0 \times 1.0)\ \mu\mathrm{m}^2$ Josephson junctions with about half the critical current density is appended. Detailed information can be found in [33] and in the Appendix B. It will be included in this discussion, as it allows to evaluate the scaling dependence for very low effective areas, probably enabling a better qualitative measure of the flux noise scaling with the effective area.

It should be noted, that another type of ML7 with $N = 8$ for the number of parallel connected loops is listed in Table 5.3 in comparison to the sensor with $N = 10$ in Table 5.2.

The washer for SQUID magnetometer of type ML4.5, ML7 and ML12 were slotted with a maximum width of superconducting structures of 60 µm, according to the design recommendations given in Chapter 5.2. According to results on solid and slotted versions of type ML2A discussed above, the motion of vortices as the source for an increased flux noise at 1 Hz is very unlikely. The width of individual superconducting structures in these three types is identical; they just differ in the number of parallel superconducting parts separated by narrow slots.

Figure 5.14 shows the dependence of the measured magnitude of flux noise at 1 Hz on the magnetometer effective area, as listed in Table 5.3. The different symbols correspond to

Table 5.3: Measured effective areas and corresponding magnitudes of flux noise at 1 Hz for a set of SQUID magnetometer. $S_{\Phi,1\mathrm{Hz}}^{1/2}$ was obtained from two-stage measurements at 4.2 K as described in Chapter 5.3. Parameters d_p/w_p are listed for comparison with recent theories.

Sensor name	effective area A_{eff} [mm^2]	$S_\Phi^{1/2}$ (1 Hz) [$\mu\Phi_0/\mathrm{Hz}^{1/2}$]	d_p/w_p
WS10µm	$1.3 \cdot 10^{-4}$	1.4 – 2.0	10
ML2A	0.36	3.4 – 4.0	31.3
ML4.5	1.83	4.9 – 5.3	20.5
ML7 (N=8)	4.35	5.5 – 5.8	15.1
ML12	8.00	6.8 – 7.8	12.7

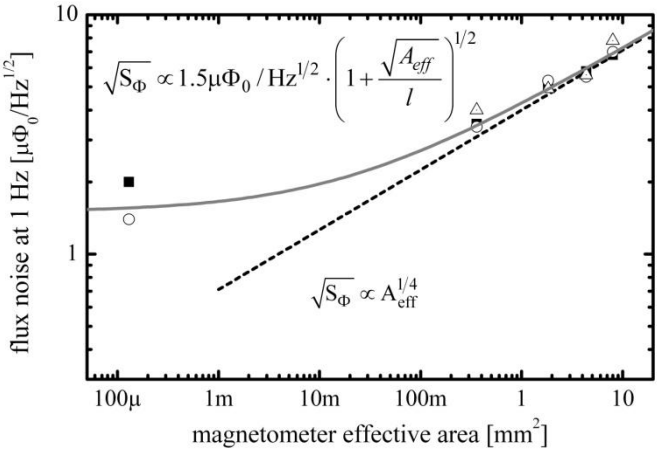

Figure 5.14: Dependence of measured magnitude of flux noise at 1 Hz on the magnetometer effective area. The different symbols correspond to the individual measured samples of each species. The dashed line represents a scaling as $S_\Phi^{1/2}$ (1 Hz) $\propto A_{\mathrm{eff}}^{1/4}$. For the solid line in addition to this scaling a saturation of $S_\Phi^{1/2}$ (1 Hz) for very small effective areas was assumed. The parameter l denote the cross-over length with an experimental found value l = 130 µm, as explained in the text.

individual measured samples. I would like to point out, that the spread between individual samples of each sensor type is rather low, although samples from different wafers have been chosen.

From the data given in Table 5.3 it is obvious that in contrast to recent investigations on qubits [156, 158, 160] the scaling of $S_\Phi^{1/2}$ (1 Hz) cannot be explained by the ratio d_p/w_p for the investigated devices. Here the magnitude of flux noise at 1 Hz increases slowly with increasing effective area of the multiloop magnetometers, whereas d/w continuously decrease.

The scaling dependence for sensors with A_{eff} larger than that of type ML2A can be described by $S_\Phi^{1/2}$ (1 Hz) $\propto A_{\mathrm{eff}}^{1/4}$, represented by the dashed black line. It is identical to a model proposed in [76]. Within this model is was supposed that magnetic noise is induced by single electrons spins located around the SQUID structure hopping on and off defect states due to thermal activation. The direction of the spins would be locked as long as the electrons are trapped, thus coupling magnetic signal into the SQUID. The superposition of many uncorrelated changes of spin direction would therefore sum up to the observed $1/f$ power spectrum [67]. Although the simulations which result in the reported fourth root dependence upon the effective area were based on a fixed ratio d_p/w_p as well as limited to maximum loop dimensions of about 100 µm, a reasonable good agreement could be found to the measured valued. The difference to the model predictions are most likely due to non-constant values d_p/w_p for the SQUIDs reported within this thesis as well as the much more complicated multiloop structure compared to the model's square washer-type SQUIDs. Consequently, in case of the multiloop magnetometer herein, the coupling of spins may differ from that in the simple square washer-type structure.

For effective areas below approximately 0.1 mm^2 the magnitude of flux noise at 1 Hz seems to saturate as could be seen in Figure 5.14. One may argue that the saturation for small effective areas is due to the critical current fluctuations in the Josephson junctions,

as the noise measurements were based on a direct coupled SQUID electronics. Therefore noise measurements at different working points on the slope with $\partial V/\partial \Phi \neq 0$ as well as on reversal points with $\partial V/\partial \Phi = 0$ were carried out to rule out this noise source. These measurements confirm that the observed magnitude of the low-frequency noise is due to magnetic flux noise in the SQUIDs, as described in [33].
The grey solid line in Figure 5.14 therefore includes a lower bound of about 1.5 $\mu\Phi_0/\mathrm{Hz}^{1/2}$ of the magnitude of flux noise at 1 Hz to account for this saturation. An experimental fit to the data according to equation

$$\sqrt{S_\Phi} \propto 1.5\,\mu\Phi_0 \big/ \mathrm{Hz}^{1/2} \cdot \left(1 + \frac{\sqrt{A_{\mathrm{eff}}}}{l}\right)^{1/2} \tag{5.3}$$

was done. The best approximation was achieved for the parameter l = 130 µm.
I want to point out, that this length coincides with the recently proposed noise source correlation length in qubits of between 6 to 400 µm [162]. It is a matter of further analysis, if the same correlation mechanism is valid also at 4.2 K. The investigation of SQUID magnetometers with effective areas covering this crossover range may give more precise information on the noise source correlation length. In addition, the temperature dependence of the observed low-frequency flux noise may provide even more insight in the noise mechanism in future experiments.
More recently, numerical simulations had shown that contributions from spins located at the edge of superconducting films, which had been neglected in all previous investigations, are significant or even dominant in narrow-linewidth loops, which may explain the observed saturation [163].

To summarize, a clear dependence of the scaling of low-frequency flux noise ${S_{\Phi,1\mathrm{Hz}}}^{1/2}$ at 4.2 K with the magnetometer effective areas has been observed. For effective areas larger about 0.1 mm^2 the experimentally found scaling law as ${S_\Phi}^{1/2}$ (1 Hz) $\propto {A_{\mathrm{eff}}}^{1/4}$ coincides with recently reported simulations on qubits. Accordingly, most probable candidates are localized electron spins at the surface of the superconductor. By changing these surface conditions one therefore may be able to improve the low-frequency noise performance of these devices.
Nevertheless, the obtained results on SQUID magnetometer presented in this chapter clearly indicate their suitability in a geophysical receiver system for transient electromagnetics, which is the focus of the next chapter. In particular it should be emphasized, that the sensors based on cross-type Josephson junctions with sub-µm dimensions exhibit an increased usable voltage swing, improved intrinsic sensor noise performance, and especially strongly increased stability against magnetic background fields during cool-down as well as during operation in applied magnetic fields.

6 A geological receiver based on the developed SQUIDs

This chapter will follow the development track towards a highly sensitive detection system for transient electromagnetics. Therefore, a realization concept based on low capacitance sub-micrometer cross-type Josephson junctions was developed. This concept faces the three fundamental requirements for the intended purpose of an unshielded measurement system for geophysics. First, according to relation (2.12) due to a decreased total junction capacitance an improved sensitivity of the developed SQUID sensors is expected, which was experimentally demonstrated in Chapter 5. As discussed in Chapter 2.3 narrow linewidth structures in combination with a small size of superconducting structures at or around the Josephson junctions should lead to an improved field stability of the SQUIDs. In Chapter 5.4 and 5.5 this has been successfully shown for static magnetic backgrounds as well as for applied magnetic fields during operation.
Another requirement, a sufficiently large slew rate of the measurement system, results from the intended purpose as a geophysical receiver system for transient electromagnetics. Within this chapter I will therefore discuss this requirement in more detail and state on the concept and composition of the developed geophysical receiver system. In Chapter 6.2 I will show results of the lab characterization of this system. Finally, in Chapter 6.3 I will present a characterization method to demonstrate the system's low-frequency noise in an unshielded environment. At the end of this chapter results from a ground based field application will be used to demonstrate the systems performance.

6.1 Concept and composition of the SQUID system

The transient electromagnetic method which uses an electromagnetic pulse to induce eddy currents in a nearby conductor was introduced in Chapter 1. The pulse is created by switching off a current through a transmitter coil. In this time an eddy current system is induced, which dissipates downward and outward in time. This eddy current system causes a decaying magnetic field. The decay rate in time is a function of the conductivity σ and the depth of the according conductor. By measuring the decaying secondary magnetic field one can deduce a conductivity profile underneath the particular measurement location. Figure 6.1 (left) shows a typical time segment in TEM for a square transmitter waveform. Therein the primary field acting on a conductor is indicated as a black line by a current through the transmitter coil. The decaying secondary field

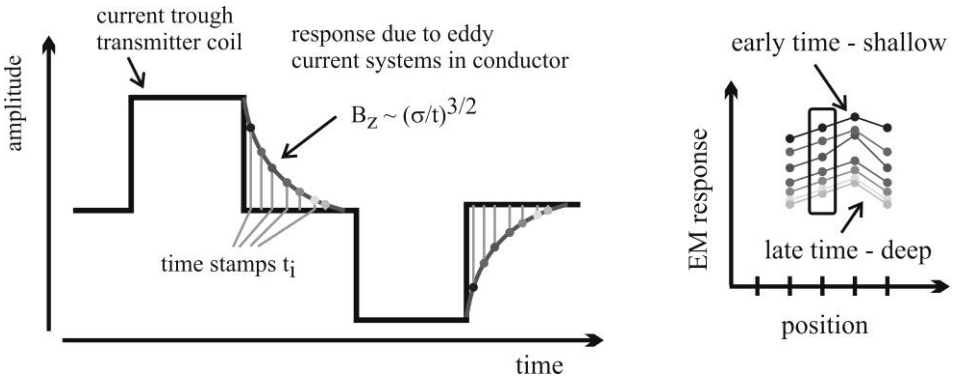

Figure 6.1: Left: Typical time segment of a square transmitter waveform in transient electromagnetics. The change of the primary field indicated by the current trough the transmitter loop cause an eddy current system in a nearby conductor. The decay of the induced secondary field due to this eddy current system is indicated as a grey line. Right: The amplitudes at specific time stamps t_i are plotted versus the actual measurement position, shown as encircled points in this picture.

$B(t) \propto (\sigma/t)^{3/2}$ according to equation (1.1) is shown as a grey solid line. The secondary magnetic field amplitudes at specific time stamps t_i, which are typically logarithmically spaced, are plotted vs. the measurement position on a profile, as shown in Figure 6.1 (right). The amplitudes shown in the time segment on the left correspond to the encircled measurement at a particular position on the right. In order to improve signal to noise ratio the obtained data are typically averaged over several measurement cycles. However, this *stacking* limits the speed of exploration and thus impacts on the survey costs. Performing this measurement procedure at several positions leads to a two dimensional conductivity profile along the mapping direction.

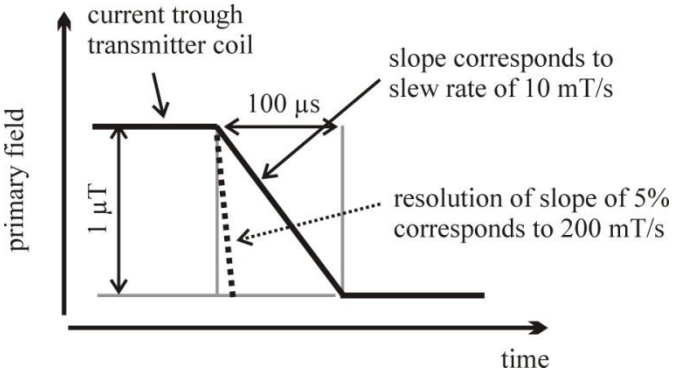

Figure 6.2: Estimation of required system slew rate for transient electromagnetics. The current through the transmitter coil produces a primary field of about 1 µT at the position of the SQUID system. The switch off of this current in about 100 µs results in a lower limit of the required slew rate of about 10 mT/s just to follow this switching. A 5 % resolution of the slope corresponds to about 200 mT/s.

By taking a closer look at the time when switching off the primary field, the required system slew rate – the maximum flux change the system can follow within a certain time span – will be estimated. The maximal magnitude of the primary field amounts to about 1 µT at the position of the SQUID for the intended application. The transmitter current is typically switched off in less than 100 µs which results in a slew rate of about 10 mT/s. This is illustrated in Figure 6.2. For the magnetometer of type ML2A presented in Chapter 5 exhibiting an inverse effective area of about 5 nT/Φ_0 this corresponds to a requirement of about 2 MΦ_0/s. For an accurate interpretation of the measured data a good resolution of this slope is necessary, as this provides information on shallow sources. An envisaged resolution of the slope of 5 % corresponds to a required system slew rate of about 200 mT/s or 40 MΦ_0/s.
The intended operation of the SQUID system imposes, besides the slew rate several, other demands on a measurement system as discussed e.g. in [164]. Although main information on conductive targets can be achieved by just the vertical component of the secondary response, typically the shape of the conductor can more precisely be estimated by additional horizontally information. Thereafter, the receiver system should contain an orthogonal triple of the developed SQUID magnetometer. They are mounted at the bottom of a cryostat made from fiberglass reinforced plastic [165].
The SQUIDs are connected via twisted copper wires to a direct-coupled readout electronics mounted on top of the cryostat. The electronics, which is similar to the one used within this thesis to determine the sensor performance, has been described in detail in [78]. As specified therein it is optimized with respect to a low input voltage noise, a high bandwidth, a low power consumption, and low temperature drift within a temperature range between 0°C to 65°C. For the operator's convenience the optimal working point for each SQUID can be set up automatically by means of a microcontroller via a personal computer.
To increase the system stability and to limit the system bandwidth to about a few hundred kHz an rf shield of several layers of aluminum coated mylar foil was wrapped around the cryostat. Special care need to be taken in the design and the mounting of this foil because it could cause eddy current systems to flow very close to the SQUID sensors.
The power supply, which is situated several meters apart the SQUID receiver system contains all parts which necessarily do not be located close to the SQUIDs. These are e.g. lead gel batteries for continuous operation of up to 12 h. The power supply also exhibits BNC outputs of the FLL which can be digitized by a subsequent ADC. This output has been used for the characterization shown in the next chapter.

6.2 Lab-Characterization

In the presented receiver system SQUID magnetometer of type ML2A are used. These sensors exhibit a usable voltage swing of about 160 µV within the system, which is close to the value as determined before in a dipstick probe inside a lead and µ-metal shield. The effective area of the sensors have been measured in a Helmholtz coil system [138] which is supplied with a low-frequency sinusoidal signal. The whole cryostat is placed inside the

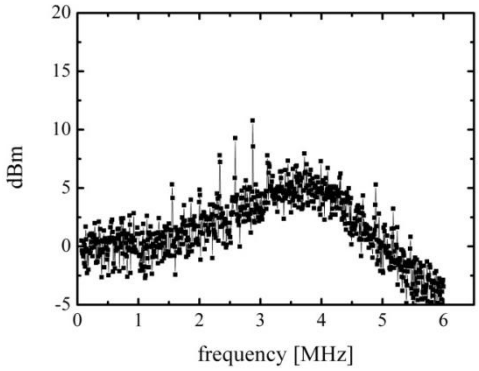

Figure 6.3: The bandwidth of channel x was determined to about 5.6 MHz, showing a slight +4 dB overshot at 3.7 MHz due to the used settings of the two-pole integrator.

coil. The current through the Helmholtz coil is determined by the measured voltage of a known precise series resistor. The resultant voltage at the FLL output was measured with a lock-in amplifier. From the corresponding coil constant, the transfer factor of current through the coil to magnetic field amplitude, and the voltage change per flux quantum at the output of the FLL, which was determined before as the system was placed inside a three layer μ-metal cylinder, the inverse effective area of the SQUID magnetometer were determined to about 5.55 nT/Φ_0.

As briefly discussed in Chapter 2.4, the choice of the feedback resistor results from a tradeoff between sufficiently low noise, high dynamic range and slew rate of the receiver system.

Together with the effective area as determined above, the desired magnetic field noise of below 20 $fT/Hz^{1/2}$ results in a maximum flux noise of about 3.6 $\mu\Phi_0/Hz^{1/2}$. In order to be well below the demanded magnetic field resolution, a safety factor of about 2 was introduced. Thus, the maximum flux noise of the SQUID together with the entire FLL including contributions from feedback resistors should be below about 1.8 $\mu\Phi_0/Hz^{1/2}$. Under the assumption of a flux noise of about 1 $\mu\Phi_0/Hz^{1/2}$ for the SQUID in a single stage configuration as well as uncorrelated noise of the feedback resistors, the SQUID, and other components of the FLL, the maximum contribution of the feedback resistors should be below 1.5 $\mu\Phi_0/Hz^{1/2}$ to meet these demands. This flux noise value sets a lower limit for the feedback resistor R_{Fb} of about 290 Ω, as the feedback coil is coupled inductively to the SQUID by a mutual inductance of about 5.1 $\mu A/\Phi_0$.

Following the discussion in Chapter 1.5, the receiver system should feature a minimum dynamic range of ± 2.5 μT. For an inverse effective area of about 5.55 nT/Φ_0 this corresponds to about 450 Φ_0. With a maximum output voltage of the FLL of the order of ± 1.25 V this corresponds to 2.8 mV/Φ_0. This results an upper limit for the feedback resistor of about 540 Ω for the given mutual inductance of the feedback coil.

As a tradeoff, a value of the feedback resistors of about 500 Ω was choosen in favor of a lower system noise. For this configuration the coupling, which equals one Φ_0, amounts to about 2.4 mV/Φ_0 at the output of the FLL. Hence the maximum flux range results in about ± 520 Φ_0, which corresponds to about ± 2.88 μT.

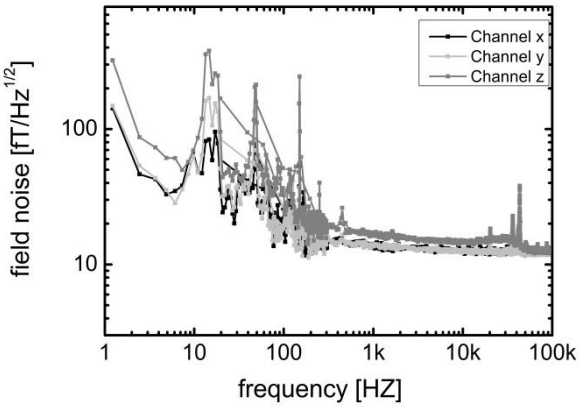

Figure 6.4: Measured field noise of three orthogonal channels in the receiver system measured inside a magnetically shielded room at IPHT Jena.

With the used configuration of feedback resistors and integrator settings, a typical system bandwith of about 5.5 MHz was achieved as shown in Figure 6.3. A slight overshot of about +4 dB at about 3.7 MHz is visible which is caused by the used settings of the two-pole integrator. The integrator values have been experimentally determined as a tradeoff between slew-rate and stability of the system.
In order to prove the stability of the system, the cryostat was placed inside a magnetically shielded room and the FLL output voltage was monitored with 24 bit ADCs [109] already introduced in Chapter 5.3. Long time series data were recorded for a whole day, while the system being locked. During this time no flux jumps have been observed. From this time series the system noise was calculated by means of FFT. Figure 6.4 shows the magnetic field noise of the three orthogonal magnetometers in the system. Above about 1 kHz one can clearly see a white noise level of about 12 $fT/Hz^{1/2}$ for channels x and y, whereas the noise of channel z, vertical to the floor, was slightly higher. This is caused by the noise of the shielded room wall close to the vertically sensitive SQUID, as the cryostat was placed closely above the floor. Above about 50 kHz it reduces to the intrinsic system noise for this channel. With the measured effective area this corresponds to a white flux noise of about 2.2 $\mu\Phi_0/Hz^{1/2}$, which is slightly above the expected value as discussed above. This is most likely caused by high-frequency noise sources acting on the SQUID, which can be seen in the fact, that the voltage swing within the system is slightly reduced compared to the dipstick characterization using heavy filtering. Accordingly, the above discussed 1 $\mu\Phi_0/Hz^{1/2}$ probably underestimates the flux noise of the SQUID within the receiver system. However, the measured white flux noise density is still well below the discussed requirements.
At frequencies below 1 kHz the system noise could not be determined due to the insufficient magnetic shielding, which let the strong amplitudes of the 50 Hz and harmonics from the local electric power line as well as a peak at about $16\,^2/_3$ Hz presumably originating from the railway power line be clearly visible.

To determine the low-frequency noise performance of the system measurements have been performed in the shielded room BMSR-1 at the PTB in Berlin. Figure 6.5 show

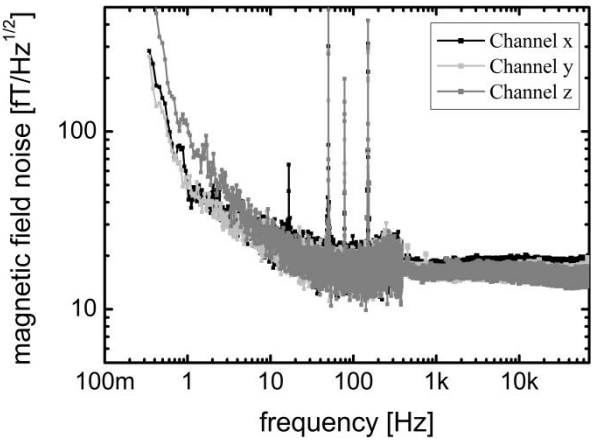

Figure 6.5: Magnetic field noise of a set of three orthogonal SQUID magnetometer of type ML2A deployed in a multi-purpose receiver system measured inside the shielded room BMSR-1 at PTB, Berlin.

results of a comparable so-called *multi-purpose* receiver system, as will be discussed in Chapter 6.3. The shown noise spectra correspond to a set of three orthogonal SQUID magnetometer of type ML2A. Due to the much better shielding at low frequencies, the white noise region is visibile down to several Hz. At 10 Hz it amounts to about 20 fT/Hz$^{1/2}$ and therefore comply the requirements as stated in Chapter 1.
However, even under these well magnetically shielded conditions a strong increase in the observed noise below about 1 Hz is visible. Accordingly it might by difficult to determine the intrinsic noise for multiloop SQUIDs of type ML2A. The task is getting even harder if sensors with larger pickup loop dimensions developed within this thesis (cf. Chapter 5.6) are used, since they provide better magnetic field resolution within the system. Furthermore, the conditions within the shielded room do not represent those in the presence of signal or the Earth's magnetic field. In Chapter 6.3 I will therefore briefly comment on recent field tests where the intrinsic noise of SQUID magnetometer of type ML7 have been determined in an unshielded environment.
According to [71] the dynamic range of a SQUID systems is defined as the feedback range divided by the white flux noise. The dynamic range amounts to about $2{\cdot}520\ \Phi_0/2.2\ \mu\Phi_0/\mathrm{Hz}^{1/2} = 4.7{\cdot}10^8\ \mathrm{Hz}^{1/2}$ for the developed system herein.
In a 1 Hz bandwidth the dynamic range can be calculated as [166]

$$DR = 20 \cdot \log\left(\frac{2 \cdot 520\ \Phi_0}{2.2\mu\Phi_0 / \mathrm{Hz}^{1/2} \cdot \text{crest factor}} \right). \tag{6.1}$$

Taking a crest factor of 4 [167] this results in $DR \approx 161$ dB ≈ 27 Bit.

The system slew rate was determined from the maximum sinusoidal flux the FLL can feed back without unlocking. For this investigation the cryostat was placed inside a three layer mu-metal cylinder. A small wire-wound copper coil was attached directly at the outside of the cryostat. First, the coupling of this coil to the SQUID was determined by

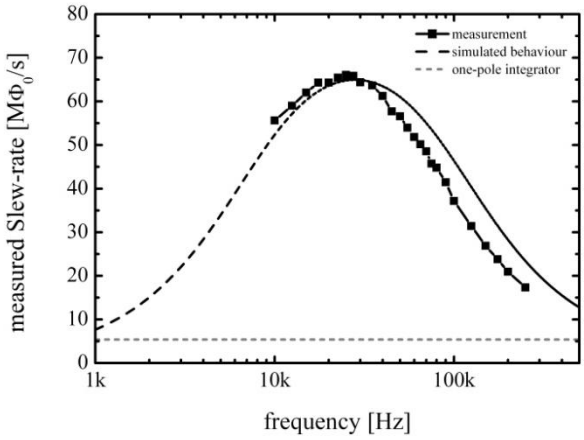

Figure 6.6: Measured frequency dependent slew rate of channel z. For the calculation of the slew rate in case of a one-pole integrator the following parameters have been used: f_{3dB} = 5.4 MHz, $\Phi_{lin} = \Phi_0/(2\pi)$.

the FLL output voltage per flux quantum $V(1\Phi_0)$, with the FLL being in feedback mode. Afterwards the amplitude of a sinusoidal current through this coil with a fixed frequency f was raised until the FLL got unstable. As a criterion for stable operation I considered zero flux jumps for at least a time interval of one second. For typical slew rate values in the $M\Phi_0$/s range, this represents less than one flux jump for $1 \cdot 10^6$ Φ_0 the FLL correctly fed back to the SQUID.

From the according FLL output voltage V_{FLL} at this point the system slew rate was calculated according to [78]

$$\dot{\Phi}_{max} = \Phi_{SQUID} \cdot \pi \cdot f = \frac{V_{FLL}}{V(1\Phi_0)} \cdot \pi \cdot f . \qquad (6.2)$$

The filled squares in Figure 6.6 show the measured slew rate according to this procedure. As the SQUID electronics comprise a two-pole integrator, as in detail described in [78], the slew rate is frequency dependent and was therefore determined for several frequencies of the coil current. In these measurements the number of flux quanta typically seen by the SQUID was in the range of several hundred.

Accordingly, the maximum slew rate was determined to 66 $M\Phi_0$/s at about 25 kHz. One can see a decrease towards smaller frequencies, where the slew rate is limited by the maximum output voltage of the FLL. At higher frequencies the decrease is due to decrease of the open loop gain.

Together with the measured data the simulated behavior of the FLL is shown as a dashed black line, showing excellent agreement to the measurement results. A model given in [78] was used to simulate the behavior. In addition, the calculated slew rate for a system with one-pole integrator is shown as dashed grey line. According to [71] in this case the maximum slew rate amounts to $2\pi f_{3dB}\delta\Phi$, which is about 5 $M\Phi_0$/s for a 3 dB cut-off frequency of about f_{3dB} = 5 MHz and an assumed linear flux range $\delta\Phi$ of about $\Phi_0/2\pi$. Therefore, the system slew rate increased up to a factor of 13 compared to commonly

used one-pole integrator systems. From the effective area of these sensors, the maximum slew rate corresponds to about 360 mT/s in terms of a magnetic field change. It is worth to note, that this is well above typically achieved values, as e.g. given in [168]. This value could even be enhanced by decreasing the value of the feedback resistor or increasing the mutual inductance between the feedback coil and SQUID, as both results in an increase of the dynamic range. However, according to equation (2.16) this will increase the thermal noise from the feedback resistor seen by the SQUID.

6.3 Field tests

The investigation of noise of a complete SQUID system is very challenging compared to the measurement of the SQUID's intrinsic noise discussed in Chapter 5.6. Due to the physical size of the cryostat no appropriate magnetic shielding with a shielding factor comparable to a superconducting shield can be applied. Especially the determination of the low-frequency noise properties of a highly sensitive SQUID system is often impossible even in magnetically well shielded rooms due to their limited low-frequency shielding factor. The use of a reference sensor inside of a magnetically shielded room does not help too, since the residual magnetic field inside of the shielded room is often too inhomogeneous. In addition, the measured system performance at low frequencies may even not correspond to the one in presence of and/or if the device was cooled down in the Earth's magnetic field because flux trapped in the SQUID structures may strongly deteriorate the sensor noise.

Thus another way has been proposed in the past [169] in order to evaluate the intrinsic noise of high sensitive magnetometers and to compare their performance in a real application scenario. The method is based on synchronous unshielded measurement with two comparable systems in a magnetically quiet area without electric conductivity anomalies in the subsurface. As described in detail in [170], measurements with two identical so-called *multi-purpose* receiver systems, similar to the prior introduced TEM system, have been performed. These systems comprise two orthogonal magnetometer triples. The low sensitive triple consists of magnetometer of type ML2A which have been developed and characterized in the framework of this thesis and used in the system described in Chapter 6.2. The high sensitive magnetometers are of type ML7 which are introduced in detail in Chapter 5.6. Whereas the low sensitive triple is used for active transient electromagnetics, the high sensitive one enables the use in other geophysical measurement methods like audio-frequency magnetics (AFMAG), magnetic induced polarization (MIP), magnetotellurics (MT) or controlled source audio magnetotellurics (CSAMT).

For the measurement, time series of two identical systems have been recorded simultaneously with a SMARTEM24 receiver [171]. Both system coordinate axes were aligned in parallel to each other. The cryostats were completely buried close together to most probably detect the same external signal. Figure 6.7 (left) shows noise spectra obtained for a measurement in northwest Delta, Utah, USA, as reported in [170]. Obviously there is a good correlation between SQUIDs with parallel sensitive axes,

indicating the good alignment between the two systems. Accordingly one may determine the intrinsic system noise by an adequate correlation technique.
In [170] two approaches have been presented, based on either the calculation of the cross-correlation or the subtraction of two time-domain signals. Therein it has been shown that under almost optimal conditions both methods result in the same white noise levels. Under the assumption of a perfect alignment, which according to Figure 6.7 (left) is roughly fulfilled in the presented measurement setup, one can also simply subtract corresponding signals in the time-domain. Figure 6.7 (right) shows the estimated intrinsic noise of the SQUID system according to this method. The intrinsic system noise for the ML7 SQUIDs amounts to about 1.2 to 1.5 $fT/Hz^{1/2}$ in the white noise region ranging roughly from 100 Hz to higher frequencies.
Unfortunately, at low-frequencies there is still the influence of well-known geophysical signals observable in the z channel, which is perpendicular to the soil. One can therefore conclude that this estimation does not give the intrinsic low-frequency noise of the system. As discussed in [170] even a small tilting of only 10^{-9} rad may account for the strong increase in the low-frequency range. Further investigation with improved tilt measurement sensors may clarify this question and may prove the capability of the presented approach to determine the intrinsic system noise.

Now I will show results of a field test with such a *multi-purpose* SQUID system in order to demonstrate the system performance. The low-sensitive triple was used for the results of the field tests presented herein. The measurement had been performed in an in-loop configuration [7]. That means that the SQUID receiver was places in the center of the transmitter loop and that both are moved simultaneously. This method results in a high spatial resolution and in easy interpretable data. A Zonge ZT transmitter [172] was used to power the transmitter coil, which had a side length of $(200 \times 200)\ m^2$. Data was recorded with a SMARTEM24 [171] receiver with a stacking of 32 decay curves. The cycle frequency was 0.125 Hz. With a duty cycle of 50 % of the square waveform, this corresponds to on- and off-times of 2 s, respectively.

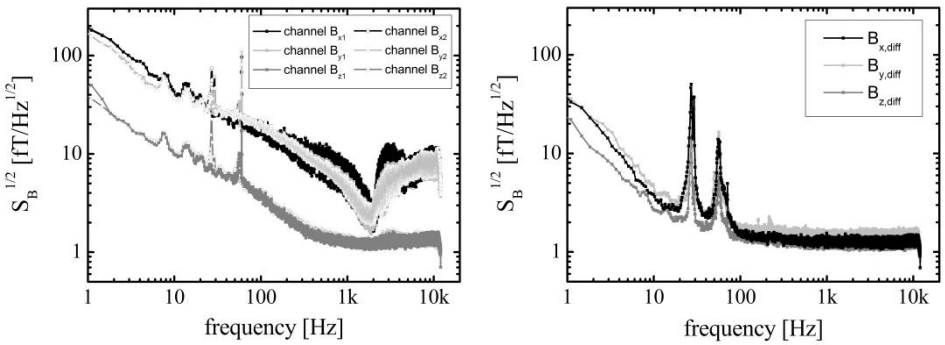

Figure 6.7: (left) Unshielded noise of two highly sensitive SQUID triples, acquired simultaneously northwest of Delta, Utah, USA. Note the good correlation between the channels in parallel. (right) Intrinsic noise of the SQUID system calculated by subtraction of corresponding reference signals in the time domain.

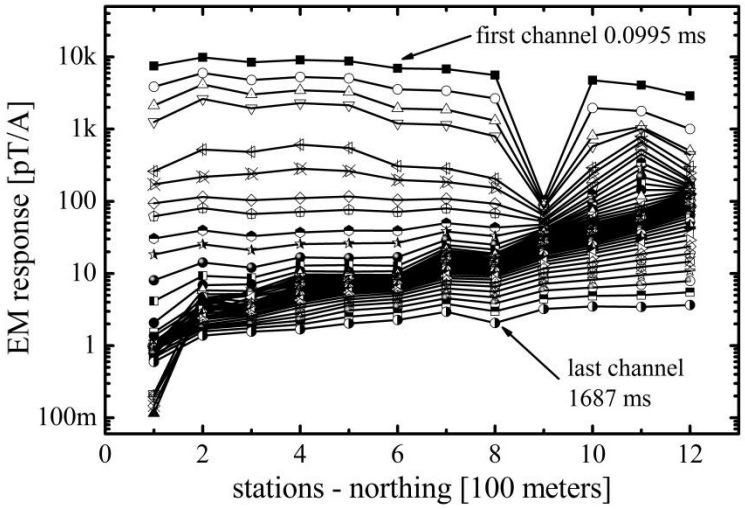

Figure 6.8: EM response of the z channel, which is perpendicular to the soil surface. Note that even the latest channel with about 1.7 s show noise free behavior.

Figure 6.8 shows the measured EM response for the z channel, which is perpendicular to the surface of the soil. As already pointed out, each curve represents a certain time window after switching off the primary field. These time channels are logarithmically spaced ranging from 995 µs to about 1.7 s. There is obviously a strong signal for early times visible. The dip at early times for station number 9 represents a locally increased conductivity in the shallow subsurface. Furthermore, an accumulation of EM responses is visible for intermediate times, which dips to the south; that is for small station numbers. For a measurement station in the middle it corresponds to times between about 10 to 100 ms. It can be interpreted as a strong change of conductivity, as can be seen in the conductivity depth inversion in Figure 6.9.

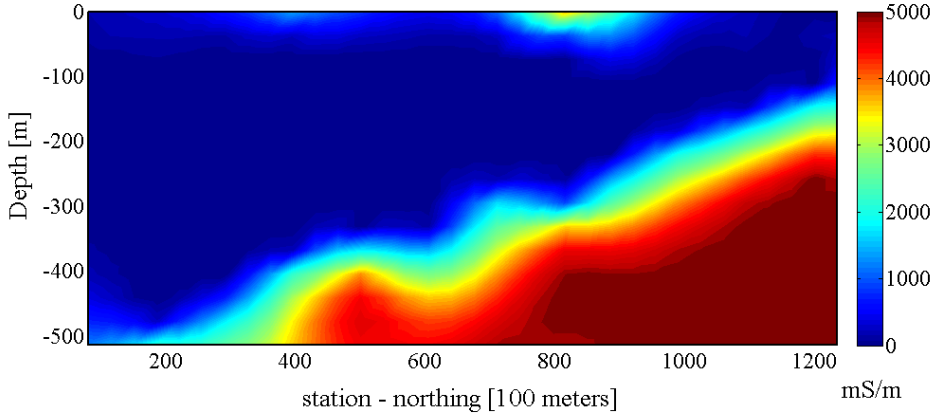

Figure 6.9: Conductivity depth inversion data modeled from the shown EM response of Figure 6.8 as explained in the text.

The data shown therein give the electrical conductivity of the soil for depths up to 500 m. Thereafter the overburden was modeled with a conductivity of about 10 Ωm. The underlying conductor, starting at a depth of about 200 m in the north and dipping with about 20° to the south was modeled with a conductance of about 0.25 Ωm.
It is worth to note, that even the last channel with about 1.7 s show almost noise free behavior. This enables geophysical investigations even at later times with this receiver system, corresponding to larger exploration depths. Moreover, the data quality allows a reduction of data averaging to increase the mapping speed.

6.4 Concluding remarks and outlook

In summary, the concept and composition of the developed geophysical receiver system has been shown together with results obtained from the lab-characterization as well as from ground based TEM field applications. In detail the receiver system noise was determined to fulfil the requirements set out in Chapter 1.5 regarding the sensitivity, dynamic range and slew rate. Accordingly, a white magnetic field noise of 12 $fT/Hz^{1/2}$ together with a dynamic range of ±520 Φ_0 corresponding to about ± 2.88 µT and system slew rates up to 66 $M\Phi_0/s$ has been measured.
Ground based field tests of a similar *multi-purpose* SQUID receiver systems showed their excellent suitability for transient electromagnetics. Up to now five of these *multi-purpose* system are operated by Anglo American [173] within the field and have already led to interesting geophysical studies and few deposit discoveries.

Appendix

Beyond the scope of this thesis, I would like to address several adjacent topics that have been investigated during my PhD. They should be briefly included within this thesis and allow an insight view on what was recently achieved in using the technology and sensors developed herein. On one hand they emphasize the importance of the introduced fabrication technology and its potential to open new application areas and one the other hand have led to interesting insights e.g. respect to the low-frequency noise in SQUIDs. More precisely, I will show results on integrated SQUID current sensors [32] beneficial in many very demanding applications ranging from the use e.g. in MRI systems for biomedical applications to the readout of radiation detectors like transition edge sensors (TES) or even the readout of devices based on single charging effects. Furthermore, miniature SQUID magnetometer based on cross-type Josephson junctions offer a possibility to overcome limitation in nowadays nanoSQUIDs, which are mostly based on constriction type junctions. In a proof-of-principle they have already shown to offer a great potential respect exceptionally low flux noise levels [33].
Moreover, I will comment on concepts for next generation geophysical measurement systems, like an on-chip linearization of the SQUID magnetometer output voltage [36] allowing to considerably improve the system slew rate or the absolute measurement of the Earth's magnetic field [35]. First steps have been taken as well towards the development of bi-SQUIDs as linear SQUID amplifier [34] probably suitable for the integration in such concepts or electrically small antenna.
Finally, I will comment on the continuation of the fabrication technology to deep submicron Josephson junctions with critical current densities of up to 20 kA/cm^2 [31].

A SQUID current sensors

As described in Chapter 2, SQUIDs are one of the today's most sensitive detectors for magnetic flux. They can be used as sensitive magnetometers like within this thesis or can be used to measure any physical quantity that could be transformed into magnetic flux. For this purpose, typically an integrated input coil on top of the SQUID washer produces a magnetic flux in the SQUID and the SQUID forms a current sensor with inductive input impedance.
Today's commercially available single SQUID current sensors with integrated input coils typically exhibit white noise levels of about 1 $pA/Hz^{1/2}$ [136, 174, 175]. Using an additional flux transformer [176] like in a cryogenic current comparator (CCC) offer the potential to improve the current resolution further and values as low as 4 $fA/Hz^{1/2}$ have been reported [177]. However, a convenient application demands for more robust and less

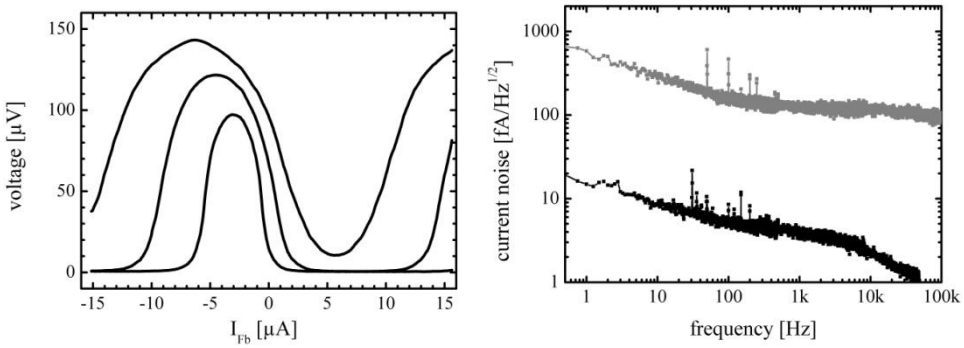

Figure A.1: Left: Flux-voltage characteristics of the current sensor SQUID. The bias currents were 11.2 µA, 12.5µA and 14 µA, respectively. Right: Noise spectrum of the current sensor SQUID without (grey) and with (black) additional flux transformer measured at 4.2 K.

bulky versions, which recently lead to several attempts of thin-film variants with white noise levels of 110 fA/Hz$^{1/2}$ [178] and 25 fA/Hz$^{1/2}$ [179].

To demonstrate the sensitivity improvement of SQUIDs based on low capacitance cross-type Josephson tunnel junctions a SQUID-based current sensor was developed. Details of the sensor are discussed in detail in [32]. The SQUID with a total chip size of (2.5 × 2.5) mm^2 is based on a clover leaf structure as reported in [180]. The total SQUID inductance amounts to 180 pH. The Josephson junctions have a size of (0.8 × 0.8) µm^2. The integrated input coil has 30 turns on each washer, which results in a mutual inductance between input coil and SQUID of M_{in} = 18.2 nH. The input coil inductance amounts to L_{in} = 2.7 µH. Figure A.1 (left) shows the measured flux-voltage characteristics of the SQUID. The low junction capacitance obviously results in a large usable voltage swing of nearly 150 µV$_{pp}$. The readout with a direct-coupled SQUID electronics [136] results in a current noise of $S_I^{1/2}$ = 110 fA/Hz$^{1/2}$ at 4.2 K which is presented by the grey line on the right hand side in Figure A.1. This corresponds to a coupled energy resolution of $\varepsilon_C = S_I \cdot L_{in}/2 \approx 30$ h at 4.2 K, with h being Planck's constant.

Furthermore, the combination with an additional thin-film flux transformer [32] enhances the input coupling of the SQUID to about 4.1 nA/Φ_0. The input current noise, shown as a black line in the right hand side of Figure A.1, was measured with a SQUID preamplifier in a two-stage configuration. The white noise level amounts to 3 fA/Hz$^{1/2}$, corresponding to a coupled energy resolution $\varepsilon_C \approx 65$ h as expected for ideal matching of the SQUID and transformer. It is worth to note, that the current noise is below about 5 fA/Hz$^{1/2}$, 10 fA/Hz$^{1/2}$ and 15 fA/Hz$^{1/2}$ at 100 Hz, 10 Hz and 1 Hz, respectively. Note that the decrease at about 10 kHz is caused by the limited bandwidth of the SQUID electronics.

In summary, this exceptionally low current noise has never been reported for integrated thin-film SQUIDs before. The compact and robust design offers a great potential compared to their wire-wound CCC counterparts which are typically applied in this range of current resolution.

B Miniature SQUIDs

The SQUID magnetometer developed within this thesis aim for low magnetic field noise spectral densities $S_B^{1/2} = S_\Phi^{1/2}/A_{eff}$, as described in Chapter 2.3. To meet the sensitivity requirements for a certain application, the magnetometer effective areas are typically increased.

In contrast, miniature SQUIDs – SQUID magnetometer with very small effective areas – typically aim for high spatial resolution needed for instance in SQUID microscopy or for an enhanced coupling to single electron spins. For the investigation of small spin systems the figure of merit is the sensitivity to a magnetic moment. According to [33], for a SQUID configuration depicted in the left hand side of Figure A.2 the total flux Φ coupled to a square loop with side-length 2*a* from a magnetic dipole *m* placed in the center can be calculated by

$$\Phi = \frac{2\mu_0}{\pi}\int_a^\infty dx \int_0^x \frac{m}{(x^2+y^2)^{3/2}}\,dy = \frac{\sqrt{2}\mu_0}{\pi}\frac{m}{a}. \qquad (A.1)$$

It is obvious, that by decreasing the loop diameter the flux coupled to the SQUID increases. Accordingly, the minimum detectable number of electron spins can be expresses by

$$S_n = \frac{\pi}{\sqrt{2}} \cdot \frac{a \cdot \sqrt{S_\Phi}}{\mu_0 \mu_B}. \qquad (A.2)$$

Here μ_0 and μ_B are vacuum permeability and Bohr magneton, respectively.

In recent years many attempts have been done for the development of miniature or even nanometer-sized SQUID sensors [181-186]. Most of them are based on constriction type junctions, as conventional window type junctions typically exhibit µm-dimensions, which obviously exclude the fabrication of SQUIDs with loop diameter of 1 µm or even less. However, these constrictions often require subsequent trimming of the junction parameter

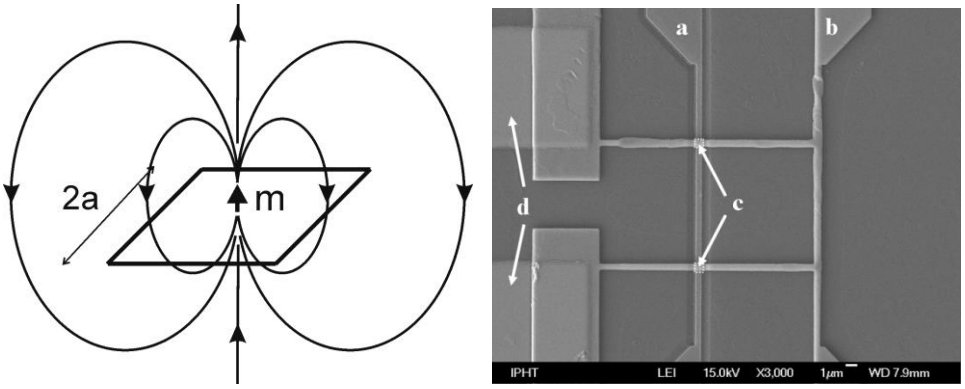

Figure A.2: Left: Schematic showing the coupling of a magnetic moment *m* to a square washer SQUID with side length 2*a*, indicated by the black square. Right: Scanning electron microscope image of a square washer SQUID as described in the text. The inner side-length is 10 µm. The Josephson junctions are indicated by dotted squares (c). (a) represents the trilayer, (b) the Nb wiring layer and (d) the AuPd shunts.

or are limited to a reduced temperature range.
These limitations can easily be overcome by the presented cross-type technology. In addition, the low junction capacitance may lead to significant improvements in device sensitivity. The SIS junction technology has proven to allow the reproducible fabrication of SQUID arrays too, thus offering e.g. miniature SQUID magnetometer arrays for SQUID microscopy.
According to the above equations, one can conclude that in a particular square washer configuration the coupling to a SQUID with a side-length of 500 nm amounts to about 10 $n\Phi_0/\mu_B$. According to equation (2.12) the expected flux noise spectral density for such a SQUID with an estimated inductance of about 1.5 pH and (0.6 × 0.6) μm^2 Josephson junctions results to about 10 $n\Phi_0/Hz^{1/2}$. Although SQUIDs with such small inductances impose the need for rather large critical current densities to meet the requirement $\beta_L \approx 1$ for optimum energy resolution, first tests on single junctions with an increased critical current density of up to 20 kA/cm^2 show very promising results, as will be shown in Appendix F. It therefore does not seem beyond the realm of possibility to reach the ultimate goal of single spin resolution in such devices. Furthermore, it is well known, that the coupling improves, if the magnetic particle is placed off-center or close to a narrowed section of the SQUID loop.

In order to prove the feasibility of this concept, a square washer SQUID has been developed. One example is shown in a scanning electron microscope image on the right side of Figure A.2. The inner side-length is 10 µm. With a junction size of (1 × 1) μm^2 in [33] a white flux noise level of 0.5 $\mu\Phi_0/Hz^{1/2}$ has been reported, even with an explicit non-ideal McCumber parameter of $\beta_C \approx 0.03$.
In a recently optimized sensor with (0.8 × 0.8) μm^2 Josephson junctions and $\beta_C \approx 1.18$ the flux noise reduced further down to 0.23 $\mu\Phi_0/Hz^{1/2}$, as expected. On the right side of Figure A.3 the measured flux noise spectral density of the optimized device is shown. For this measurement the two-stage configuration described in Chapter 5.3 was used. The measurement had been performed while the chip was immersed in liquid helium. It is important to note, that the increase in low-frequency noise is mainly due to magnetic flux

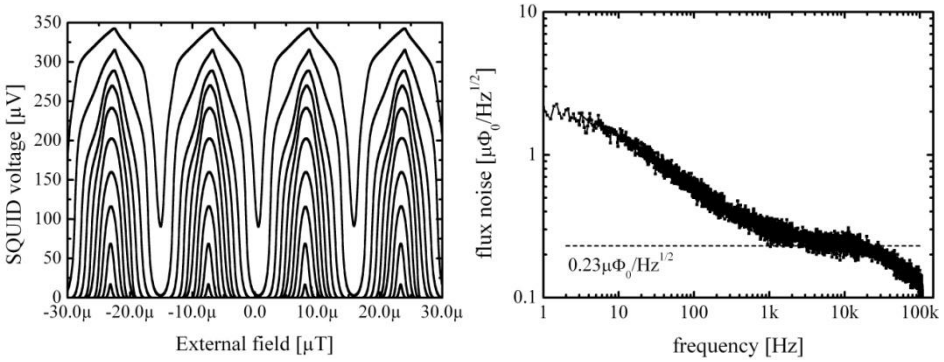

Figure A.3: Left: Flux-voltage characteristics of the miniature SQUID as described in the text. The bias currents range from 10 µA to 32.5 µA in steps of 2.5 µA. Right: Flux noise spectral density of the optimized miniature SQUID measured at 4.2 K.

noise as discussed in Chapter 5.7. The left side of Figure A.3 presents the flux-voltage characteristics of the device. The usable voltage swing accounts to more than 300 μV_{pp}. If a direct readout with dc-coupled room-temperature SQUID electronics [136] was used, a very low white flux noise of 0.3 $\mu\Phi_0/Hz^{1/2}$ was measured due to the large transfer function. This is already close to the measured intrinsic sensor noise.
These results clearly demonstrate the significance of the approach, as the presented SQUIDs with loop diameter of 10 µm already exhibit white flux noise levels like their state-of-the-art counterparts with loop diameter of about 370 nm [185] based on constriction-type junctions. By further down-scaling the device dimensions, one would expect significant improvements according to relation (2.12), if scaling ratios persist. In addition, this will raise a long standing question, to which values low-frequency noise extends. Furthermore, as the observed low-frequency noise is mainly due to magnetic flux noise it may help to reveal the source of this noise, as discussed in Chapter 5.7.

C SQIF-based dc SQUID amplifier with intrinsic negative feedback

Following the discussion in Chapter 2 the SQUID acts as a flux-to-voltage transducer with a very limited linear working range. To increase this working range, typically a SQUID electronics is used, which measures the voltage across the SQUID, amplifies and integrates this signal and feeds it back as a feedback flux into the SQUID. However, the delay due to signal propagation limits the bandwidth of such systems as well as the maximum system slew rate.
To overcome this limit several on-chip feedback concepts have been introduced [187, 188]. Here, I will briefly describe a two-stage setup comprising a SQUID magnetometer and a SQIF. A detailed description can be found in [36].
The SQIF depicted in the circuit diagram on the left side in Figure A.4 acts as a low-noise cryogenic amplifier, thereby reducing the demands for room-temperature electronics. Compared to the above mentioned concepts based on single SQUIDs or SQUID arrays it features a single working point of the amplifier SQUID. This avoids possible uncertainties due to flux jumps. In addition, the partial feedback of the SQIF's bias

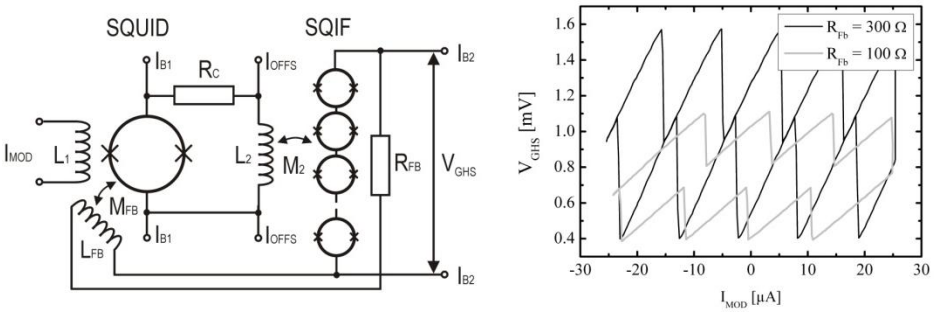

Figure A.4: Left: Schematic of the SQIF-based dc SQUID amplifier measurement setup. Right: Linearized voltage-response due to on-chip feedback for two feedback resistor values R_{Fb}.

current results in an on-chip linearization of the flux-voltage characteristic.
The right side of Figure A.4 shows the linearized voltage response due to a signal flux in the SQUID magnetometer. Each jump in the curve corresponds to exactly $\pm 1\ \Phi_0$. This allows the reconstruction of the input signal and enables the measurement of magnetic fields of practical unlimited dynamic range. In addition, the feedback path is significantly shorter compared to conventional room-temperature SQUID electronics, wherefrom substantial reduction of delay times and hence improvements in system bandwidth and slew rate can be expected.

D Setup for the absolute measurement of the Earth's magnetic field

Due to the periodic flux-voltage characteristic, the voltage across the SQUID in FLL mode corresponds to a set of equidistant flux branches. As a result of unknown point of origin in the external flux SQUIDs can only measure relative changes in flux.
The SQUID-based setup for the absolute measurement of the Earth's magnetic field therefore combines several coplanar SQUIDs integrated on a single chip [35]. The effective areas are arranged step-like to ensure knowledge of the working range of the sensitive SQUIDs by less sensitive reference SQUIDs. This means, that the SQUID with the smallest effective area needs to be chosen according to the desired maximum magnetic field strength to operate as an absolute sensor. In other words, this SQUID in FLL mode remains on the same branch for any amplitude below the desired maximum magnetic field. For a given magnetic field the output voltage of this reference SQUID is used to determine the correct working branch of the SQUID with next smaller effective area. Figure A.5 shows the working principle for a two-stage SQUID cascade [35].

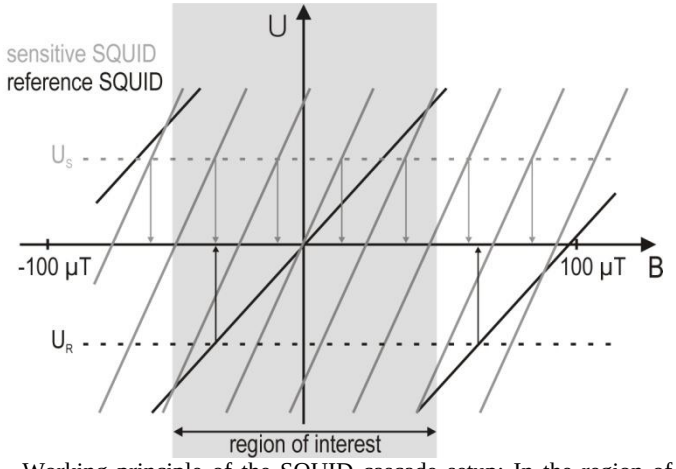

Figure A.5: Working principle of the SQUID cascade setup: In the region of interest, the reference SQUID exhibits a unique operating point. The output voltage of this reference SQUID V_R then indicates the possible working range of the sensitive SQUID, which determines the overall system sensitivity.

Besides the question of point of origin in the external flux, this setup considerably improves the dynamic range of the measurement system, as it separates the information of the measurement data into several channels, which are later-on combined after data acquisition.
In [35] the successful one-dimensional experimental implementation of this approach is presented. As described therein, magnetic fields with amplitudes exceeding 50 µT have been measured with a sensitivity of about 6 $fT/Hz^{1/2}$. The overall dynamic range of the SQUID magnetometer system was 190 dB in this investigation.

E Linear SQUID amplifier – bi-SQUIDs

In Appendix C several concepts based on the on-chip linearization of the flux-voltage characteristics have been introduced. However, their advantages come along with a compromise between linearity and amplitude of the output voltage. This is discussed in detail in [36].
To face this problem, recently a modified dc SQUID capable of providing highly linear intrinsic voltage response was suggested [189]. These so-called bi-SQUIDs, shown in the left hand side of Figure A.6, combine an rf- as well as a dc-SQUID. The nonlinear transformation of the input signal into the Josephson phase difference in the rf SQUID is therein counterbalanced by the nonlinear transformation of the phase difference into the output voltage across the SQUID, which at optimum conditions results in a highly linear triangular-shaped flux-voltage characteristic.
In order to prove the feasibility of this concept, bi-SQUID magnetometer based on cross-type Josephson junctions have been developed [34]. Unlike previously reported experiments [190-192], a rather large SQUID inductance was designed in order to use the bi-SQUID directly as linear magnetometer.
A set of typical measured flux-voltage characteristics of the device is shown on the right

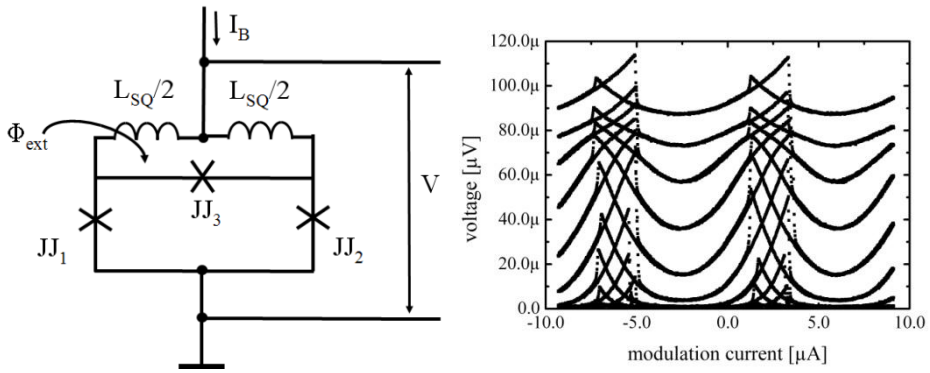

Figure A.6: Left: Bi-SQUID schematics. Together with the SQUID inductance the third Josephson junction JJ_3 forms an rf SQUID, whereas junctions JJ_1 and JJ_2 acting as a dc SQUID. Right: Typical measured flux-voltage characteristics of the fabricated bi-SQUID magnetometer.

side of Figure A.6. Together with the desired triangular flux-voltage characteristics, new features due to the large SQUID inductance appear. They are represented by hysteretic regions at the response tops. Furthermore, smoothing of the flux-voltage response at zero voltage illustrates the influence of noise rounding of the current voltage characteristics. Nevertheless, these first experiments show quite promising results. Investigations regarding an optimized design and the intrinsic noise of these sensors are currently underway.

F Fabrication technology for deep sub-micrometer Josephson junctions

Within the thesis the focus was primarily set on the development of a reliable junction technology offering a high throughput, which favored the used i-line stepper over the electron-beam lithography tool. Here I would like to comment on ongoing work in a further reduction of the junction size towards deep sub-micrometer dimensions by use of e-beam lithography.

The benefits of small area and therefore low capacitance Josephson junctions were already discussed in Chapter 3 together with numerous applications. The question to be raised within this chapter is to what extend the cross-type junction technology can be extended?

As a first step the critical current densities have been increased. For an envisaged junction size of $(350 \times 350)\,\mathrm{nm}^2$ a critical current of 10 µA corresponds to a critical current density of about 8 kA/cm^2, whereas for a $(200 \times 200)\,\mathrm{nm}^2$ Josephson junction a j_C of about 25 kA/cm^2 is required.

Table A.1 shows typically obtained values for cross-type Josephson junctions with increased critical current densities as well as reference values within this technology for a j_C of 1.7 kA/cm^2 used within this thesis. The characteristics have been determined on the base of $(1 \times 1)\,\mu\mathrm{m}^2$ Josephson junctions.

The ratio R_S/R_N of the sub-gap to normal state resistance decreases for increasing critical current densities j_C. Following common assumption reported in the literature, this decrease for large j_C's can be interpreted in the way, that the junction barrier doesn't form a closed oxide layer anymore. It starts to be porous. This results in an increased conduction through quasi-particles and therefore in a decreased sub-gap resistance. It is

Table A.1: Measured specific junction capacitance for two wafers.

Critical current density [kA/cm^2]	R_S/R_N	$V_m = I_C R_S$ [mV]	V_{Gap} [mV]
1.7	≈ 40	≈ 45	≈ 2.8
7.5	10	≈ 15	2.6
15	2.5	≈ 4.5	(2.3 – 2.4)

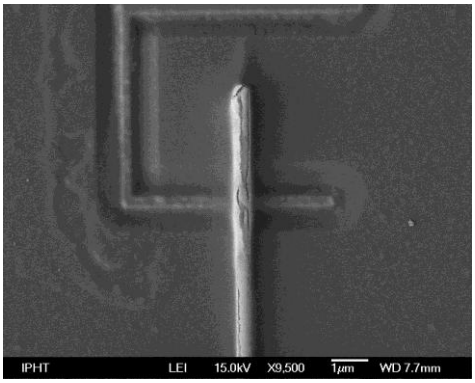

Figure A.7: Scanning electron microscope image of a (250 × 250) nm^2 Josephson junction. The residue next to the vertical line remained from lift-off of the used photo resist.

important to note, that this behavior as well as the decrease of the quality parameter V_m and gap-voltage is consistent with experimental results reported e.g. in [193].

Figure A.7 shows a scanning electron microscope image of a square Josephson junction with (250 × 250) nm^2. The trench around the vertical line, corresponding to the trilayer base electrode, is causes by the shadowing effect during planarization. As pointed out in Chapter 3.2, this can be avoided by an improved planarization processes, as e.g. chemical mechanical polishing (CMP). However, no noticeable detrimental effect due to the trenches has been observed.

One can therefore conclude that Josephson junctions with linear dimensions in the 100 nm range should be feasible within this technology. Accordingly, one can expect further improvements in device performance. However, the decreased quality in the sub-gap region with increasing critical current density may place a limitation especially for low-frequency applications.

Summary

This thesis describes the development of a high sensitive receiver system for transient electromagnetics. As these systems will mostly be used in magnetically unshielded field operation often in very remote areas and even by non-professional personal, a high reliability is essential. Therefore, throughout this thesis special emphasis was given on reproducibility and reliability of the developed fabrication process, the sensors, and all sub-components of the entire system. Not all technical aspects of this development will be described herein.
The intended application imposes very challenging requirements on the receiver system and hence on the SQUID sensors. Accordingly, the magnetic field resolution should be better than 20 $fT/Hz^{1/2}$ in the frequency range between 10 Hz and 20 kHz. At the same time the system should feature a dynamic range larger than ± 2.5 µT. Since there is a worldwide trend towards stronger and faster transmitter for TEM as an active method, the system slew rate emerges as a main figure of merit besides sufficiently low noise. Furthermore, unshielded operation in the Earth's magnetic field with additional applied excitation fields demands for a high field stability of the SQUID sensors.

The thesis starts with a short introduction on geophysical prospection methods and especially the basics of the transient electromagnetics method in Chapter 1. Besides others, the two major advantages of SQUID sensors compared to other magnetometer classes especially induction coils will be discussed: the measurement of the magnetic field rather than its derivative and the achievable very low intrinsic noise. As a result, within this thesis the development of a high sensitive receiver system for transient electromagnetics was focused on SQUID sensors.
Out of basic relations describing fundamental effects as well as the working principle of SQUIDs, in Chapter 2 a realization concept was developed pointing towards small area and low capacitance Josephson junctions. More precisely, as the flux noise scales with the junction capacitance, highly sensitive SQUIDs can be realized with Josephson junctions featuring a low total junction capacitance. According to equation (2.13) this comes along with an increased usable voltage swing of the SQUIDs which in theory enables an increased system slew rate. Furthermore, the use of narrow linewidth structures in combination with a small size of superconducting structures at or around the Josephson junctions is to be favored, as this should lead to an improved field stability of the SQUIDs.
Typical conventional junction fabrication technologies for small area Josephson junctions and their limitations with respect to e.g. minimum achievable junction size or process reliability has therefore been discussed in Chapter 3. These considerations led to the introduction of the new cross-type fabrication technology. Here the total junction capacitance is reduced by downsizing of the junction area into the sub-micrometer range

as well as by avoiding any unnecessary parasitic capacitance in parallel to the junctions, which may limit the performance of superconducting electronic devices. Especially for deep sub-micrometer junction dimensions the parasitic capacitance would otherwise become more pronounced or even dominant. The main advantage of the presented approach lies in the self-definition of the junction area and thus omits any idle region due to the undesired overlap between superconducting electrodes around the junction. Accordingly, the size of the superconductor at or around the Josephson junctions is just the junction dimension. The minimum achievable junction size was limited by the used i-line stepper lithography tool to $(0.6 \times 0.6)\ \mu m^2$. Due to the higher throughput and reduced turn-around times, the i-line stepper was favored over e-beam lithography at this stage of development. Ongoing work towards deep sub-micrometer Josephson junctions is discussed in the Appendix. It may in future improve the performance of the developed devices even further.

Results of the electrical characterization of the fabricated cross-type Josephson junctions were described in Chapter 4. In order to evaluate the performance of the fabrication technology, junction parameters like the $I_C R_N$-product, the quality parameter $I_C R_S$, and especially the ratio of the sub-gap to normal state resistance R_S/R_N are of particular importance. Accordingly, square shaped Josephson junctions with linear dimensions ranging from 10 µm down to 0.6 µm have been characterized. They all feature a high gap-voltage of about 2.8 mV and R_S/R_N-ratios of up to 40. Quality-parameters of about 45 mV independent of the junction size and $I_C R_N$-products up to about 1.7 mV indicate the high quality of the junctions.

In addition, the junction quality was evaluated by Fraunhofer diffraction pattern measurements. It should be pointed out, that in these measurements the critical currents of the investigated junctions reduced to zero, which indicates a homogeneous thickness of the oxide tunnel barrier. In Chapter 4.2 it was furthermore shown, that the measured dependence could be well described by a model representing a symmetric and convex current density distribution over the junction width. The extracted current density profile indicates a decrease of the critical current density at the junction edges, most probably due to damages during the fabrication process. However, even for the smallest fabricated junctions with an area of $(0.6 \times 0.6)\ \mu m^2$ an almost homogeneous region of the critical current density around the center of the junction remains. Consequently, these electrical measurements do not imply a technological limitation for these junction dimensions and the cross-type technology can most likely be extended to even smaller junction sizes.

The total junction capacitance is a main figure of merit in the presented approach. Therefore, the specific junction capacitance was determined by Fiske step measurements to about $62.5\ fF/\mu m^2$ in Chapter 4.3. Hence, for the minimum junction area of $(0.6 \times 0.6)\ \mu m^2$ the junction capacitance amounts to about 20 fF, which is up to a factor of 30 smaller compared to junctions fabricated in the conventional window-type technology.

According to this strong decrease in the total junction capacitance, an improved sensitivity and increased voltage swing is expected, which was estimated in Chapter 5.1. Considering optimum conditions for the energy resolution of the SQUIDs, that is for β_C and β_L about unity, the flux noise density should reduce by a factor of about 2, whereas the voltage swing should increase by more than a factor of 5.

Under the constraints for the intended use in a geophysical receiver system, design criteria for the development of SQUID magnetometer have been discussed in Chapter 5.2. It was shown that multiloop SQUID magnetometers are to be favored in regard to their lower ratio of the SQUID inductance to the magnetometer effective area. Moreover, the reliability of the system as an essential criterion directed towards a single stage SQUID system. Simulations of the device performance based on analytical description of sensor parameters have been carried out in Chapter 5.2, resulting in the multiloop magnetometer named ML2A. SQUIDs of this type have shown typical usable voltage swings of about 170 μV even with moderate McCumber parameter $\beta_C \approx 0.4$.

The low voltage noise of the developed SQUIDs demands a two-stage SQUID setup to determine the intrinsic sensor noise. Accordingly, a white flux noise as low as 0.55 $\mu\Phi_0/\mathrm{Hz}^{1/2}$ was measured for sensors of type ML2A. With an inverse effective area of 5.55 nT/Φ_0 this corresponds to 3 $\mathrm{fT}/\mathrm{Hz}^{1/2}$. It is furthermore worth to note, that the intrinsic energy resolution of these sensors with a SQUID inductance of about 130 pH amounts to 7 h at 4.2 K. Moreover the strongly increased usable voltage swing/ transfer function enables the readout of nearly the intrinsic sensor noise even in a single stage configuration, which may decisively simplify multichannel systems as e.g. in biomagnetism. In a single stage configuration a white flux noise as low as 0.9 $\mu\Phi_0/\mathrm{Hz}^{1/2}$ has been measured, corresponding to about 5 $\mathrm{fT}/\mathrm{Hz}^{1/2}$.

The unshielded field operation imposes special requests on the field stability of the developed sensors. The measured critical field for flux trapping during cool-down of the SQUIDs of type ML2A have shown a $1/w^2$ dependence with w being the linear dimension of the junctions or of the underlying superconductor in case of window type junctions, respectively. The measured data show excellent agreement with theoretical predictions. Tolerable magnetic background fields during cool-down of up to 6.5 mT have been achieved for $(0.6 \times 0.6)\ \mu\mathrm{m}^2$ junctions, which is nearly a factor of 100 larger than for conventional SQUID sensors nowadays. For junction dimensions of $(0.8 \times 0.8)\ \mu\mathrm{m}^2$ used within the SQUID magnetometer applied within the geophysical receiver system the tolerable magnetic background field during cool-down amounts to 3.9 mT.

The application scenario of TEM with an applied magnetic field has raised the question of the stability of these sensors against polarizing magnetic fields during operation. In Chapter 5.5 for polarization fields perpendicular to the chip surface two distinct magnetic field amplitudes have been observed, both scaling as $1/w$ for the investigated junction dimensions with linear dimension w of the junctions. For polarization fields larger about 30 mT in SQUIDs of type ML2A with $(0.8 \times 0.8)\ \mu\mathrm{m}^2$ Josephson junctions the voltage-flux characteristic starts to lag behind the field change after the magnetization pulses, which presumably is caused by creep of flux entering in the vicinity of the Josephson junctions and being expelled later on. For field amplitudes exceeding about 40 mT the voltage-flux characteristic indicates a new stable working point of the SQUIDs due to a change in the junction's critical current caused by frozen flux in or close to the Josephson junctions. For polarization fields in plane of the chip critical fields for vortex trapping of about 76 mT has been determined being independent of the junction dimensions, which to my knowledge is the highest reported value for magnetization fields integrated SQUID sensors could withstand so far without sophisticated screening methods.

Accordingly, these sensors do not only enable the use in measurement systems for transient electromagnetics, but moreover seems to be perfectly suited for e.g. MRI or combined MEG/ MRI systems.

In addition to the described magnetometer of type ML2A a complete family of magnetic field sensors has been developed. They were all designed as multiloop SQUID magnetometer and mainly differ in their pickup loop dimensions, which results in different effective areas depending on the particular application case. With moderate McCumber parameters β_C of about 0.4 they all provide more than 100 µV of usable voltage swing. The most sensitive ones achieve magnetic field noise levels of down to 0.3 fT/Hz$^{1/2}$ and therefore allow addressing even very demanding application fields.

Besides these exceptional low white noise levels the developed SQUID sensors exhibit rather unusual low-frequency noise dependencies. By means of Allan variance, the noise spectra had been divided into several branches, dependent on the dominant scaling of flux noise with frequency. Above about 1 kHz the sensor shows white noise, for $0.2\ \text{Hz} \le f < 1\ \text{kHz}$ main contribution are due to magnetic flux noise scaling as $S_\Phi{}^{1/2} \propto 1/f^{1/4}$ and for $20\ \text{mHz} \le f \le 0.2\ \text{Hz}$ $S_\Phi{}^{1/2} \propto 1/f^{1/2}$, with f being frequency. Below about 20 mHz the system shows random walk characteristics, which may be due to thermal drift in the SQUID electronics.

In the second frequency interval of $0.2\ \text{Hz} \le f < 1\ \text{kHz}$, which is of main importance for the developed sensors, critical current fluctuations had been ruled out as the source of noise by use of an ac-biased flux modulated SQUID electronics. Whereas the noise spectra showed the described slow increase of low-frequency noise for working points with a nonzero transfer function, in working points insensitive to magnetic signals the measured noise remains white in the observed frequency range. Thus it was concluded, that the increase in the low-frequency noise for this branch is caused by a magnetic signal and not by critical current fluctuations from the Josephson junctions.

Further investigations showed that in addition external magnetic fields e.g. due to environmental noise, as well as motion of trapped flux could be ruled out as a source of $1/f$ noise in these devices. According to the presented results, the source of this noise has to be local, that is within the dimension of the device effective areas.

The development of magnetic field sensors with effective areas ranging over several orders of magnitude enabled the investigation of the scaling law of low-frequency flux noise with device dimensions in Chapter 5.7. The low junction capacitance allowed to clearly determine the magnitude of flux noise $S_\Phi{}^{1/2}$ at 1 Hz, as a measure for the low-frequency noise, even at 4.2 K. A clear scaling dependence of $S_\Phi{}^{1/2}$ (1 Hz) with magnetometer effective areas has been observed, which had been interpreted in a model of fluctuating surface spins. Following common assumptions, the observed increase of low-frequency flux noise in SQUIDs as well as in Qubits is attributed to random reversal of spins on the surface of the superconductors. In contrast to previous investigations, which were mainly focused on the temperature dependence of the low-frequency flux noise, the presented results give an explicit quantitative experimental scaling of this noise with device dimensions and may therefore help to confirm current microscopic theories and probably help to reveal the underlying noise mechanism – a long standing question in the investigation of SQUIDs.

The concept and composition of the developed geophysical receiver system was discussed in Chapter 6 and results of the lab-characterization of the system were given. In detail it was shown, that within the system the used SQUID sensors of type ML2A exhibit usable voltage swings of about 160 µV. In the described configuration a 3dB bandwidth of about 5.5 MHz was determined. The choice of feedback resistors resulted in a system dynamic range of $\pm$ 520 Φ_0 and a white magnetic field noise spectral density of 12 fT/Hz$^{1/2}$. The increased noise compared to single stage measurements of the SQUIDs have been discussed in the framework of thermal noise from the feedback resistors, whereby the tradeoff between high dynamic range and low system noise became obvious. Due to the use of a two-pole integrator, the system showed a frequency dependent slew rate, with a maximum of 66 MΦ_0/s at about 25 kHz.
The determination of the low-frequency noise of the entire receiver system showed the influence of the limited low-frequency shielding factor of the used magnetic shielded rooms. Although the measured noise of the system complied with the requirements as stated in Chapter 1, determining especially the low-frequency system performance of highly sensitive SQUID systems may not be possible even in magnetic shielded rooms. Moreover, the determined system performance may not correspond to those in the presence of the Earth's magnetic field. Accordingly, in Chapter 6.3 a characterization method to demonstrate the intrinsic system's noise in an unshielded environment had been introduced together with results obtained on a *multi-purpose* SQUID receiver system.
Finally, results from a ground based TEM field application demonstrated the excellent systems performance and reliability even in remote operation. The excellent performance was documented by an almost noise free behavior even for the last recorded channel with about 1.7 s of the decay curve in the TEM measurements. Already five TEM systems equipped with the sensors developed in this thesis are already in worldwide operation in mineral exploration and for other challenging geophysical objectives.

In the Appendix several adjacent topics, which had been investigated together with my colleagues during the time of my PhD and which are beyond the direct scope of this thesis, have briefly been discussed. Therein it has been shown, that the use of low-capacitance cross-type Josephson junctions not only led to highly sensitive SQUID magnetometer, but e.g. SQUID current sensors with white current sensitivities of down to about 3 fA/Hz$^{1/2}$ have been realized.
Moreover, the use of cross-type Josephson tunnel junctions enables the integration in highly sensitive SQUID magnetometer with very low effective areas. More precisely, the presented SQUIDs with 10 µm loop diameter already showed white flux noise levels comparable to state-of-the-art devices with several hundred nm loop diameter, which nowadays are typically based on constriction-type junctions. A further downscaling may therefore allow addressing several emerging application fields, like e.g. the investigation of small spin systems. Moreover, these devices allow extending the investigation of the scaling of low-frequency magnetic noise to even smaller SQUID loop dimensions and may furthermore provide an interesting tool for the investigation of local magnetic material properties.
Following the discussion in Chapter 6.2, the choice of feedback resistors is driven by the

tradeoff between system noise and dynamic range or slew rate. The investigation of this topic have led to a SQIF-based dc SQUID amplifier with intrinsic negative feedback, which enables an on-chip feedback, wherefrom significant improvements in system bandwidth and slew rate can be expected compared to conventional room-temperature SQUID electronics. Moreover, the presented setup for the absolute measurement of the Earth's magnetic field have led to significant improvement of the dynamic range of the measurement system, amounting to about 190 dB. The implementation of linear SQUID amplifier may help to further strengthen these concepts.

Finally, ongoing work on deep sub-micrometer Josephson junctions may on one hand help to further improve the performance of the developed devices and will probably also affect other parts of superconducting electronics in future.

Samenvatting (Summary in Dutch)

Dit proefschrift beschrijft de ontwikkeling van een zeer gevoelig ontvanger systeem voor de transiënte elektromagnetische methode. Aangezien deze systemen veelal magnetisch onafgeschermd in het veld worden gebruikt in vaak zeer afgelegen gebieden en zelfs door niet-professioneel personeel, is een hoge betrouwbaarheid essentieel. Daarom is in dit proefschrift bijzondere nadruk gelegd op de reproduceerbaarheid en de betrouwbaarheid van het ontwikkelde fabricageproces, de sensoren en alle subcomponenten van het gehele systeem. Niet alle technische aspecten van deze ontwikkeling zullen hierin worden beschreven.

De beoogde toepassing stelt zeer uitdagende eisen aan het ontvanger systeem en daarmee aan de SQUID sensoren. Dienovereenkomstig dient de magneetveld resolutie beter dan 20 $fT/Hz^{1/2}$ in het frequentiegebied tussen 10 Hz en 20 kHz te zijn. Tegelijkertijd moet het systeem over een dynamisch bereik groter dan ± 2.5 μT beschikken. Aangezien er een wereldwijde trend naar sterkere en snellere zender voor TEM als actieve methode is, is er naast een voldoende laag ruisniveau een grote volgsnelheid van het systeem noodzakelijk. Bovendien vraagt onafgeschermd gebruik in het magnetisch veld van de Aarde met extra aangelegde excitatievelden om een hoge veldstabiliteit van de SQUID sensoren.

Het proefschrift begint in hoofdstuk 1 met een korte inleiding over geofysische prospectie methodes en hier hoofdzakelijk de basisprincipes van de transiënte elektromagnetische methode. De twee belangrijkste voordelen van SQUID magnetometer sensoren in vergelijking met andere magnetometertypen, voornamelijk inductiespoelen, worden besproken: het meten van het magnetische veld in plaats van ziin afgeleide en het haalbare zeer lage intrinsieke ruisen. Als gevolg hiervan wordt in dit proefschrift voor de ontwikkeling van een zeer gevoelig ontvangersysteem voor TEM hoofdzakelijk naar de SQUID sensoren gekeken.

Uitgaande van ten grondslag liggende effekten en het werkingsprincipe van SQUIDs, wordt in hoofdstuk 2 een concept voor Josephson juncties met een kleine oppervlakte en een lage capaciteit ontwikkeld. Omdat het fluxruisen lineair afhankelijk is van de junctiecapaciteit, kunnen zeer gevoelige SQUIDs gerealiseerd worden met Josephson juncties met een lage totale junctiecapaciteit. Volgens vergelijking (2.13) gaat dit samen met een verhoogde bruikbare spanningsmodulatie van de SQUIDs die in theorie een grotere systeemvolgsnelheid mogelijk maakt. Bovendien is het gebruik van smalle structuren in combinatie met kleine supergeleidende structuren in de buurt van de Josephson junctions te begunstigen, aangezien dit zou moeten leiden tot een verbeterde veldstabiliteit van de SQUIDs.

Typische conventionele junctie fabricage technologieën voor Josephson juncties met kleine oppervlakte en hun beperkingen met betrekking tot bijvoorbeeld de kleinst haalbare junctie grootte of betrouwbaarheid van het proces is dan ook in hoofdstuk 3 besproken. Deze overwegingen hebben geleid tot de introductie van de nieuwe *cross-type*

fabricage technologie . Hierbij is de totale junctie capaciteit verminderd door verkleining van het contactoppervlak tot submicrometer afmetigen en het vermijden van onnodige parasitaire capaciteiten parallel aan de juncties, die de prestaties van de supergeleidende elektronica kunnen beperken. Vooral voor juncties met afmetingen duidelijk onder 1 µm kan de parasitaire capaciteit anders sterk toenemen of zelfs dominant worden. Het belangrijkste voordeel van de voorgestelde aanpak is de zelfdefinitie van de junctie oppervlakte en daarmee het weglaten van nutteloze gebieden die veroorzaakt worden door de ongewenste overlapping van de supergeleidende elektroden rond de junctie. Dienovereenkomstig is de grootte van de supergeleider op of rond de Josephson junctie gelijk aan de junctie afmetingen. De kleinst bereikbare junctie afmetingen werden door de gebruikte *i-line stepper* lithografie beperkt tot $(0.6 \times 0.6)\ \mu m^2$. Door de hogere verwerkingscapaciteit en kortere verwerkingstijden, werd in deze fase van de ontwikkeling de *i-line stepper* ten opzichte van electronenstraallithografie begunstigd. Lopend onderzoek aan Josephson juncties met afmetingen duidelijk onder 1 µm wordt in de bijlage besproken. In de toekomst zouden hierdoor de prestaties van de ontwikkelde schakelingen nog verder verbeterd kunnen worden.

De elektrische karakterisering van de gefabriceerde *cross-type* Josephson juncties is in hoofdstuk 4 beschreven. Om de fabricagetechnologie te evalueren, zijn junctie parameters zoals het $I_C R_N$-product, de kwaliteitsparameter $I_C R_S$, en vooral de verhouding van de sub-gab en de normale toestand weerstand R_S/R_N van bijzonder belang. Dienovereenkomstig zijn vierkante Josephson juncties met lineaire afmetingen variërend van 10 µrn tot 0.6 µrn gekarakteriseerd. Ze beschikken allemaal over een hoge gap-spanning van ongeveer 2,8 mV en R_S/R_N-verhouding van maximaal 40. Kwaliteit-parameters van ongeveer 45 mV onafhankelijk van de junctie grootte en $I_C R_N$-producten tot ongeveer 1.7 mV duiden op de hoge kwaliteit van de juncties.

De junctie kwaliteit werd bovendien geëvalueerd door metingen van het Fraunhofer diffractie patroon. Het zij opgemerkt dat in deze metingen de kritische stroom van de onderzochte junctie tot nul vermindert, hetgeen op een homogene dikte van de oxide tunnelbarrière wijst. In hoofdstuk 4.2 werd bovendien aangetoond dat de gemeten afhankelijkheid goed kan worden beschreven door een model met een symmetrische en convexe stroomdichtheidsverdeling in de junctie. Het afgeleide stroomdichtheidsprofiel toont een vermindering van de kritische stroomdichtheid aan de junctie randen, waarschijnlijk veroorzaakt door schade tijdens het fabricageproces. Zelfs voor de kleinste vervaardigde juncties met een oppervlak van $(0.6 \times 0.6)\ \mu m^2$ blijft een vrijwel homogene kritische stroomdichtheidsverdeling in het midden van de junctie. Derhalve impliceren deze elektrische metingen geen technologische beperking voor de junctie afmetingen en kan de *cross-type* technologie zeer waarschijnlijk worden ingezet voor nog kleinere junctie afmetingen.

De totale junctie capaciteit is een belangrijke parameter voor de getoonde *cross-type* juncties. In hoofdstuk 4.3 werd de specifieke junctie capaciteit bepaald met behulp van Fiske-stap metingen, wat ongeveer $62.5\ fF/\mu m^2$ opleverde. Hieruit volgt dat voor de kleinste juncties van $(0.6 \times 0.6)\ \mu m^2$ een junctie capaciteit van circa 20 fF. Dit is tot een factor 30 kleiner dan juncties vervaardigd met de gebruikelijke venster technologie.

Uitgaande van deze sterke afname van de totale junctie capaciteit, wordt een verbeterde

gevoeligheid en verhoogde spanningsmodulatie verwacht, en afgeschat in hoofdstuk 5.1. Bij optimale omstandigheden voor de energieresolutie van de SQUIDs, dat wil zeggen β_C en β_L zijn beide ongeveer één, zou de flux ruisdichtheid met een factor van ongeveer 2 af moeten nemen, terwijl de spanningsmodulatie met een factor van meer dan 5 toe zou moeten nemen.

Beperkt door het beoogde gebruik in een geofysisch ontvanger systeem, werden de ontwerpcriteria voor de ontwikkeling van SQUID magnetometers in hoofdstuk 5.2 besproken. Er werd aangetoond dat multiloop SQUID magnetometers begunstigd zijn door hun lagere verhouding van de SQUID inductie tot de effektieve oppervlakte van de magnetometer. Bovendien is de betrouwbaarheid van het systeem als wezenlijk criterium gericht op een eentraps SQUID systeem. Op basis van een analytische beschrijving van de sensor parameters, zijn in hoofdstuk 5.2 simulaties betreffende de werking van de schakeling uitgevoerd, wat in de multiloop magnetometer ML2A resulteerde. SQUIDs van dit type hebben gemetene typische bruikbare spanningsmodulaties van ongeveer 170 μV voor een McCumber parameter β_C van ongeveer 0.4.

Het lage spanningsruisen van de ontwikkelde SQUIDs maakt een tweetraps SQUID setup voor het bepalen van het intrinsieke sensorruisen noodzakelijk. Dienovereenkomstig werd een wit fluxruisniveau van schlechts 0.55 $\mu\Phi_0/Hz^{1/2}$ gemeten voor sensoren van het type ML2A. Dit komt overeen met 3 $fT/Hz^{1/2}$ voor een inverse effectieve oppervlakte van 5.55 nT/Φ_0 voor deze sensoren. Verder is het de moeite waard om op te merken, dat de intrinsieke energieresolutie van deze sensoren met een SQUID inductie van ongeveer 130 pH 7 h bij 4.2 K bedraagt. Bovendien maakt de sterk toegenomen bruikbare spanningsmodulatie/overdrachts functie zelfs het uitlezen van nagenoeg het intrinsieke sensorruisen in een eentraps configuratie mogelijk. Dit kan een beslissende vereenvoudiging voor meerkanaals systemen voor bijvoorbeeld biomagnetisme zijn. In zo'n eentraps configuratie werd een wit fluxruisniveau van 0.9 $\mu\Phi_0/Hz^{1/2}$ gemeten, wat overeenkomt met ongeveer 5 $fT/Hz^{1/2}$.

Onafgeschermde metingen in het veld stellen hoge eisen aan de veldstabiliteit van de ontwikkelde sensoren. De gemeten kritische velden waarbij flux gevangen wordt tijdens het afkoelen van de SQUIDs van het type ML2A volgen een $1/w^2$ afhankelijkheid, waarin w respectievelijk de lineaire afmeting van de juncties of de daaronderliggende supergeleider in het geval van *window type* juncties is. De metingen komen zeer goed overeen met de theoretische voorspellingen. Voor (0.6 x 0.6) μm^2 grote juncties zijn magnetische achtergrondvelden tot 6.5 mT toegestaan tijdens het afkoelen, wat bijna een factor 100 groter is dan voor aktuele conventionele SQUID sensoren. Voor junctie afmetingen van (0.8 × 0.8) μm^2 zoals gebruikt in de SQUID magnetometer voor het geofysische ontvanger systeem bedraagt het toelaatbare magnetische achtergrondveld tijdens het afkoelen 3.9 mT.

De toepassing in TEM met een aangelegd magnetisch veld stelt de stabiliteit van deze sensoren tegen polariserende magnetische velden tijdens hun inzet aan de orde. In hoofdstuk 5.5 zijn voor polarisatie velden loodrecht op het chipoppervlak twee verschillende magnetische veldamplitudes waargenomen, die beide een $1/w$ afhankelijkheid vertonen voor de onderzochte juncties. Voor polarisatie velden groter dan ongeveer 30 mT en SQUIDs van het type ML2A met (0.8 × 0.8) μm^2 grote Josephson

juncties begint de spanning-flux karakteristiek achter te blijven bij de veldverandering na de magnetische puls, wat vermoedelijk wordt veroorzaakt door het bewegen van flux die in de buurt van de Josephson juncties indringt en later verdreven wordt. Voor veldamplitudes groter dan ongeveer 40 mT duidt de spanning-flux karakteristiek op een nieuw stabiel arbeidspunt van de SQUIDs als gevolg van een verandering in kritische stroom van de junctie veroorzaakt door ingevroren flux in of nabij de Josephson juncties. Voor polarisatie velden parallel aan het chipoppervlak zijn onafhankelijk van de junctie afmetingen kritische velden van ongeveer 76 mT voor het indringen van vortices vastgesteld. Dit is voor zover ik weet de hoogste gerapporteerde waarde voor magnetiserende velden die geïntegreerde SQUID sensoren tot nu toe konden doorstaan zonder geavanceerde screeningsmethoden toe te passen.

Behalve de beschreven magnetometer ML2A werd een complete serie magneetveldsensoren ontwikkeld. Ze zijn allemaal als *multiloop* SQUID magnetometer ontworpen en verschillen hoofdzakelijk in hun *pickup loop* afmetingen, waardoor SQUIDs met verschillende effectieve oppervaktes voor verschillende specifieke toepassingen ontstaan zijn. Alle SQUIDs hebben meer dan 100 µV spanningsmodulatie voor een McCumber parameters β_C van ongeveer 0.4. De gevoeligste bereiken een magneetveldruisen van 0.3 fT/Hz$^{1/2}$ wat het gebruik in zeer veeleisende toepassingen mogelijk maakt.

Naast deze uitzonderlijk lage witte ruisniveaus vertonen de ontwikkelde SQUID sensoren nogal ongewone ruisspectra bij lage frequnties. Door meting van de Allan variantie werden de ruisspectra in verschillende gebieden verdeeld, afhankelijk van de afhankelijkheid van de fluxruis van de frequentie f. Boven ongeveer 1 kHz vertoont de sensor witte ruis, voor 0.2 Hz $\leq f <$ 1 kHz is de belangrijkste bijdrage toe te schrijven aan magnetische fluxruis $S_\Phi^{1/2} \propto 1/f^{1/4}$ en voor 20 mHz $\leq f \leq$ 0.2 Hz $S_\Phi^{1/2} \propto 1/f^{1/2}$. Onder ongeveer 20 mHz vertoont het systeem toevallige veranderingen, eventueel als gevolg van thermische drift in de SQUID elektronica.

In het voor de ontwikkelde sensoren van groot belang zijnde tweede frequentie-interval van 0.2 Hz tot 1 kHz, werden met behulp van een *ac-biased* flux gemoduleerde SQUID elektronica schommelingen in de kritische stroom als ruisbron uitgesloten. Terwijl voor arbeidspunten met een overdrachtsfunctie ongelijk aan nul de ruisspectra de beschreven langzame toename bij lage frequenties toonden, bleven voor arbeidspunten die ongevoelig voor magnetische signalen zijn, de ruisspectra wit in het gemetene frequentiebereik. Hieruit volgt dat de toename van het laagfrequente ruisen in dit frequentiegebied wordt veroorzaakt door een magnetische signaal en niet door kritische stroom schommelingen van de Josephson juncties.

Verder onderzoek toonde aan dat externe magnetische velden, veroorzaakt door bijvoorbeeld omgevingsruis, evenals de beweging van de ingevroren flux kan worden uitgesloten als bron van 1/*f* ruis in deze sensoren. Uit de gepresenteerde resultaten volgt dat de ruisbron lokaal moet zijn, dat wil zeggen uit een gebied overeenkomend met de effektieve oppervlakte van de SQUID.

De ontwikkeling van magneetveld sensoren met effectieve oppervlaktes die enkele ordes van grootte varieren maakte het mogelijk de het laagfrequente ruisen afhankelijk van de SQUID afmetingen te bepalen en is beschreven in hoofdstuk 5.7. De lage

junctiecapaciteit maakte het mogelijk de het fluxruisniveau $S_\Phi^{1/2}$ bij 1 Hz als maat voor de laagfrequente ruis te bepalen, zelfs bij 4.2 K. Er werd een duidelijke afhankelijkheid van $S_\Phi^{1/2}$ (1 Hz) van de effektieve oppervlakte van de magnetometer gemeten, wat geïnterpreteerd is met een model voor fluctuerende oppervlakte spins. De waargenomen toename van de laagfrequente fluxruis in SQUIDs en in Qubits wordt over het algemeen toegeschreven aan de willekeurige omkering van de spins aan het oppervlak van de supergeleiders. In tegenstelling tot eerdere onderzoeken, die vooral waren gericht op de temperatuurafhankelijkheid van het laagfrequente fluxruisen, geven de gepresenteerde resultaten een expliciete kwantitatieve experimentele afhankelijkheid van dit ruisen van de *device* afmetingen. Dit kan behulpzaam zijn huidige microscopische theorieën te bevestigen en wellicht helpen om het ten grondslag liggende ruismechanisme te onthullen - een lang bestaande vraag in het onderzoek aan SQUIDs.

Het concept en de samenstelling van het ontwikkelde geofysische ontvangersysteem en zijn karakterisatie in het laboratorium werden besproken in hoofdstuk 6. De in het systeem ingebouwde SQUID sensoren van het type ML2A tonen een spanningsmodulatie van ongeveer 160 µV. De 3dB bandbreedte is ongeveer 5.5 MHz voor de beschreven configuratie. Door de keuze van de feedback weerstanden bedraagt het dynamische bereik van het systeem $\pm 520\,\Phi_0$ en de spectrale witte magnetische veldruisdichtheid 12 fT/Hz$^{1/2}$. De ten opzichte van eentraps metingen toegenomen ruisnivaus van de SQUIDs werden met behulp van het thermische ruisen van de *feedback* weerstanden beschreven. Hierbij werd de afweging tussen een hoog dynamisch bereik en laag systeemruisen duidelijk. Door het gebruik van een twee-polige integrator, vertoonde het systeem een frequentieafhankelijke stijgsnelheid van maximaal 66 MΦ_0/s bij ongeveer 25 kHz.

Bij de bepaling van het laagfrequente ruisen van het complete ontvangersysteem werd de invloed van de beperkte laagfrequente afschermingsfactor van de gebruikte magnetisch afgeschermde ruimtes duidelijk. Hoewel het gemeten systeem ruisniveau voldoet aan de eisen zoals gesteld in hoofdstuk 1, is het bepalen van vooral de prestaties bij lage frequenties van zeer gevoelige SQUID systemen zelfs in magnetisch afgeschermde ruimtes niet mogelijk. Bovendien kunnen de zo bepaalde systeemprestaties afwijken van die in de aanwezigheid van het magnetisch veld van de aarde. Dienovereenkomstig werd in hoofdstuk 6.3 een karakteriseringsmethode ter bepaling van het intrinsieke ruisen van het systeem in onafgeschermde omgeving geintroduceerd samen met de bijbehorende metingen zoals verkregen met een multi-purpose SQUID-ontvanger systeem.

Tot slotte worden de uitstekende systeemprestaties van een op de grond geinstalleerd TEM systeem, zelfs wanneer deze op afstand bediend wordt, besproken. De uitmuntende prestaties werden duidelijk door een vrijwel ruisvrij gedrag voor zelfs het laatst opgenomen kanaal ongeveer 1.7 s na het uitschakelen van de TEM-puls. Vijf TEM-systemen die zijn uitgerust met de sensoren die in dit proefschrift ontwikkeld werden, worden al wereldwijd bij de exploratie van mineralen en bij andere uitdagende geofysische doelstellingen ingezet.

In de bijlage worden een aantal onderwerpen, die tijdens mijn promotie samen met mijn collega's werden onderzocht maar niet direct met het thema van dit proefschrift te maken hebben, kort besproken. Er werd aangetoond, dat het gebruik van lage-capaciteit *cross-*

type Josephson juncties niet alleen leidde tot zeer gevoelige SQUID magnetometer, maar hiermee bijvoorbeeld ook SQUID stroomsensoren met stroomgevoeligheden tot ongeveer 3 $fA/Hz^{1/2}$ (witte ruis) mogelijk zijn.

Bovendien maken *cross-type* Josephson tunneljuncties zeer gevoelige SQUID magnetometer met uiterst kleine effectieve oppervlaktes mogelijk. Zulke SQUIDs met 10 µm ringdiameter vertonen een wit fluxruisniveau dat vergelijkbaar is met *state-of-the-art* SQUIDs met ringdiameters van enkele honderd nm, zoals die tegenwoordig gewoonlijk met constrictie-juncties gemaakt worden. Een verdere verkleining kan voor verschillende opkomende toepassingen, zoals bijvoorbeeld het onderzoek aan kleine spinsystemen, van belang zijn. Bovendien kunnen deze SQUIDs voor het bepalen van de afhankelijkheid van de laagfrequente ruis van zeer kleine ringdiameters of het meten van lokale magnetische materiaaleigenschappen ingezet worden.

Zoals in hoofdstuk 6.2 besproken werd, bepaalt de afweging tussen systeemruis en dynamisch bereik of stijgsnelheid de keuze van de *feedback* weerstanden.. Onderzoek op dit gebied leidde tot een op een SQIF gebaseerde dc SQUID versterker met intrinsieke negatieve terugkoppeling, wat een *on-chip* terugkoppeling mogelijk maakt. Hiermee zijn aanzienlijke verbeteringen in de systeembandbreedte en de stijgsnelheid mogelijk in vergelijking met conventionele SQUID elektronica bij kamertemperatuur. Bovendien kon met behulp van de gepresenteerde *setup* voor de absolute meting van het magnetisch veld van de aarde, het dynamische bereik van het systeem aanzienlijk verbeterd worden tot ongeveer 190 dB. Door gebruik te maken van lineaire SQUID versterkers zouden deze concepten verder verbeterd kunnen worden.

Tot slotte kunnen de lopende werkzaamheden aan submicrometer Josephson juncties enerzijds helpen bij het verder verbeteren van de ontwikkelde *devices* en anderzijds in de toekomst waarschijnlijk invloed hebben op andere delen van supergeleidende elektronica.

Acknowledgements

This thesis would not have been possible without the assistance of numerous people. During this time they do not only gave me scientific and technical support, but moreover social support, for which I would like to sincerely thank them.
First of all, I would like to mention my supervisors Prof. Dr. Horst Rogalla and Prof. Dr. Hans-Georg Meyer for giving me the opportunity to write my PhD thesis at the University of Twente while working at IPHT in Jena and to present the results of my scientific work at various conferences. Furthermore, enabling the participation in many field trials gave me the opportunity to see scientific questions in addition from a totally different and highly beneficial point of view.
Special thanks go to Ronny and Slava, my daily scientific advisors at IPHT. I highly appreciate their trust, patience and support during my work and I would also like to thank them for endless proofreading of the manuscript. Especially I would like to emphasize Slava's russian style to solve hopeless seeming problems. That really impressed my very much and I don't want to miss this time. I hope that we can all solve plenty of problems together in future.
Furthermore, I would like to thank my colleagues Thomas, Michael and Andreas for many interesting discussions and their helping hand when Matlab didn't do what it should. It was a very pleasant and fruitful time with you. I would like to thank Torsten for meeting the endless demands on the measurement software, Kolja for his help with the slew rate simulations and Rob for translating the summary of the thesis and being a Twente insider.
Special thanks go as well to my colleagues doing all the work in the clean-room: Solveig, Ludwig, Sven, Steini and Katrin as well as the entire group behind them. As I used to say, Ich wünsche euch alle Zeit gute Kontakte! Thank you also Jürgen and Hermann for your efforts to promptly provide the photo masks. Moreover, Heike and Marion provided numerous bonding wires and organized the helium for the measurements.
I would like to thank the whole group of Quantum Detection at IPHT for the pleasant time I could join with you.

During my PhD I've also worked together with researchers from other groups. The most important for me was the work with Michael Mück. Thank you for giving me a deeper understanding in the low-frequency noise and measurement methods.
Thanks go as well to Prof. Victor Kornev and his colleagues Igor and Alexey for the joint development of the bi-SQUIDs in the cross-type technology and the interesting insights we gained. Hopefully we can continue our work together.
Special thanks go to Yasunori Matsui from the group of Prof. Itozaki from Osaka University. During his stay at IPHT he worked with such diligence and conscientiousness and I highly appreciate to join this time with him.

I would also like to thank Prof. Paul Seidel and the Department of Low Temperature Physics of the Friedrich-Schiller University Jena for the allocation of the superconducting magnet measurement setup and Thomas Schurig from the PTB Berlin for giving us a chance to perform noise measurements in the BMSR.
Moreover, I would like to thank Jaco Smit very much for providing the excellent data for the TEM field test, which is of vital importance to demonstrate the performance of the entire measurement system in the field.
Special thanks go as well to Ans and Inke for their help with the paperwork especially in the final stage of the thesis. Thank you for your always kind and straightforward helps.

Finally, I want to thank my family and especially my wife Linda and my son Richard. Thank you for always being there for me. I would not be where I am, or who I am today without you.

List of Publications

1. S. Anders, M. Schmelz, L. Fritzsch, R. Stolz, V. Zakosarenko, T. Schönau and H.-G. Meyer, "Sub-micrometer-sized, cross-type Nb-AlOx-Nb tunnel junctions with low parasitic capacitance", *Supercond. Sci. Technol.* **22**, 064012, (2009).
2. M. Schmelz, R. Stolz, V. Zakosarenko, S. Anders, L. Fritzsch, M. Schubert and H.-G. Meyer, "SQUIDs based on submicrometer-sized Josephson tunnel junctions fabricated in a cross-type technology ", *Supercond. Sci. Technol.* **24** 015005, (2011).
3. M. Schmelz, R. Stolz, V. Zakosarenko, T. Schönau, S. Anders, L. Fritzsch, M. Mück, H.-G. Meyer, "Field-stable SQUID magnetometer with sub-fT/Hz$^{1/2}$ resolution based on sub-micrometer cross-type Josephson tunnel junctions", *Supercond. Sci. Technol.* **24** 065009, (2011).
4. A. Chwala, R. Stolz, V. Zakosarenko, M. Schmelz, L. Fritzsch, F. Bauer, M. Starkloff, J.P. Smit and H.-G. Meyer, "Low temperature SQUID magnetometer system for geophysical exploration with transient electromagnetics", *Supercond. Sci. Technol.* **24** 125006, (2011).
5. T. Schönau, M. Schmelz, V. Zakosarenko, R. Stolz, S. Anders, L. Fritzsch and H.-G. Meyer, "SQIF-based dc SQUID amplifier with intrinsic negative feedback", *Supercond. Sci. Technol.* **25** 015005, (2012).
6. A. Sharafiev, I. Soloviev, V. Kornev, M. Schmelz, R. Stolz, V. Zakosarenko, S. Anders and H.-G. Meyer, "Bi-SQUIDs with sub-micron cross-type Josephson tunnel junctions", *Supercond. Sci. Technol.* **25** 045001, (2012).
7. M. Schmelz, R. Stolz, V. Zakosarenko, S. Anders, L. Fritzsch, H. Roth and H.-G. Meyer, "Highly sensitive miniature SQUID magnetometer fabricated with cross-type Josephson tunnel junctions", *Physica C* **478** 77-80, (2012).
8. V. Zakosarenko, M. Schmelz, R. Stolz, T. Schönau, L. Fritzsch, S. Anders and H.-G. Meyer, "Femtoammeter on the base of SQUID with thin-film flux transformer", *Supercond. Sci. Technol.* **25** 095014, (2012).
9. M. Schmelz, R. Stolz, V. Zakosarenko, T. Schönau, S. Anders, L. Fritzsch, M. Mück, M. Meyer and H-G Meyer, "Sub-fT/Hz$^{1/2}$ resolution and field-stable SQUID magnetometer based on low parasitic capacitance sub-micrometer cross-type Josephson tunnel junctions", *Physica C* **482** 27-32, (2012).
10. Y. Zhang, C. Liu, M. Schmelz, H.-J. Krause, A. I. Braginski, R. Stolz, X. Xie, H.-G. Meyer, A. Offenhäusser, and M. Jiang, "Planar SQUID Magnetometer integrated with Bootstrap Circuits under Different Bias Modes", *Supercond. Sci. Technol.* **25** 125007, (2012).
11. T. Schönau, M. Schmelz, V. Zakosarenko, R. Stolz, M. Meyer, S. Anders, L. Fritzsch and H.-G. Meyer, "SQUID-based setup for the absolute measurement of the Earth's magnetic field", *Supercond. Sci. Technol.* **26** 035013, (2013).

12. A. Chwala, J. Kingman, R. Stolz, M. Schmelz, V. Zakosarenko, S. Linzen, F. Bauer, M. Starkloff M. Meyer and H.-G. Meyer, "Noise characterization of highly sensitive SQUID magnetometer system in unshielded environments", *Supercond. Sci. Technol.* **26** 035017, (2013).
13. T. Schönau, M. Schneider, M. Schiffler, M. Schmelz, R. Stolz, and H.-G. Meyer, "Removal of step-edges and corresponding Gibbs ringing in SQUID-based geomagnetic data", *Meas. Sci. Technol.* **24** 125004, (2013).

Submitted/ to be submitted

14. M. Schmelz, V. Zakosarenko, R. Stolz, T. Schönau, S. Anders, L. Fritzsch, S. Linzen, and H.-G. Meyer
    "Effective area dependence of low-frequency magnetic flux noise in dc SQUID magnetometer at 4.2 K"
15. S. Anders, M. Schmelz, R. Stolz, V. Zakosarenko, and H.-G. Meyer
    "Deep submicron cross-type Josephson tunnel junctions"

List of Abbreviations

a	radius of a circular transmitter loop [m]
a_0	side length of the Josephson junction [µm]
A	magnetic vector potential [Vs/m]
A_{eff}	effective area of the magnetometer [mm^2]
A_{JJ}	area of the Josephson junction [μm^2]
B	magnetic flux density [T]
β_C	McCumber parameter
β_L	screening parameter of a dc-SQUID
$\beta_{L,eff}$	effective screening parameter
c_0	light velocity in vacuum = $2.998 \cdot 10^{-8}$ m/s
c_S	specific junction capacitance [$fF/\mu m^2$]
C_{JJ}	total junction capacitance [fF]
$C_{JJ,p}$	parasitic capacitance in parallel to the junction capacitance due to the overlap of wiring layers [fF]
d_p	inner pickup coil dimension [mm]
d_s	slit width between spokes in multiloop magnetometer [µm]
D_p	outer pickup coil dimension [mm]
DR	dynamic range of SQUID receiver system
δ	skin depth of an electromagnetic wave
e	elementary charge = $1.602 \cdot 10^{-19}$ C
E_J	Josephson coupling energy
ε	energy resolution [h]
ε_0	vacuum permittivity = $8.854 \cdot 10^{-12}$ F/m
ε_C	coupled energy resolution of a SQUID [h]
ε_r	relative permittivity
f	frequency [Hz]
f_{3dB}	small-signal bandwidth of the FLL
f_{GBP}	gain-bandwidth product of amplifier
f_J	Josephson frequency = 483.6 MHz/µV·V_{DC}
F	area penetrated by the magnetic flux [mm^2]
ϕ	phase of superconducting wave function
φ	phase difference across a Josephson junction
$\delta\Phi$	linear flux range

Φ	magnetic flux [Wb]
Φ_0	magnetic flux quantum = $2.068 \cdot 10^{-15}$ Wb
Φ_{ext}	external applied magnetic flux [Wb]
Φ_{Fb}	feedback flux in the SQUID
Φ_{lin}	linear flux working range [Wb]
Φ_{Sig}	signal flux applied to the SQUID
Φ_{max}	slew rate of the FLL [MΦ_0/s]
Γ	noise parameter
H	Planck's constant = $6.626 \cdot 10^{-34}$ Js
$\hbar$	reduced Planck's constant = h/2π = $1.055 \cdot 10^{-34}$ Js
H_C	critical field of a superconductor [A/m]
I	current [A]
I_B	bias current of a SQUID [µA]
I_C	critical current of a Josephson junction [µA]
$I_{C,0}$	maximum critical current of a Josephson junction [µA]
I_{C1}, I_{C2}	critical currents of the two junctions in the SQUID loop [µA]
I_{Gap}	current at the gap of an SIS Josephson junction [µA]
j_C	critical current density of a Josephson junction [A/cm^2]
J_C	critical current density of a superconductor [A/cm^2]
J_{circ}	circulating screening current in the SQUID loop
k_B	Boltzmann's constant = $1.381 \cdot 10^{-23}$ J/K
l	noise source correlation length [µm]
l	closed path inside a superconductor
L_{in}	inductance of input coil [pH]
L_{SQ}	SQUID inductance [pH]
λ_J	Josephson penetration depth [µm]
λ_L	London penetration depth [nm]
m	magnetic dipole
m_S	mass of superconducting charge carries
M_{dyn}	current sensitivity of the SQUID [Φ_0/µA]
M_{Fb}	mutual inductance between SQUID and feedback coil [pH]
M_{in}	mutual inductance between SQUID and input coil [pH]
μ_0	vacuum permeability = $4\pi \cdot 10^{-7}$ H/m
μ_B	Bohr magneton = $9.274 \cdot 10^{-24}$ J/T
n_S	Cooper pair density [cm^{-3}]
N	number of parallel loops in multiloop magnetometer
R_{dyn}	dynamic resistance of a SQUID in a working point [Ω]
R_D	damping resistor in parallel to SQUID inductance [Ω]
R_{Fb}	feedback resistor in FLL [Ω]

R_{JJ}	junction resistance, parallel connection of R_N and R_{Sh} [Ω]
R_N	normal state resistance of a Josephson junction [Ω]
R_S	subgap resistance of a Josephson junction [Ω]
R_{Sh}	shunt resistance of a Josephson junction [Ω]
S_B	magnetic field noise spectral density [fT^2/Hz]
$S_I^{1/2}$	equivalent input current noise of SQUID [$pA/Hz^{1/2}$]
S_{I0}	power spectral density of critical current noise [pA^2/Hz]
$S_{I,Amp}^{1/2}$	effective preamplifier input current noise [$pA/Hz^{1/2}$]
$S_{V,Amp}^{1/2}$	effective preamplifier input voltage noise [$nV/Hz^{1/2}$]
S_Φ	power spectral density of SQUID flux noise [Φ_0^2/Hz]
$S_{\Phi,t}^{1/2}$	total measured flux noise of SQUID and electronics [$\Phi_0/Hz^{1/2}$]
$S_{\Phi,SQ}^{1/2}$	intrinsic flux noise of the SQUID [$\Phi_0/Hz^{1/2}$]
σ	electrical conductivity of the soil [Ωm]
t	time [s]
t_i	time stamps in TEM response
t_{ox}	thickness of tunnel oxide barrier in a Josephson junction [nm]
T	temperature [K]
T_C	critical temperature of a superconductor [K]
τ	cluster time for calculation of Allan standard deviation [s]
V	voltage [V]
V_F	Voltage of Fiske steps [μV]
V_Φ	transfer function of the SQUID [$\mu V/\Phi_0$]
V_{Gap}	gap voltage of a Josephson junction [mV]
V_m	quality parameter of a Josephson junction [mV]
δV	usable voltage swing of the SQUID [μV]
w	width of a superconducting structure [μm]
ω_J	angular frequency of alternating current = $2\pi f_J$
w_p	linewidth of superconducting pickup coil [μm]
w_s	linewidth of spokes in multiloop magnetometer [μm]
W_1, W_2	working points
ξ	coherence length [nm]
Ψ	superconducting wave function

References

1. G. Agricola, *De re metallica*. 1556.
2. M.N. Nabighian, *Electromagnetic Methods in Applied Geophysics: Application/Parts A and B*. Society of Exploration Geophysicists, 1988.
3. W.W.M. Telford, L.P. Geldart and R.E. Sheriff, *Applied Geophysics*. Cambridge University Press, 1990.
4. P. Kearey, M. Brooks and I. Hill, *An Introduction to Geophysical Exploration*. Wiley, 2013.
5. H. Brasse, *Lecture notes on "Methoden der geoelektrischen und elektromagnetischen Tiefenerkundung"*. 2003, Department Geophysic, FU Berlin.
6. G. J. Palacky, *Chapter 3: Resistivity characteristics of geologic targets*, in *Electromagnetic Methods in Applied Geophysics: Voume 1, Theory*, Editor M.N. Nabighian. Society of Exploration Geophysicists. p. 52-129, 1988.
7. M.N. Nabighian, *Chapter 6: Time Domain Electromagnetic prospecting methods*, in *Electromagnetic Methods in Applied Geophysics: Volume 2, Application/Parts A and B*, Editor M. Nabighian. Society of Exploration Geophysicists. p. 427-520, 1988.
8. M. Nabighian, "Quasi-static transient response of a conducting half-space - An approximate representation", *Geophysics*, vol. **44** (10), p. 1700-1705, (1979).
9. M. W. Asten and A. C. Duncan, "The quantitative advantages of using B-field sensors in time-domain EM measurement for mineral exploration and unexploded ordnance search", *Geophysics*, vol. **77** (4), p. WB137-WB148, (2012).
10. B. Spies, "Depth of investigation in electromagnetic sounding methods", *Geophysics*, vol. **54** (7), p. 872-888, (1989).
11. C. Le Roux and J. Macnae, "SQUID sensors for EM systems", *Proceedings of Exploration 07: Fifth Decennial International Conference on Mineral Exploration*, p. 417-423, (2007).
12. M. N. Nabighian and J. C. Macnae, "Electrical and EM methods, 1980–2005", *The Leading Edge*, vol. **24** (Supplement), p. S42-S45, (2005).
13. Geonics Limited. *Geonics Limited ProTEM receiver*. 2013; http://www.geonics.com/.
14. Zonge International. *Zonge International Receivers*. 2013; http://zonge.com/instruments-home/equipment/receivers/.
15. Crone Geophysics & Exploration Ltd. *Crone Geophysics Receiver CDR2*. 2013; http://www.cronegeophysics.com/index.html.
16. J. Macnae, "Developments in Broadband Airborne Electromagnetics in the Past Decade", *Proceedings of Exploration 07: Fifth Decennial International Conference on Mineral Exploration*, p. 387-398, (2007).

17. S. Thomson, D. Fountain and T. Watts, "Airborne Geophysics – Evolution and Revolution", *Proceedings of Exploration 07: Fifth Decennial International Conference on Mineral Exploration*, p. 19-37, (2007).
18. Spectrem Air Ltd. *Spectrem 2000*. 2013; http://www.spectrem.co.za/spectrem2000.
19. Fugro Airborne Surveys. *GEOTEM - Fugro Airborne Surveys*. 2013; http://www.fugroairborne.com/services/geophysicalservices/bysurvey/electromagnetics/fixed-wing-electromagnetic/geotem.
20. Fugro Airborne Surveys. *MEGATEM - Fugro Airborne Surveys*. 2013; http://www.fugroairborne.com/services/geophysicalservices/bysurvey/electromagnetics/fixed-wing-electromagnetic/megatem.
21. Aeroquest Airborne. *AeroTEM - Aeroquest Airborne*. 2013; http://www.aeroquestairborne.com/AeroTEM.
22. Geotech Ltd. *VTEM - Geotech Airborne Geophysical Surveys and Exploration*. 2013; http://www.geotech.ca/vtem.
23. Fugro Airborne Surveys. *HeliGEOTEM - Helicopter Time-Domain Electromagnetics*. 2013; http://www.fugrowaterservices.com/downloads/mapping/ChoppTimeDomEM.pdf.
24. J. Zimmerman and W. Campbell, "Tests of cryogenic SQUID for geomagnetic field measurements", *Geophysics*, vol. **40** (2), p. 269-284, (1975).
25. T. Gamble, W. Goubau and J. Clarke, "Magnetotellurics with a remote magnetic reference", *Geophysics*, vol. **44** (1), p. 53-68, (1979).
26. S. G. Wang, L. H. Zhang, C. J. Wang and Y. D. Dai, "Application of high temperature superconducting quantum interference devices in transient electromagnetic method for magnetotelluric soundings", *Physica C: Superconductivity*, vol. **282–287, Part 1** (0), p. 411-414, (1997).
27. M. Bick, G. Panaitov, N. Wolters, Y. Zhang, H. Bousack, A. I. Braginski, U. Kalberkamp, H. Burkhardt and U. Matzander, "A HTS rf SQUID vector magnetometer for geophysical exploration", *IEEE Transactions on Applied Superconductivity*, vol. **9** (2), p. 3780-3785, (1999).
28. A. Chwala, R. Stolz, J. Ramos, V. Schultze, H. G. Meyer and D. Kretzschmar, "An HTS dc SQUID system for geomagnetic prospection", *Superconductor Science and Technology*, vol. **12** (11), p. 1036, (1999).
29. J. B. Lee, D. L. Dart, R. J. Turner, M. A. Downey, A. Maddeyer, G. Panjkovic, C. P. Foley, K. E. Leslie, R. Binks, C. Lewis, and W. Murray, "Airborne TEM surveying with a SQUID magnetometer sensor", *Geophysics*, vol. **67** (2), p. 468-477, (2002).
30. K. E. Leslie, R. A. Binks, C. P. Foley, R. G. Thorn, M. J. Roberts, J. Du, E. E. Mitchell, S. K. H. Lam, C. J. Lewis, C. Millar, and R. T. Osmond, "Operation of a geophysical HTS SQUID system in sub-Arctic environments", *IEEE Transactions on Applied Superconductivity*, vol. **13** (2), p. 759-762, (2003).
31. S. Anders, M. Schmelz, R. Stolz and H. G. Meyer, *unpublished results on: Deep submicron cross-type Josephson tunnel junctions*. 2013.
32. V. Zakosarenko, M. Schmelz, R. Stolz, T. Schönau, L. Fritzsch, S. Anders and H. G. Meyer, "Femtoammeter on the base of SQUID with thin-film flux transformer", *Superconductor Science and Technology*, vol. **25** (9), p. 095014, (2012).

33. M. Schmelz, R. Stolz, V. Zakosarenko, S. Anders, L. Fritzsch, H. Roth and H. G. Meyer, "Highly sensitive miniature SQUID magnetometer fabricated with cross-type Josephson tunnel junctions", *Physica C: Superconductivity*, vol. **476**, p. 77-80, (2012).
34. A. Sharafiev, I. Soloviev, V. Kornev, M. Schmelz, R. Stolz, V. Zakosarenko, S. Anders and H. G. Meyer, "Bi-SQUIDs with submicron cross-type Josephson tunnel junctions", *Superconductor Science and Technology*, vol. **25** (4), p. 045001, (2012).
35. T. Schönau, M. Schmelz, V. Zakosarenko, R. Stolz, M. Meyer, S. Anders, L. Fritzsch and H. G. Meyer, "SQUID-based setup for the absolute measurement of the Earth's magnetic field", *Superconductor Science and Technology*, vol. **26** (3), p. 035013, (2013).
36. T. Schönau, M. Schmelz, V. Zakosarenko, R. Stolz, S. Anders, L. Fritzsch and H. G. Meyer, "SQIF-based dc SQUID amplifier with intrinsic negative feedback", *Superconductor Science and Technology*, vol. **25** (1), p. 015005, (2012).
37. T. Van Duzer and C.W. Turner, *Principles of superconductive devices and circuits*. Elsevier, 1981.
38. K.K. Likharev, *Dynamics of Josephson Junctions and Circuits*. Gordon and Breach Science Publishers, 1986.
39. M. Tinkham, *Introduction to Superconductivity*. Dover Publications, 1996.
40. J. Clarke and A.I. Braginski, *The SQUID Handbook: Fundamentals and Technology of SQUIDs and SQUID Systems*. Wiley-VCH, 2006.
41. W. Buckel and R. Kleiner, *Superconductivity*. Wiley-VCH, 2008.
42. H. K. Onnes, "Further experiments with liquid helium. C. On the change of electric resistance of pure metals at very low temperatures etc. IV. The resistance of pure mercury at helium temperatures.", *Proceedings of the Koninklijke Nederlandse Akademie Van Wetenschappen*, vol. **13**, p. 1274-1276, (1911).
43. H. K. Onnes, "Further experiments with liquid helium. D. On the change of the electrical resistance of pure metals at very low temperatures, etc. V. The disappearance of the resistance of mercury.", *Proceedings of the Koninklijke Nederlandse Akademie Van Wetenschappen*, vol. **14**, p. 113-115, (1911).
44. B. D. Josephson, "Possible new effects in superconductive tunneling", *Physics Letters*, vol. **1** (7), p. 251-253, (1962).
45. R. Pöpel, "The Josephson Effect and Voltage Standards", *Metrologia*, vol. **29** (2), p. 153-174, (1992).
46. E. Fang and T. Van Duzer, "A Josephson integrated circuit simulator JSIM for superconductive electronics application", *Extended Abstracts of 1989 Int. Superconductive Electronics Conference*, p. 407-410, (1989).
47. J. Satchell, "Stochastic simulation of SFQ logic", *IEEE Transactions on Applied Superconductivity*, vol. **7** (2), p. 3315-3318, (1997).
48. D. E. McCumber, "Effect of ac Impedance on dc Voltage-Current Characteristics of Superconductor Weak-Link Junctions", *Journal of Applied Physics*, vol. **39** (7), p. 3113-3118, (1968).
49. W. C. Stewart, "Current-voltage characteristics of Josephson junctions", *Applied Physics Letters*, vol. **12** (8), p. 277-280, (1968).
50. J. Matisoo, "Subnanosecond pair-tunneling to single-particle tunneling transitions in Josephson junctions", *Applied Physics Letters*, vol. **9** (4), p. 167-168, (1966).

51. K. K. Likharev, "Superconductor digital electronics", *Physica C: Superconductivity*, vol. **482** (0), p. 6-18, (2012).
52. C. M. Falco, W. H. Parker, S.E. Trullinger and P. K. Hansma, "Effect of thermal noise on current-voltage characteristics of Josephson junctions", *Physical Review B*, vol. **10** (5), p. 1865-1873, (1974).
53. R. F. Voss, "Noise characteristics of an ideal shunted Josephson junction", *Journal of Low Temperature Physics*, vol. **42** (1-2), p. 151-163, (1981).
54. V. Ambegaokar and A. Baratoff, "Tunneling Between Superconductors", *Physical Review Letters*, vol. **10** (11), p. 486-489, (1963).
55. V. Ambegaokar and A. Baratoff, "Errata - Tunneling Between Superconductors", *Physical Review Letters*, vol. **11** (2), p. 104-104, (1963).
56. M. Podt, *Wideband Low-Noise integrated SQUID systems*, PhD thesis UniversityTwente, 2003.
57. V. Patel and J. E. Lukens, "Self-shunted Nb/AlOx/Nb Josephson junctions", *IEEE Transactions on Applied Superconductivity*, vol. **9** (2), p. 3247-3250, (1999).
58. A. M. Kadin, C. A. Mancini, M. J. Feldman and D. K. Brock, "Can RSFQ logic circuits be scaled to deep submicron junctions?", *IEEE Transactions on Applied Superconductivity*, vol. **11** (1), p. 1050-1055, (2001).
59. R. Jaklevic, J. Lambe, A. Silver and J. Mercereau, "Quantum Interference Effects in Josephson Tunneling", *Physical Review Letters*, vol. **12** (7), p. 159-160, (1964).
60. G. Testa, S. Pagano, E. Sarnelli, C. R. Calidonna and M. M. Furnari, "Improved superconducting quantum interference devices by resistance asymmetry", *Applied Physics Letters*, vol. **79** (18), p. 2943-2945, (2001).
61. G. Testa, E. Sarnelli, S. Pagano, C. R. Calidonna and M. M. Furnari, "Characteristics of asymmetric superconducting quantum interference devices", *Journal of Applied Physics*, vol. **89** (9), p. 5145-5050, (2001).
62. M. Rudolph, J. Nagel, J. M. Meckbach, M. Kemmler, M. Siegel, K. Ilin, D. Koelle and R. Kleiner, "Direct current superconducting quantum interferometers with asymmetric shunt resistors", *Applied Physics Letters*, vol. **101** (5), p. 052602, (2012).
63. C. D. Tesche and J. Clarke, "dc SQUID: Noise and optimization", *Journal of Low Temperature Physics*, vol. **29** (3-4), p. 301-331, (1977).
64. J. Clarke, *SQUID fundamentals*, in *SQUID Sensors: Fundamentals, Fabrication and Applications*, Editor H. Weinstock. Kluwer Academic Publishers: Dordrecht/ Boston/ London. p. 1-62, 1996.
65. J. J. P. Bruines, V. J. Waal and J. E. Mooij, "Comment on: "Dc SQUID: Noise and optimization" by Tesche and Clarke", *Journal of Low Temperature Physics*, vol. **46** (3-4), p. 383-386, (1982).
66. R. H Koch, J. Clarke, W. M. Goubau, J. M. Martinis, C. M. Pegrum and D. J. Harlingen, "Flicker (1/f) noise in tunnel junction dc SQUIDS", *Journal of Low Temperature Physics*, vol. **51** (1-2), p. 207-224, (1983).
67. S. Machlup, "Noise in semiconductors - spectrum of a Two-parameter random signal", *Journal of Applied Physics*, vol. **25** (3), p. 341-343, (1954).
68. P. Dutta, P. Dimon and P. M. Horn, "Energy Scales for Noise Processes in Metals", *Physical Review Letters*, vol. **43** (9), p. 646-649, (1979).
69. P. Dutta and P. M. Horn, "Low-frequency fluctuations in solids: 1/f noise", *Reviews of Modern Physics*, vol. **53** (3), p. 497-516, (1981).

70. D. J. Van Harlingen, T. L. Robertson, B. L. T. Plourde, P. A. Reichardt, T. A. Crane and J. Clarke, "Decoherence in Josephson-junction qubits due to critical-current fluctuations", *Physical Review B*, vol. **70** (6), p. 064517, (2004).
71. D. Drung, *Advanced SQUID read-out electronics*, in *SQUID Sensors: Fundamentals, Fabrication and Applications*, Editor H. Weinstock. Kluwer Academic Publishers: Dordrecht/ Boston/ London. p. 63-116, 1996.
72. M. A. Washington and T. A. Fulton, "Observation of flux trapping threshold in narrow superconducting thin films", *Applied Physics Letters*, vol. **40** (9), p. 848-850, (1982).
73. E. Dantsker, S. Tanaka, P.-A. Nilsson, R. Kleiner and John Clarke, "Reduction of 1/f noise in high-Tc dc superconducting quantum interference devices cooled in an ambient magnetic field", *Applied Physics Letters*, vol. **69** (26), p. 4099-4101, (1996).
74. G. Stan, S. Field and J. M. Martinis, "Critical Field for Complete Vortex Expulsion from Narrow Superconducting Strips", *Physical Review Letters*, vol. **92** (9), p. 097003, (2004).
75. K. Kuit, J. Kirtley, W. van der Veur, C. Molenaar, F. Roesthuis, A. Troeman, J. Clem, H. Hilgenkamp, H. Rogalla and J. Flokstra, "Vortex trapping and expulsion in thin-film $YBa_2Cu_3O_{7-\delta}$ strips", *Physical Review B*, vol. **77** (13), p. 134504, (2008).
76. R. H Koch, D. DiVincenzo and J. Clarke, "Model for 1/f Flux Noise in SQUIDs and Qubits", *Physical Review Letters*, vol. **98** (26), p. 267003, (2007).
77. F. Yoshihara, K. Harrabi, A. O. Niskanen, Y. Nakamura and J. S. Tsai, "Decoherence of flux qubits due to 1/f flux noise", *Physical Review Letters*, vol. **97** (16), p. 167001, (2006).
78. N. Oukhanski, R. Stolz and H. G. Meyer, "High slew rate, ultrastable direct-coupled readout for dc superconducting quantum interference devices", *Applied Physics Letters*, vol. **89** (6), p. 063502, (2006).
79. R. Stolz, *Supraleitende Quanten-interferenzdetektor-Gradiometer-Systeme für den geophysikalischen Einsatz*, PhD thesis University Jena, 2006.
80. M. M. T. M. Dierichs, R. A. Panhuyzen, C. E. Honingh, M. J. de Boer and T. M. Klapwijk, "Submicron niobium junctions for submillimeter-wave mixers using optical lithography", *Applied Physics Letters*, vol. **62** (7), p. 774-776, (1993).
81. M. Watanabe, Y. Nakamura and J.-S. Tsai, "Circuit with small-capacitance high-quality Nb Josephson junctions", *Applied Physics Letters*, vol. **84** (3), p. 410-412, (2004).
82. K. K. Likharev and V. K. Semenov, "RSFQ logic/memory family: a new Josephson-junction technology for sub-terahertz-clock-frequency digital systems", *IEEE Transactions on Applied Superconductivity*, vol. **1** (1), p. 3-28, (1991).
83. J. E. Mooij, T. P. Orlando, L. Levitov, Lin Tian, C. H. van der Wal and S. Lloyd, "Josephson Persistent-Current Qubit", *Science*, vol. **285** (5430), p. 1036-1039, (1999).
84. M. Gurvitch, M. A. Washington and H. A. Huggins, "High quality refractory Josephson tunnel junctions utilizing thin aluminum layers", *Applied Physics Letters*, vol. **42** (5), p. 472-474, (1983).
85. H. Kroger, L. N. Smith and D. W. Jillie, "Selective niobium anodization process for fabricating Josephson tunnel junctions", *Applied Physics Letters*, vol. **39** (3), p. 280-282, (1981).

86. T. Imamura and S. Hasuo, "A submicrometer Nb/AlOx/Nb Josephson junction", *Journal of Applied Physics*, vol. **64** (3), p. 1586-1588, (1988).
87. R. Dolata, T. Weimann, H. J. Scherer and J. Niemeyer, "Sub µm Nb/AlOx/Nb Josephson junctions fabricated by anodization techniques", *IEEE Transactions on Applied Superconductivity*, vol. **9** (2), p. 3255-3258, (1999).
88. M. B. Ketchen, D. Pearson, A. W. Kleinsasser, C. K. Hu, M. Smyth, J. Logan, K. Stawiasz, E. Baran, M. Jaso, T. Ross, K. Petrillo, M. Manny, S. Basavaiah, S. Brodsky, S. B. Kaplan, W. J. Gallagher, and M. Bhushan, "Sub-µm, planarized, Nb-AlOx-Nb Josephson process for 125 mm wafers developed in partnership with Si technology", *Applied Physics Letters*, vol. **59** (20), p. 2609-2611, (1991).
89. Z. Bao, M. Bhushan, R. Siyuan and J. E. Lukens, "Fabrication of high quality, deep-submicron Nb/AlOx/Nb Josephson junctions using chemical mechanical polishing", *IEEE Transactions on Applied Superconductivity*, vol. **5** (2), p. 2731-2734, (1995).
90. A. H. Worsham, D. E. Prober, J. H. Kang, J. X. Przybysz and M. J. Rooks, "High-quality sub-micron Nb trilayer tunnel junctions for a 100 GHz SIS receiver", *IEEE Transactions on Magnetics*, vol. **27** (2), p. 3165-3167, (1991).
91. M. B. Ketchen, "Design considerations for DC SQUIDs fabricated in deep sub-micron technology", *Magnetics, IEEE Transactions on*, vol. **27** (2), p. 2916-2919, (1991).
92. D. Yohannes, S. Sarwana, S. K. Tolpygo, A. Sahu, Y. A. Polyakov and V. K. Semenov, "Characterization of HYPRES' 4.5 kA/cm^2 & 8 kA/cm^2 Nb/AlOx/Nb fabrication processes", *IEEE Transactions on Applied Superconductivity*, vol. **15** (2), p. 90-93, (2005).
93. M. Kroug, A. Endo, T. Tamura, T. Noguchi, T. Kojima, Y. Uzawa, M. Takeda, Z. Wang and W. Shan, "SIS Mixer Fabrication for ALMA Band10", *IEEE Transactions on Applied Superconductivity*, vol. **19** (3), p. 171-173, (2009).
94. Ch Kaiser, J. M. Meckbach, K. S. Ilin, J. Lisenfeld, R. Schäfer, A. V. Ustinov and M. Siegel, "Aluminum hard mask technique for the fabrication of high quality submicron Nb/Al–AlOx/Nb Josephson junctions", *Superconductor Science and Technology*, vol. **24** (3), p. 035005, (2011).
95. Ch. Kaiser, *High quality Nb/Al-AlOx/Nb Josephson junctions : technological development and macroscopic quantum experiments* PhD thesis Karlsruhe Institute of Technology, 2011.
96. J. M. Meckbach, M. Merker, S. J. Buehler, K. Ilin, B. Neumeier, U. Kienzle, E. Goldobin, R. Kleiner, D. Koelle and M. Siegel, "Sub-µm Josephson Junctions for Superconducting Quantum Devices", *IEEE Transactions on Applied Superconductivity*, vol. **23** (3), p. 1100504, (2013).
97. H. Scherer, T. Weimann, P. Hinze, B. W. Samwer, A. B. Zorin and J. Niemeyer, "Characterization of all-chromium tunnel junctions and single-electron tunneling devices fabricated by direct-writing multilayer technique", *Journal of Applied Physics*, vol. **86** (12), p. 6956-6964, (1999).
98. D. Born, T. Wagner, W. Krech, U. Hubner and L. Fritzsch, "Fabrication of ultrasmall tunnel junctions by electron beam direct-writing", *IEEE Transactions on Applied Superconductivity*, vol. **11** (1), p. 373-376, (2001).
99. Hiroyuki Akaike, Akira Fujimaki, Yoshiaki Takai and Hisao Hayakawa, "Submicrometer-Scale Patterning of Superconducting Nb Films Using Focused Ion Beam", *Japanese Journal of Applied Physics*, vol. **31** (Part 2, No. 4A), p. L410, (1992).

100. H. Akaike, T. Watanabe, N. Nagai, A. Fujimaki and H. Hayakawa, "Fabrication of submicron Nb/AlOx-Al/Nb tunnel junctions using focused ion beam implanted Nb patterning (FINP) technique", *IEEE Transactions on Applied Superconductivity*, vol. **5** (2), p. 2310-2313, (1995).
101. Y. Harada, D. B. Haviland, P. Delsing, C. D. Chen and T. Claeson, "Fabrication and measurement of a Nb based superconducting single electron transistor", *Applied Physics Letters*, vol. **65** (5), p. 636-638, (1994).
102. J. M. Martinis and R. H. Ono, "Fabrication of ultrasmall Nb-AlOx-Nb Josephson tunnel junctions", *Applied Physics Letters*, vol. **57** (6), p. 629-631, (1990).
103. M. Podt, B. G. A. Rolink, J. Flokstra and H. Rogalla, "Low-Tc ramp-type Josephson junctions for SQUIDS", *J. Phys. IV*, vol. **12** (2002), p. 133-136, (2002).
104. S. N. Vdovichev, A. Yu Klimov, Yu N. Nozdrin and V. V. Rogov, "Edge-type Josephson junctions with silicon nitride spacer", *Technical Physics Letters*, vol. **30** (5), p. 374-376, (2004).
105. S. Anders, M. Schmelz, L. Fritzsch, R. Stolz, V. Zakosarenko, T. Schönau and H. G. Meyer, "Sub-micrometer-sized, cross-type Nb–AlOx–Nb tunnel junctions with low parasitic capacitance", *Superconductor Science and Technology*, vol. **22** (6), p. 064012, (2009).
106. H. Dang and M. Radparvar, "A process for fabricating submicron all-refractory Josephson tunnel junction circuits", *IEEE Transactions on Magnetics*, vol. **27** (2), p. 3157-3160, (1991).
107. M. Voss, A. Karpov and K. H. Gundlach, "Submicron Nb-Al-oxide-Nb junctions for frequency mixers", *Superconductor Science and Technology*, vol. **6** (5), p. 373-377, (1993).
108. D. Maier, H. Rothermel, K. H. Gundlach and R. Zimmermann, "Submicron Nb-Al/Al oxide-Nb tunnel junctions sandwiched between Al films", *Physica C: Superconductivity*, vol. **268** (1–2), p. 26-40, (1996).
109. National Instruments Germany GmbH. 2013; http://germany.ni.com/.
110. National Instruments. *NI LabVIEW*. 2013; http://www.ni.com/labview/.
111. T. Krause, *Labview-Software for data acquisition*, 2011.
112. E. P. Houwman, D. Veldhuis, J. Flokstra and H. Rogalla, "Fabrication and properties of Nb/Al, Alox/Nb Josephson tunnel junctions with a double-oxide barrier", *Journal of Applied Physics*, vol. **67** (4), p. 1992-1994, (1990).
113. H. Terai, S. Miki, T. Yamashita, K. Makise and Z. Wang, "Demonstration of single-flux-quantum readout operation for superconducting single-photon detectors", *Applied Physics Letters*, vol. **97** (11), p. 112510, (2010).
114. T. Ortlepp, M. Hofherr, L. Fritzsch, S. Engert, K. Ilin, D. Rall, H. Toepfer, H. G. Meyer and M. Siegel, "Demonstration of digital readout circuit for superconducting nanowire single photon detector", *Optics Express*, vol. **19** (19), p. 18593-18601, (2011).
115. Oxford Instruments, *Customer-specified superconducting magnet system (NbTi) of Oxford Instruments GmbH with a maximum field of 5 T*, 2013.
116. A. Barone and G. Paterno, *Physics and applications of the Josephson effect*. Wiley-VCH, 1982.
117. M. Schmelz, R. Stolz, V. Zakosarenko, S. Anders, L. Fritzsch, M. Schubert and H. G. Meyer, "SQUIDs based on submicrometer-sized Josephson tunnel junctions fabricated in a cross-type technology", *Superconductor Science and Technology*, vol. **24** (1), p. 015005, (2011).

118. M. Schmelz, R. Stolz, V. Zakosarenko, T. Schönau, S. Anders, L. Fritzsch, M. Mück, M. Meyer and H. G. Meyer, "Sub-fT/Hz$^{1/2}$ resolution and field-stable SQUID magnetometer based on low parasitic capacitance sub-micrometer cross-type Josephson tunnel junctions", *Physica C: Superconductivity*, vol. **482**, p. 27-32, (2012).
119. M. D. Fiske, "Temperature and Magnetic Field Dependences of the Josephson Tunneling Current", *Reviews of Modern Physics*, vol. **36** (1), p. 221-222, (1964).
120. D. D. Coon and M. D. Fiske, "Josephson ac and Step Structure in the Supercurrent Tunneling Characteristic", *Physical Review*, vol. **138** (3A), p. A744-A746, (1965).
121. G. Wende, *personal communications*, 2011.
122. Hypres Inc. *Hypres DesignRules - Rev. 23*. 2006; http://www.hypres.com/foundry/.
123. M. Maezawa, M. Aoyagi, H. Nakagawa, I. Kurosawa and S. Takada, "Specific capacitance of Nb/AlO$_x$/Nb Josephson junctions with critical current densities in the range of 0.1 - 18 kA/cm^2", *Applied Physics Letters*, vol. **66** (16), p. 2134-2136, (1995).
124. Alan W. Kleinsasser, M. W. Johnson and K. A. Delin, "Direct measurement of the Josephson plasma resonance frequency from I-V Characteristics", *IEEE Transactions on Applied Superconductivity*, vol. **15** (2), p. 86-89, (2005).
125. D. Yohannes, A. Kirichenko, S. Sarwana and S. K. Tolpygo, "Parametric Testing of HYPRES Superconducting Integrated Circuit Fabrication Processes", *IEEE Transactions on Applied Superconductivity*, vol. **17** (2), p. 181-186, (2007).
126. V. Zakosarenko, L. Warzemann, J. Schambach, K. Blüthner, K. H. Berthel, G. Kirsch, P. Weber and R. Stolz, "Integrated LTS gradiometer SQUID systems for unshielded measurements in a disturbed environment", *Superconductor Science and Technology*, vol. **9**, p. A112-A115, (1996).
127. D. J. Adelerhof, H. Nijstad, J. Flokstra and H. Rogalla, "(Double) relaxation oscillation SQUIDs with high flux-to-voltage transfer: Simulations and experiments", *Journal of Applied Physics*, vol. **76** (6), p. 3875-3886, (1994).
128. M. Podt, J. Flokstra and H. Rogalla, "Low-noise SQUIDs with large transfer: two-stage SQUIDs based on DROSs", *Physica C: Superconductivity*, vol. **372–376**, p. 225-228, (2002).
129. M. Podt, J. Flokstra and H. Rogalla, "An experimental double relaxation oscillation superconducting quantum interference device with on-chip feedback", *Superconductor Science and Technology*, vol. **17** (4), p. 701-704, (2004).
130. T. Reich, P. Febvre, T. Ortlepp, F. H. Uhlmann, J. Kunert, R. Stolz and H. G. Meyer, "Experimental study of a hybrid single flux quantum digital superconducting quantum interference device magnetometer", *Journal of Applied Physics*, vol. **104** (2), p. 024509, (2008).
131. D. Drung, J. Beyer, M. Peters, J. H. Storm and T. Schurig, "Novel SQUID Current Sensors With High Linearity at High Frequencies", *IEEE Transactions on Applied Superconductivity*, vol. **19** (3), p. 772-777, (2009).
132. J. E. Zimmerman, "Sensitivity enhancement of superconducting quantum interference devices through use of fractional-turn loops", *Journal of Applied Physics*, vol. **42** (11), p. 4483-4487, (1971).
133. F. Dettmann, W. Richter, G. Albrecht and W. Zahn, "A monolithic thin film DC-SQUID", *physica status solidi (a)*, vol. **51**, p. K185-K188, (1979).

134. P. Carelli and V. Foglietti, "Behavior of a multiloop dc superconducting quantum interference device", *Journal of Applied Physics*, vol. **53** (11), p. 7592-7598, (1982).
135. D. Drung, S. Knappe and H. Koch, "Theory for the multiloop dc superconducting quantum interference device magnetometer and experimental verification", *Journal of Applied Physics*, vol. **77** (8), p. 4088-4098, (1995).
136. Supracon AG. 2013; http://www.supracon.com/.
137. V. Foglietti, "Double dc SQUID for flux-locked-loop operation", *Applied Physics Letters*, vol. **59** (4), p. 476-478, (1991).
138. A. Chwala, F. Bauer, V. Schultze, R. Stolz and H. G. Meyer, "Helmholtz coil systems for the characterization of SQUID sensor heads", *Inst. Phys. Conf. Ser.*, vol. **158**, p. 739-742, (1997).
139. D. Drung, C. Assmann, J. Beyer, A. Kirste, M. Peters, F. Ruede and T. Schurig, "Highly Sensitive and Easy-to-Use SQUID Sensors", *IEEE Transactions on Applied Superconductivity*, vol. **17** (2), p. 699-704, (2007).
140. D. Drung, R. Cantor, M. Peters, H. J. Scheer and H. Koch, "Low-noise high-speed dc superconducting quantum interference device magnetometer with simplified feedback electronics", *Applied Physics Letters*, vol. **57** (4), p. 406-408, (1990).
141. M. Schmelz, R. Stolz, V. Zakosarenko, T. Schönau, S. Anders, L. Fritzsch, M. Mück and H. G. Meyer, "Field-stable SQUID magnetometer with sub-fT $Hz^{-1/2}$ resolution based on sub-micrometer cross-type Josephson tunnel junctions", *Superconductor Science and Technology*, vol. **24** (6), p. 065009, (2011).
142. J. Luomahaara, P. T. Vesanen, J. Penttilä, J. O. Nieminen, J. Dabek, J. Simola, M. Kiviranta, L. Grönberg, C. J. Zevenhoven, R. J. Ilmoniemi, and J. Hassel, "All-planar SQUIDs and pickup coils for combined MEG and MRI", *Superconductor Science and Technology*, vol. **24** (7), p. 075020, (2011).
143. A. N. Matlashov, E. Burmistrov, P. E. Magnelind, L. Schultz, A. V. Urbaitis, P. L. Volegov, J. Yoder and M. A. Espy, "SQUID-based systems for co-registration of ultra-low field nuclear magnetic resonance images and magnetoencephalography", *Physica C: Superconductivity*, vol. **482**, p. 19-26, (2012).
144. K. Enpuku, T. Muta, K. Yoshida and F. Irie, "Noise characteristics of a dc SQUID with a resistively shunted inductance", *Journal of Applied Physics*, vol. **58** (5), p. 1916-1923, (1985).
145. S. Ward, "AFMAG—Airborne and ground", *Geophysics*, vol. **24** (4), p. 761-787, (1959).
146. Frank Ruede, *Highly sensitive current sensors based on DC-SQUIDs for operation in electromagnetically disturbed environment*, PhD thesis Technical University Berlin, 2009.
147. D. W. Allan, "Time and Frequency (Time-Domain) Characterization, Estimation, and Prediction of Precision Clocks and Oscillators", *IEEE Transactions on Ultrasonics, Ferroelectrics and Frequency Control*, vol. **34** (6), p. 647-654, (1987).
148. C. D. Nugroho, V. Orlyanchik and D. J. Van Harlingen, "Low frequency resistance and critical current fluctuations in Al-based Josephson junctions", *Applied Physics Letters*, vol. **102** (14), p. 142602, (2013).
149. ez SQUID Mess- und Analysegeräte. 2013; http://www.ez-squid.de/.

150. E. Dantsker, S. Tanaka and J. Clarke, "High-T_C superconducting quantum interference devices with slots or holes: Low 1/f noise in ambient magnetic fields", *Applied Physics Letters*, vol. **70** (15), p. 2037, (1997).
151. F. C. Wellstood, C. Urbina and J. Clarke, "Low-frequency noise in dc superconducting quantum interference devices below 1 K", *Applied Physics Letters*, vol. **50** (12), p. 772-774, (1987).
152. F. C. Wellstood, C. Urbina and J. Clarke, "Role of Geometry on the Color of Flux Noise in dc SQUIDs", *IEEE Transactions on Applied Superconductivity*, vol. **21** (3), p. 856-859, (2011).
153. F. Yoshihara, K. Harrabi, A. Niskanen, Y. Nakamura and J. Tsai, "Decoherence of Flux Qubits due to 1/f Flux Noise", *Physical Review Letters*, vol. **97** (16), p. 167001, (2006).
154. K. Kakuyanagi, T. Meno, S. Saito, H. Nakano, K. Semba, H. Takayanagi, F. Deppe and A. Shnirman, "Dephasing of a Superconducting Flux Qubit", *Physical Review Letters*, vol. **98** (4), p. 047004, (2007).
155. J. M. Martinis, S. Nam, J. Aumentado, K. M. Lang and C. Urbina, "Decoherence of a superconducting qubit due to bias noise", *Physical Review B*, vol. **67** (9), p. 094510, (2003).
156. R. Bialczak, R. McDermott, M. Ansmann, M. Hofheinz, N. Katz, E. Lucero, M. Neeley, A. O'Connell, H. Wang, A. Cleland, and J. M. Martinis, "1/f Flux Noise in Josephson Phase Qubits", *Physical Review Letters*, vol. **99** (18), p. 187006, (2007).
157. R. de Sousa, "Dangling-bond spin relaxation and magnetic 1/f noise from the amorphous-semiconductor/oxide interface: Theory", *Physical Review B*, vol. **76** (24), p. 245306, (2007).
158. L. Faoro and L. Ioffe, "Microscopic Origin of Low-Frequency Flux Noise in Josephson Circuits", *Physical Review Letters*, vol. **100** (22), p. 227005, (2008).
159. S. Choi, D.-H. Lee, S. Louie and J. Clarke, "Localization of Metal-Induced Gap States at the Metal-Insulator Interface: Origin of Flux Noise in SQUIDs and Superconducting Qubits", *Physical Review Letters*, vol. **103** (19), p. 197001, (2009).
160. T. Lanting, A. Berkley, B. Bumble, P. Bunyk, A. Fung, J. Johansson, A. Kaul, A. Kleinsasser, E. Ladizinsky, F. Maibaum, R. Harris, M. Johnson, E. Tolkacheva, and M. Amin, "Geometrical dependence of the low-frequency noise in superconducting flux qubits", *Physical Review B*, vol. **79** (6), p. 060509R, (2009).
161. S. Sendelbach, D. Hover, M. Mück and R. McDermott, "Complex Inductance, Excess Noise, and Surface Magnetism in dc SQUIDs", *Physical Review Letters*, vol. **103** (11), p. 117001, (2009).
162. D. Sank, R. Barends, R. Bialczak, Y. Chen, J. Kelly, M. Lenander, E. Lucero, M. Mariantoni, A. Megrant, M. Neeley, P. J. J. O'Malley, A. Vainsencher, H. Wang, J. Wenner, T. C. White, T. Yamamoto, Y. Yin, A. N. Cleland, and J. M. Martinis, "Flux Noise Probed with Real Time Qubit Tomography in a Josephson Phase Qubit", *Physical Review Letters*, vol. **109** (6), p. 067001, (2012).
163. S. M. Anton, I. A. B. Sognnaes, J. S. Birenbaum, S. R. O'Kelley, C. J. Fourie and J. Clarke, "Mean square flux noise in SQUIDs and qubits: numerical calculations", *Superconductor Science and Technology*, vol. **26** (7), p. 075022, (2013).

164. A. Chwala, J. P. Smit, R. Stolz, V. Zakosarenko, M. Schmelz, L. Fritzsch, F. Bauer, M. Starkloff and H. G. Meyer, "Low temperature SQUID magnetometer systems for geophysical exploration with transient electromagnetics", *Superconductor Science and Technology*, vol. **24** (12), p. 125006, (2011).
165. Cryoton Co. Ltd. *Cryoton Co. Ltd.* 2013; http://cryoton.ru/eng/dewar.htm.
166. T. R. Clem, G. J. Kekelis, J. D. Lathrop, D. J. Overway and W. M. Wynn, *Superconducting Magnetic Gradiometers for Mobile Applications with an Emphasis on Ordnance Detection*, in *SQUID Sensors: Fundamentals, Fabrication and Applications*, Editor H. Weinstock. Springer Netherlands. p. 517-568, 1996.
167. D. Drung and M. Mück, *SQUID electronics*, in *The SQUID Handbook vol. 1: Fundamentals and Technology of SQUIDs and SQUID systems*, Editors, J. Clarke and Alex I. Braginski. Wiley-VCH: Weinheim. p. 127-170, 2004.
168. J. Clarke and A.I. Braginski, *The SQUID Handbook: Applications of SQUIDs and SQUID Systems*. Wiley-VCH, 2006.
169. H. F. Morrison, U. Conti, V. F. Labson, E. Nichols and N. E. Goldstein, *Field tests of Noise in SQUID and Induction Coil Magnetometers*, in *Report LBID-901*. April 1984, Earth Science Division, LBL.
170. A. Chwala, J. Kingman, R. Stolz, M. Schmelz, V. Zakosarenko, S. Linzen, F. Bauer, M. Starkloff, M. Meyer and H. G. Meyer, "Noise characterization of highly sensitive SQUID magnetometer systems in unshielded environments", *Superconductor Science and Technology*, vol. **26** (3), p. 035017, (2013).
171. EMIT - electromagnetic imaging technology. *SMARTem24 Geophysical Receiver Systems*. 2013; http://www.electromag.com.au/smartem24.php.
172. Zonge International. *Zonge International*. 2013; http://www.zonge.com/index.html.
173. Anglo American. 2013; http://www.angloamerican.com/.
174. STAR Cryoelectronics. 2013; http://www.starcryo.com/.
175. Magnicon GmbH. 2013; http://www.magnicon.com/.
176. B. Muhlfelder, W. Johnson and M. W. Cromar, "Double transformer coupling to a very low noise SQUID", *IEEE Transactions on Magnetics*, vol. **19** (3), p. 303-307, (1983).
177. F. Gay, F. Piquemal and G. Geneves, "Ultralow noise current amplifier based on a cryogenic current comparator", *Review of Scientific Instruments*, vol. **71** (12), p. 4592-4595, (2000).
178. C. Granata, A. Vettoliere and M. Russo, "An ultralow noise current amplifier based on superconducting quantum interference device for high sensitivity applications", *Review of Scientific Instruments*, vol. **82** (1), p. 013901, (2011).
179. J. Luomahaara, M. Kiviranta and J. Hassel, "A large winding-ratio planar transformer with an optimized geometry for SQUID ammeter", *Superconductor Science and Technology*, vol. **25** (3), p. 035006, (2012).
180. R. Stolz, L. Fritzsch and H. G. Meyer, "LTS SQUID sensor with a new configuration", *Superconductor Science and Technology*, vol. **12** (11), p. 806-808, (1999).
181. K. Hasselbach, C. Veauvy and D. Mailly, "MicroSQUID magnetometry and magnetic imaging", *Physica C: Superconductivity*, vol. **332** (1–4), p. 140-147, (2000).

182. S. K. H. Lam and D. L. Tilbrook, "Development of a niobium nanosuperconducting quantum interference device for the detection of small spin populations", *Applied Physics Letters*, vol. **82** (7), p. 1078, (2003).
183. G. C. Tettamanzi, C. I. Pakes, A. Potenza, C. H. Marrows, S. Prawer and D. N. Jamieson, "Superconducting Microbridge Junctions Fabricated using Focused Ion Beams", *ICONN '06. International Conference on Nanoscience and Nanotechnology, 2006.*, p. 355-358, (2006).
184. A. G. P. Troeman, H. Derking, B. Borger, J. Pleikies, D. Veldhuis and H. Hilgenkamp, "NanoSQUIDs Based on Niobium Constrictions", *Nano Letters*, vol. **7** (7), p. 2152-2156, (2007).
185. L. Hao, J. C. Macfarlane, J. C. Gallop, D. Cox, J. Beyer, D. Drung and T. Schurig, "Measurement and noise performance of nano-superconducting-quantum-interference devices fabricated by focused ion beam", *Applied Physics Letters*, vol. **92** (19), p. 192507, (2008).
186. J. Nagel, O. F. Kieler, T. Weimann, R. Wo□lbing, J. Kohlmann, A. B. Zorin, R. Kleiner, D. Koelle and M. Kemmler, "Superconducting quantum interference devices with submicron Nb/HfTi/Nb junctions for investigation of small magnetic particles", *Applied Physics Letters*, vol. **99** (3), p. 032506, (2011).
187. R. P. Welty and J. M. Martinis, "Two-stage integrated SQUID amplifier with series array output", *IEEE Transactions on Applied Superconductivity*, vol. **3** (1), p. 2605-2608, (1993).
188. K. D. Irwin and M. E. Huber, "SQUID operational amplifier", *Applied Superconductivity, IEEE Transactions on*, vol. **11** (1), p. 1265-1270, (2001).
189. V. K. Kornev, I. I. Soloviev, N. V. Klenov and O. A. Mukhanov, "Bi-SQUID: a novel linearization method for dc SQUID voltage response", *Superconductor Science and Technology*, vol. **22** (11), p. 114011, (2009).
190. V. Kornev, I. Soloviev, N. Klenov, A. Sharafiev and O. Mukhanov, "Array designs for active electrically small superconductive antennas", *Physica C: Superconductivity*, vol. **479** (0), p. 119-122, (2012).
191. P. Longhini, S. Berggren, A. L. de Escobar, A. Palacios, S. Rice, B. Taylor, V. In, O. Mukhanov, G. Prokopenko, M. Nisenoff, E. Wong, and M. C. De Andrade, "Voltage response of non-uniform arrays of bi-superconductive quantum interference devices", *Journal of Applied Physics*, vol. **111** (9), p. 093920, (2012).
192. I. I. Soloviev, V. K. Kornev, A. V. Sharafiev, N. V. Klenov and O. A. Mukhanov, "Bi-SQUID arrays and parallel SQIF structures for active electrically small antennas", *Journal of Surface Investigation. X-ray, Synchrotron and Neutron Techniques*, vol. **6** (4), p. 591-597, (2012).
193. R. E. Miller, W. H. Mallison, A. W. Kleinsasser, K. A. Delin and E. M. Macedo, "Niobium trilayer Josephson tunnel junctions with ultrahigh critical current densities", *Applied Physics Letters*, vol. **63** (10), p. 1423-1425, (1993).